An Unusual Case of Rapid Cyclogenesis in the Northeast Pacific Basin.

By
Patrick T. BEATY

A dissertation submitted in partial fulfillment of
the requirements for the degree of

Doctor of Philosophy
(Atmospheric and Oceanic Sciences)

at the
UNIVERSITY OF WISCONSIN-MADISON
2025

Date of Final Oral Examination: 14 July 2025

The dissertation is approved by the following members of the Final Oral Committee:
Jonathan Martin, Professor, Atmospheric and Oceanic Sciences
Stephanie Henderson, Assistant Professor, Atmospheric and Oceanic Sciences
Andrea Lopez Lang, Associate Professor, Atmospheric and Oceanic Sciences
Elizabeth Maroon, Assistant Professor, Atmospheric and Oceanic Sciences
Brett Hoover, Affiliate Staff, Atmospheric and Oceanic Sciences
Andrew Winters, Assistant Professor, University of Colorado-Boulder

Abstract

An Unusual Case of Rapid Cyclogenesis in the Northeast Pacific Basin.

By Patrick T. BEATY

In late November 2019, a record-setting extratropical cyclone rapidly intensified in the northeast Pacific basin over a relatively cold sea surface and near steep topography along the United States West Coast. Cyclogenesis began as a lower-tropospheric diabatic Rossby wave (DRW) spawned from intense, differential lower-tropospheric frontogenesis at the intersection of a zonally-oriented baroclinic zone and warm, moist tropical air plume, with the cyclone then propagating eastward through a pre-existing expansive anticyclone. Then, an intensifying upper-level jet/front system (UJFS) borne from a downward surge of stratospheric air plunged equatorward from Alaska and became favorably aligned with the DRW to result in deepening rates as high as 6 hPa hr^{-1} before the cyclone made landfall near the California-Oregon border. The November 2019 (NV19) storm is of particular interest as the cyclone followed an unusual storm track for explosively-deepening cyclones, intensified at an extremely rapid rate based on two climatologies, and underwent its maximum deepening in a location that was the furthest east based on three climatologies.

This dissertation provides a comprehensive analysis of this explosive cyclogenesis event, which includes a detailed synoptic overview and is motivated by three central research questions which explore distinct aspects of this unusual storm. Using piecewise potential vorticity (PV) inversion, the evolution of the storm is shown to follow a rare bottom-up development whereby most of the intensification period was driven by the DRW with additional intensification provided by the UJFS just prior to landfall. Further application of the piecewise PV inversion results reveals that the UJFS strengthened primarily due to upper-tropospheric PV with minimal influence from PV associated with the DRW, suggesting independent intensification of the UJFS and the DRW. Ensemble-based sensitivity analysis highlighted that ensemble members which forecasted a stronger NV19 storm also forecasted a later interaction between the UJFS and the DRW, which further supports the idea that these two structures primarily intensified independently. Future analysis of explosive cyclogenesis events involving a DRW and UJFS is needed, including further investigation into the NV19 storm, comparing the NV19 storm to similar explosive cyclogenesis events, and simulating the behavior of DRWs within a warming climate.

Acknowledgements

It takes a village for a person to complete a PhD and I am indebted to each and every resident of my village who helped me achieve my dream. Before I personally thank those in my life, I want to acknowledge that this research has been supported by the National Science Foundation under Grant AGS-1851152.

I would like to acknowledge my advisor, Jonathan Martin, for shaping me into a diligent, thorough, and inquisitive scientist. You are always equally excited about the smallest detail and largest result and that excitement transformed the way I approach scientific discovery. You allowed me the freedom to explore any avenue I found interesting while also providing focused feedback to guide my thinking. Through your mentorship, I have become an independent and confident researcher with the ability to constructively criticize my own work. I owe a portion of my master's degree, my PhD degree, and my presentation ability to you for taking a chance on the "Wizard of Omaha". I also will never forget that I am undefeated in tennis against *the* Jonathan Martin.

I would like to thank my PhD committee members: Stephanie Henderson, Brett Hoover, Andrea Lopez Lang, Elizabeth Maroon, and Andrew Winters. Your detailed guidance and constructive skepticism greatly improved the breadth and quality of this research. You all also served as outstanding examples of productive scientists whom I will continue to strive to be. Finally, I was lucky enough to have most of you as instructors, and I aim to model my teaching after all of you setting great examples. I would like to individually thank Michael Morgan for being a witty collaborator and exceptional mentor. I hope our friendship never 'gpend's. I would also like to individually thank Angela Rowe, whose perseverance as an educator and researcher was admirable, and whose donut runs/mentor sessions were always appreciated. Finally, I would be remiss to not individually thank Pete Pokrandt, the glue which holds AOS and all of our sanities together. You helped with countless coding and technology issues over the years and were the best driver during Weather Watch. You also became a friendly face whom I looked forward to seeing on the 14th floor.

Next, I would like to thank all of my collaborators. Chris Davis is acknowledged for developing the piecewise PV inversion code used in the analysis. My ability to comprehend and manipulate the piecewise PV inversion code is thanks to Andrew Winters, who offered support, suggestions, and encouragement over many emails and video calls while I learned the piecewise PV inversion code. You were also a thoughtful co-author who has an innate ability to steer your questions and comments towards enlightening avenues of further investigation. Gary Lackmann played a crucial role in the development and refinement of the research from intricacies within the synoptic overview to overarching conclusions suggested by the piecewise PV inversion results. It has been an honor collaborating with one of the great minds within the synoptic meteorology community and I look forward to future collaboration opportunities.

Next, I would like to thank the Martonian Lab: Libby Orr, Poush Ghosh, and Flora Walchenbach. You are all incredibly important people in my life whom I will cherish forever. Libby, you have been by my side throughout this journey, offering your support in every way that I needed. I am so grateful that we found each other at the AOS poster session where it all began. Here's to many more poster sessions, The WLDLFE concerts, sand and indoor volleyball games, scary movies, sushi restaurants, craft days, and weddings in the near and distant future. Poush, you are one of my closest friends ever. We have both grown so much over our grad school careers and we have kept it as tight as Tia-Clair's hamstrings. I owe you for several very important aspects of my life, including knowing what to order at coffee shops, how to properly lift, how to use PowerPoint in an internationally-diverse classroom, when its Wednesday, and for your behind the scenes efforts at Union South and in Fort Wayne, Indiana in 2024. Flora, you are one of the coolest people I have ever met. I have appreciated getting to know you from your fashion to your quips, and your silly lunches in between. Thank you for being a kindhearted, tea-loving person to 'puter across from.

Next, I would like to thank the AOS staff: Christi Balas Levenson, Carolyn Lipke, Dee Van Ruyven, Scott Dyke, and Sabrina Manero. We are truly blessed to have such caring and supportive people helping us navigate the complexity that accompanies getting an advanced degree. I have many friends to thank within the AOS department: Becca Hall, Karissa Shannon, Jack Zweifel, Tanner Blanke, Grant Gilcrease, Kyle Obremski, Carolyn Bean, Ruby Burgess, Ian Cornejo, Ian Beckley, Jongjin Seo, Andi Muttaqin, Nuo Chen, Rudra Thaker, Sagar Rathod, Stefanie Kluge, and Adrianna Modelska. You all have impacted my PhD journey immensely and I am grateful for the memories we share. I also would like to thank several former students of mine: Nate Falkinham, Jared Van Bramer, Anastasia Tomanek, Jacob Servais, and Vince Nayman. I have learned just as much from you as you have learned from me.

Finally, I would like to especially thank my family. My success both during my PhD and in every other aspect of my life is all a credit to the loving environment I get to experience every single day. To my mother, Mary, who continues to offer unwavering support and encouragement throughout every aspect of my life. You are the reason I am able to persevere through any challenge set before me and always remember to 'have a sparkly day'. To my father, John, who sparks my scientific curiosity and advocates for me to be the best version of myself. You are the reason I am able to achieve everything I set within my sights and always remember to 'be a good kid'. To my sister, Liz, who is my biggest fan and my best friend. You are the reason I have always reached for the stars and have known how special I am my whole life, even though you tried to give me back when I was 1 month old. I also received unwavering support and encouragement from my uncle Steve Cox, my aunt Julie Selner, my uncle Tom Beaty, my cousin Caroline Beaty-Helms, my uncle Paul Beaty, and my grandma Mary Cox. And finally to my dog, Kelvin. You can't read this but I owe you a walk and a treat for being the best little guy ever.

Table of contents

List of Figures

1. Introduction

In late November 2019, an extremely rapid, record-setting extratropical cyclogenesis event occurred over the northeast Pacific Ocean. The development is of particular interest as much of the strengthening occurred in an unusual environment characterized by cold sea surface temperatures and near steep topography along the United States West Coast.

On 25 November 2019, a stationary upstream surface cyclone was situated to the south of the Aleutian Islands and a pre-existing surface baroclinic zone stretched eastward towards the United States West Coast through an expansive surface anticyclone. The stationary upstream surface cyclone ushered warm, moist tropical air poleward towards the surface baroclinic zone, which resulted in a strip of intense, but horizontally restricted, lower-tropospheric frontogenesis. The resultant thermally direct vertical circulation mobilized a diabatically-generated, cyclonic lower-tropospheric vortex known as a diabatic Rossby wave (DRW) which began propagating eastward along the baroclinic zone.

On 26 November 2019, an intensifying upper-level jet/front system (UJFS) originating over Alaska became favorably aligned with the lower-tropospheric DRW as it continued to propagate eastward. The UJFS focused a region of vigorous cyclonic vorticity advection by the thermal wind, indicative of column-mean divergence and ascent (Sutcliffe 1947), over the surface cyclone for more than 12 hours as it approached landfall on the California-Oregon border. The compounding forcings for cyclogenesis from the lower- and upper-troposphere resulted in deepening rates as high as 6 hPa hr^{-1} prior to the November 2019 (hereafter NV19) storm making landfall around 0300 UTC 27 November 2019. The NV19 cyclone set all-time low pressure records along the United States West Coast and record-high significant wave heights off the California coast before becoming a prolific winter storm and disrupting travel across the United States during the following week.

Rapid cyclogenesis events have been of interest since their original classification by Tor Bergeron (Sanders and Gyakum 1980). Detailed studies and summaries of infamous rapid cyclogenesis events are numerous throughout the literature (e.g. Lynott and Cramer 1966; Bosart 1981; Gyakum 1983a,b;

Uccellini et al. 1985; Uccellini 1986; Whitaker et al. 1988; Dickinson et al. 1997; Wernli et al. 2002; Zhang et al. 2002; Revell and Gorman 2003; Hultquist et al. 2006; Rivière et al. 2010; Odell et al. 2013; Chang et al. 2013; Heo et al. 2015, 2019; Suri et al. 2025; Beaty et al. 2025). These rapidly deepening cyclones frequently have devastating impacts on the shipping industry, marine life, agriculture, the ecology industry, and coastal and inland societies. The NV19 storm had its own slew of devastating impacts including widespread heavy snow, blizzard conditions, flash flooding, high winds, severe thunderstorms, and tornadoes. The NV19 storm caused $200 million in damage across the United States (NOAA National Centers for Environmental Information 2019) and was classified as "Significant" using the Regional Snowfall Index, which estimates the disruption snowstorms have on the affected population (Squires et al. 2014). It is therefore crucial to understand the dynamics and evolution of rapid cyclogenesis events to aid in their accurate prediction and to minimize their disruption on life.

The analysis of the unusual rapid cyclogenesis of the NV19 storm consists of a detailed synoptic overview and a comprehensive investigation of the development motivated by three main research questions. The synoptic overview as presented in Chapter 2 covers a 36-hour period at twelve hour increments from 1200 UTC 25 November, prior to the nascent stage of cyclogenesis, to 0000 UTC 27 November, past the period of most rapid development and as the storm made landfall on the West Coast of the United States.

The first main research question was: what was the sequence of processes involved in the development of the NV19 storm? In Chapter 2, the 3D Ertel potential vorticity (PV) structure associated with this storm was partitioned into separate upper-tropospheric, lower-tropospheric, and diabatically-induced anomalies which were separately inverted to recover the balanced flow associated with each piece. The inversion operation and recovery of the balanced flow revealed that development followed a bottom-up sequence by which near-surface PV dominated early cyclogenesis, diabatically-induced PV dominated a large period of subsequent intensification, and upper-tropospheric PV dominated the final period of development. Bottom-up developments of this intensity are rare. It is shown that diabatic influences in response to vigorous latent heat release are responsible for much of the lower-tropospheric cyclogenesis early in the lifecycle with the UJFS becoming the predominant driver for the rapid cyclogenesis at later times, and immediately prior to landfall.

The second main research question was: to what extent did the NV19 lower-tropospheric DRW influence the development of the UJFS? In Chapter 3, the balanced flow recovered from performing piecewise PV inversion was used to calculate the $\vec{Q}$-vector (Hoskins et al. 1978) associated with each piece of the partitioned PV. The $\vec{Q}$-vector was then used to invert the quasi-geostrophic ω equation. Finally, the magnitude of frontogenetic tilting and vertical vorticity generation via tilting associated with each piece of the partitioned PV in the vicinity of the strengthening UJFS was determined using the distribution of ω. The relative strength of positive ω, or subsidence, through the jet core afforded by the upper-tropospheric PV, diabatically-induced PV, and lower-tropospheric PV was compared to uncover which piece of the PV was most responsible for intensifying the UJFS via subduction of the tropopause into the mid-troposphere. It is found that upper-tropospheric PV was primarily responsible for the strengthening of the UJFS, with a negligible amount of UJFS intensification provided by diabatically-induced PV. Therefore, the UJFS, which was an important driver for cyclogenesis prior to landfall, intensified without substantial aid from the lower-tropospheric DRW even when the UJFS and DRW were vertically collocated and forcing rapid surface cyclogenesis.

The third main research question was: given the established sequence of development after exploring the first two research questions, what were some of the controls of the intensity of the NV19 storm? In Chapter 4, ensemble-based forecast sensitivity analysis (ESA) was performed on the NV19 development. ESA establishes a linear relationship between a forecast metric (NV19 storm intensity) and perturbed initial conditions (the controls) per ensemble member using forecast ensemble statistics. Ensemble members from the ECMWF integrated forecast system (IFS; ECMWF 2024) ensemble suite were used in the ESA. The results of the analysis revealed that mean sea-level pressure off the coast of California and Oregon near the time of peak intensity of the NV19 cyclone was sensitive to changes in variables such as 850 hPa 2-D frontogenesis, 925 hPa potential vorticity, 500 hPa relative vorticity, and

500 hPa cyclonic relative vorticity advection by the 300-700 hPa thermal wind. Comparing ensemble members portraying a stronger NV19 cyclone to those portraying a weaker NV19 cyclone suggested that mutual amplification between the lower-tropospheric DRW and the UJFS was crucial to the record-setting nature of this development, with ensemble members portraying a stronger NV19 cyclone forecasting a delayed interaction and independent strengthening between the lower-tropospheric DRW and the UJFS.

The future of investigation into DRW evolutions is vast as speculated in Chapter 5, including further analysis of the NV19 storm. Iterated, optimal perturbation analysis using the adjoint model can be used to determine if the NV19 storm reached its maximum potential strength. Summer 2019 featured the rapid development of the second-strongest marine heatwave in the northeast Pacific basin which lasted well past fall 2019, and the potential connection between that marine heatwave and the NV19 storm could be analyzed in-depth. Additional DRW explosive deepening cases can be explored using the methods developed and refined within this analysis. One viable candidate for this additional analysis is a DRW which rapidly deepened into a 945 hPa cyclone off the Washington, USA, and British Columbia coast in the latter-half of November 2024. This cyclogenesis event appears to exhibit some striking dynamical similarities to the cyclogenesis event in November 2019. Additionally, the Northern and Southern Hemisphere climatologies of DRW evolutions presented in Boettcher and Wernli (2013) and Boettcher and Wernli (2015), respectively, could be expanded to feature a longer catalog of DRW events to track changes in frequency, intensity, and geographic location of DRWs during specific periods of interest. Finally, a tool like a large-scale climate model could be used to simulate and investigate DRW evolutions under a future warming climate, with a comparison of past and simulated future DRWs to highlight potential key developmental differences of these future rapidly-deepening cyclones.

2. Overview and Piecewise PV Inversion

2.1. Introduction

Rapid extratropical cyclogenesis, colloquially known as "bomb" cyclogenesis (e.g., Sanders and Gyakum 1980; Roebber 1984) arises from a variety of different dynamical and thermodynamical factors including the interaction between upper-tropospheric troughs and lower-tropospheric baroclinic zones (e.g., Sanders 1986; Gyakum et al. 1992; Lagouvardos et al. 2007; Heo et al. 2019), diabatic heating in the form of latent heat release, (Bosart 1981; Roebber 1993; Martin and Otkin 2004; Terpstra et al. 2015; Kohl and O'Gorman 2022) and/or sea-surface heat fluxes (e.g., Davis and Emanuel 1988; Roebber 1989; Kuo et al. 1991; Gyakum and Danielson 2000; Kouroutzoglou et al. 2015). In addition, the interaction between a diabatic Rossby wave (DRW) and an upper-tropospheric trough (Wernli et al. 2002; Moore et al. 2008; Rivière et al. 2010; Boettcher and Wernli 2011, 2013; McKenzie 2014; Tamarin and Kaspi 2016; Zhang and Wang 2018) is a particular kind of rapid cyclogenesis event. The concept of a DRW was introduced in a series of studies in the early 1990s (i.e., Raymond and Jiang 1990; Snyder and Lindzen 1991; Parker and Thorpe 1995). The latter two studies employed highly idealized models with cloud-diabatic feedbacks in the vicinity of lower-troposphere baroclinic zones to consider both the production, and subsequent evolution, of positive low-level potential vorticity (PV) anomalies beneath the location of maximum cloud production.

Studies by Moore and Montgomery (2004, 2005) were the first to classify such low-level PV anomalies as diabatically-generated vortices. The interaction between the associated cyclonic flow around such a vortex and the baroclinic zone along which it forms acts to provide continued positive moisture and temperature advections downstream of the vortex. These advections contribute to the production of clouds and precipitation, which regenerate the lower-tropospheric cyclonic PV anomaly downstream,

---

This chapter is an edited version of the peer-reviewed publication:

Beaty, P. T., J. E. Martin, A. C. Winters, and G. M. Lackmann, 2025: An Unusual Case of Rapid Cyclogenesis in the northeast Pacific Basin. Overview and Piecewise PV Inversion. Monthly Weather Review, 154, https://doi.org/10.1175/MWR-D-24-0198.1.

thereby appearing to propagate the original anomaly downstream (Terpstra et al. 2015; Tamarin and Kaspi 2016; Kohl and O'Gorman 2022).

In late December 1999, storm *Lothar* devastated portions of western Europe, becoming the costliest windstorm in European history in terms of structural and ecological damage (Wernli et al. 2002). Focusing their analysis of the event on the evolution of *Lothar* as a DRW, Wernli et al. (2002) showed that *Lothar* underwent a 'bottom-up' development in which the lower-tropospheric cyclonic PV anomaly (the DRW), acting on an initially zonal upper-tropospheric flow, induced upper-tropospheric trough development which eventually enabled a superposition of upper- and lower-tropospheric PV features. Though bottom-up development of explosive DRWs with no pre-existing upper-tropospheric trough is rare (Boettcher and Wernli 2013), such a configuration served to initiate the mutual amplification of the two features which was manifest in the rapid development of *Lothar*. Rivière et al. (2010) employed the Météo-France operational model to perform a sensitivity analysis on the development of *Lothar* and, though analysis was centered around the investigation of *Lothar*, the conclusions were extended to explosive development of DRWs in general. They found that the explosive growth stage of rapidly developing DRWs such as *Lothar* are highly dependent on 1) moist processes to overcome frictional and turbulent dissipation, 2) the location of the upper-level jet exit region to aid in synoptic-scale ascent, and 3) a lower-tropospheric baroclinic zone to encourage DRW self-sustenance.

Boettcher and Wernli (2011) used four European Centre for Medium-Range Weather Forecasts (ECMWF) model forecasts initialized at different lead times along with a DRW-tracking algorithm to interrogate the influence of downstream lower-tropospheric temperature and moisture advections on rapid DRW developments. Boettcher and Wernli (2013) constructed a 10-year climatology of DRWs in the Northern Hemisphere based on the tracking algorithm developed in Boettcher and Wernli (2011). These consecutive studies led to the identification of four precursor environments favorable for DRW genesis: 1) a broad subtropical high advecting warm air and moisture towards a baroclinic zone, 2) a cutoff low or remnant tropical cyclone advecting warm air and moisture towards a baroclinic zone, 3) an upper-tropospheric trough moving over a lower-tropospheric baroclinic zone, and 4) the remnants of a tropical cyclone or mesoscale convective system propagating along a baroclinic zone as a lower-tropospheric vortex. Frequent locations of rapid DRW developments in the Northern Hemisphere were along the Gulf Stream in the Atlantic Ocean and following the climatological North Pacific wintertime jet (Boettcher and Wernli 2013). In addition, they suggested that most cases of explosive DRW development involve a DRW interacting with a pre-existing upper-tropospheric trough.

Moore et al. (2008) and Rivière et al. (2010) both took advantage of the utility of the piecewise PV inversion method introduced by Davis and Emanuel (1991) to attribute the intensification of a DRW cyclogenesis event to discrete pieces of the full column PV. The cases chosen for both studies were DRWs propagating over warm sea surface temperatures (SSTs) which provides substantial surface heat and moisture fluxes to aid in the rapid strengthening of the DRW (e.g., Davis and Emanuel 1988; Roebber 1989; Kuo et al. 1991; Gyakum and Danielson 2000; Kouroutzoglou et al. 2015). To the best of the authors' knowledge, a similar analysis on an explosive DRW development over a cold ocean surface ($<$ 12°C) has not yet been performed. DRW developments over such cold ocean surfaces represented an estimated 5% of *all* tracked DRWs in the Boettcher and Wernli (2013) climatology.

From 0000 UTC 26 November to 0000 UTC 27 November 2019, a DRW, originating at the intersection of a high θ_e tropical moisture plume and a zonally oriented baroclinic zone, underwent rapid cyclogenesis over the northeast Pacific Ocean. DRW intensification followed the description offered by Boettcher and Wernli (2013), wherein low-level diabatically-generated PV associated with the DRW vortex became vertically collocated with an upper-tropospheric PV anomaly borne of a downward and equatorward surge of stratospheric air. Hourly ECMWF reanalysis version 5 (ERA5; Hersbach et al. 2020) data suggest that this superposition of forcings resulted in a remarkable mean sea level pressure (MSLP) fall of 49 hPa in 24 hours as the DRW progressed east-southeastward towards the United States West Coast. As the storm neared landfall, the MSLP dropped 12 hPa between 1600 UTC and 1900 UTC 26 November, including a 1-hour central MSLP fall of 6 hPa from 1700 UTC to 1800 UTC 26 November 2019. The observed MSLP minimum of 973.4 hPa at Crescent City, California at 0300 UTC 27 November 2019 set the all-time low sea-level pressure record for the state of California. November low sea-level pressure records were also observed in Medford, Oregon (981.4 hPa) and Eureka, California (984.4 hPa) on the same date.

The November 2019 (hereafter NV19) cyclone provides an opportunity to interrogate the nature of an explosive DRW development over a cold ocean surface. The analysis will center on a piecewise PV inversion of this particular cyclone following the method of Davis and Emanuel (1991). Comparing this event to those previously examined (over warm SSTs) will highlight physical precursors critical for rapid DRW-induced development in such an otherwise unfavorable environment. The paper is organized as follows. An overview of the reanalysis data and the piecewise PV inversion method utilized in this study is detailed in Section 2.2. Section 2.3 provides a synoptic evolution of the lifecycle of the November 2019 cyclone from 12 hours before genesis to post-occlusion and affirms that this is a DRW-induced development while highlighting its exceptional nature. The evolution of the lifecycle of the storm through the lens of piecewise PV inversion is discussed in Section 2.4. Comparison of this event to the bottom-up development of *Lothar* along with conclusions and suggestions for further analysis are offered in Section 2.5.

2.2. Data and Methods

2.2.1. Dataset

Wind speed and direction, temperature, geopotential height, relative humidity, and MSLP data for the NV19 storm were extracted on a limited area domain extending from 10°N to 75°N and 180° to 90°W from the ERA5 data set (Hersbach et al. 2020) obtained from the Copernicus Climate Data Store. The analysis employs ERA5 data at 1-hour intervals from 0000 UTC 01 November to 2300 UTC 31 December 2019 with a horizontal grid spacing of 0.25° × 0.25° and 19 vertical levels from 1000 hPa to 100 hPa at a vertical grid spacing of 50 hPa. ERA5 data were then regridded to a grid spacing of 1.0° × 1.0° as coarse data with smooth gradients is more amenable to the PV inversion process (Hoskins et al.

1985). ERA5 hourly MSLP and wind data were compared with the 3-hourly Weather Prediction Center and the 6-hourly Ocean Prediction Center Pacific surface observations to confirm their accuracy.

2.2.2. Piecewise PV inversion

First envisioned by Rossby (1940), Ertel (1942) expressed the potential vorticity (often referred to as the Ertel PV (EPV)) as

$$EPV = -g\,(\zeta_\theta + f)\,\frac{\partial\theta}{\partial p} \tag{1}$$

where g is gravitational acceleration, ζ_θ is the isentropic relative vorticity, f is the planetary vorticity, and $\frac{\partial\theta}{\partial p}$ is a static stability term. EPV is conserved for adiabatic, inviscid flow. Information about the atmospheric flow associated with a distribution of EPV can be extracted through the process of PV inversion (Hoskins et al. 1985; Davis and Emanuel 1991). The inversion of a distribution of PV, often done in pressure coordinates to avoid complexities of θ coordinates, requires knowledge of 1) a horizontal and vertical distribution of PV, 2) prescribed boundary conditions on the domain, and 3) a balance condition which relates the mass to the momentum field. It can be particularly enlightening to partition the PV field into discrete pieces each related to different vertical levels and/or physical processes involved in cyclogenesis, a technique known as *piecewise PV inversion* first introduced by Davis and Emanuel (1991, hereafter DE). Such piecewise PV inversion isolates the mass and momentum fields associated with individual pieces of the total anomalous PV, thus enabling investigation of the effect of each piece on the overall circulation tendency and the advection of the other pieces of the PV. The way the PV is partitioned is thus crucially important to both the procurement and the precision of the resulting insights.

The DE inversion method assumes hydrostatic balance and that the magnitude of the rotational part of the flow is much larger than that of the divergent part of the flow. Applying these approximations to the divergence equation and equation (1) results in the system of equations, in spherical coordinates, used in the DE piecewise PV inversion:

$$\nabla^2\Phi = \nabla\cdot(f\nabla\psi) + \frac{2}{a^4\cos^2\phi}\frac{\partial\left(\frac{\partial\psi}{\partial\lambda},\frac{\partial\psi}{\partial\phi}\right)}{\partial(\lambda,\phi)} \tag{2}$$

$$\mathrm{EPV} = \frac{g\kappa\pi}{p}\left[(f+\nabla^2\psi)\frac{\partial^2\Phi}{\partial^2\pi} - \frac{1}{a^2\cos^2\phi}\frac{\partial^2\psi}{\partial\lambda\,\partial\pi}\frac{\partial^2\Phi}{\partial\lambda\,\partial\pi} - \frac{1}{a^2}\frac{\partial^2\psi}{\partial\phi\,\partial\pi}\frac{\partial^2\Phi}{\partial\phi\,\partial\pi}\right], \tag{3}$$

where Φ is the geopotential, ψ is the nondivergent streamfunction, ϕ is the latitude, λ is the longitude, a is the radius of the earth, p is the pressure, $\kappa = R/c_p$, and π is the Exner function $\left[c_p\left(\frac{p}{p_0}\right)^{\kappa}\right]$, which serves as the vertical coordinate (DE). Equation (2), the nonlinear balance condition of Charney (1955), relates the wind and pressure fields according to the assumption that the rotational part of the flow is much larger than the divergent part of the flow, which has been shown to be a good approximation to observed atmospheric flows, especially for flows of the synoptic scale (e.g., Davis et al. 1996). The unbalanced portion of the flow corresponds primarily to the nondivergent component of the ageostrophic wind and cannot be recovered using PV inversion techniques (Davis et al. 1996). The nondivergent flow field recovered from piecewise PV inversion was compared to the pure ERA5 flow field across a $10° \times 10°$ box centered on the NV19 MSLP minimum. Differences between these two flow fields did not exceed 20% for 950 hPa, 10% for 900 hPa, and 5% at and above 850 hPa meaning that piecewise PV inversion is accurately representing this development throughout the troposphere. These larger differences near the surface are directly attributed to stronger nondivergent ageostrophic components of the wind in the vicinity of the intense NV19 cyclone.

Piecewise PV inversion is accomplished by first performing an inversion on the full perturbation PV which is defined by subtracting the 2-month mean PV from the instantaneous PV at 1-hour increments at each grid point during the development of the NV19 storm. For the full perturbation PV inversion, equations (2) and (3) are solved simultaneously for the hourly Φ and ψ, with the lateral boundary conditions for Φ and ψ prescribed by subtracting the 2-month mean Φ and ψ from the instantaneous ERA5 data. The boundary ψ was initialized using Neumann boundary conditions such that the component of the total wind from the ERA5 data which was perpendicular to the boundary was equivalent to the gradient of ψ along that same boundary, and that the net divergence out of the domain was zero. Neumann boundary conditions consistent with hydrostatic balance were prescribed along the bottom (top) of the domain such that the vertically-averaged perturbation potential temperature, defined following the same method used in calculating the perturbation PV, between 1000 hPa and 950 hPa (150 hPa and 100 hPa) were used to define Φ and ψ along the bottom (top) of the domain. Full static PV inversion was performed across the entire horizontal and vertical domain and, to assure a stable solution of equations (2) and (3), negative PV values were manually adjusted to a small positive constant of 0.01 PVU (where $1\ \mathrm{PVU} = 1 \times 10^{-6}\ \mathrm{m^2\ s^{-1}\ K\ kg^{-1}}$) and the static stability was required to remain positive throughout the domain. The threshold for convergence was set to 0.1 meter, the over-relaxation parameters for Φ and ψ were 1.8 and 1.9, respectively, and the under-relaxation parameter was set to 0.3. Each hourly time-step reached convergence after approximately 150 iterations. The reader is referred to DE for a complete description of the boundary conditions and numerical methods used to solve this system.

2.2.3. Partitioning method

The next step in performing piecewise PV inversion is to partition the full perturbation PV field into three distinct pieces. Here we follow a modified version of the piecewise partitioning described in Davis (1992), Korner and Martin (2000), and Winters and Martin (2017) which employs both isobaric and relative humidity criteria. Both the partitioning, and the consequent analysis, were found to be insensitive to a robust, but physically reasonable range of choices considered for the RH threshold (not shown).

The three-way partitioning method used in this study is depicted in Fig. 2.1. The surface PV (SFC) is defined as perturbation PV between 950 hPa and 700 hPa in air with a relative humidity $< 95\%$, and also includes the perturbation potential temperature on the bottom boundary of the domain. SFC is designed to represent the influence of near-surface potential temperature perturbations on the flow throughout the domain, as these are equivalent to PV perturbations along the bottom boundary (Bretherton 1966). The interior PV (INT) is defined as the perturbation PV between 950 hPa and 150 hPa found in air with a relative humidity $\geq 95\%$. INT is designed to represent the influence of diabatic generation and erosion of PV associated with latent heat release, a process central to DRW propagation (Boettcher and Wernli 2013; Terpstra et al. 2015; Tamarin and Kaspi 2016; Kohl and O'Gorman 2022). Therefore, INT can be considered a residual representing both the influence of diabatic processes and other remnant PV anomalies. The upper-tropospheric PV (UPTROP) is defined as the perturbation PV between 650 hPa and 150 hPa found in air with a relative humidity < 95% and includes the perturbation potential temperature on the top boundary of the domain. UPTROP is designed to isolate the role of dry middle- and upper-tropospheric, and stratospheric PV intrusions on the flow, along with stratospheric potential temperature anomalies.

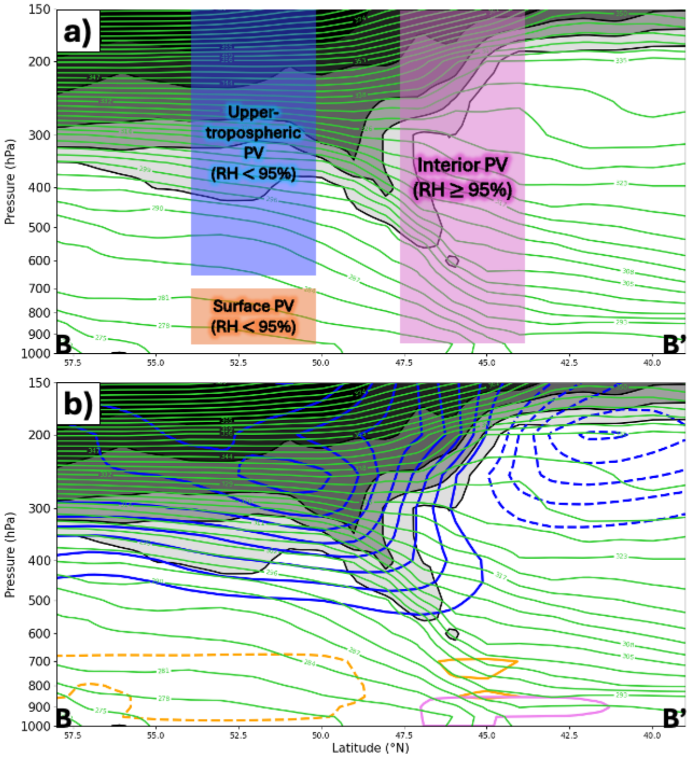

Fig. 2.1. Schematic of the piecewise partitioning scheme used in the inversion of the perturbation PV overlaid on a cross section along B-B' in Fig. 2.4e. Solid, green contours are potential temperature contoured every 3 K starting at 300 K. Potential vorticity is shaded in gray every 2 PVU (1 PVU = 1×10^{-6} m^2 s^{-1} K kg^{-1}) starting at 2 PVU. Labelled boxes correspond to the three distinct pieces of the total perturbation PV with the top and bottom boundaries of each box indicating the isobaric layers included within those pieces. Criterion for relative humidity used to distinguish the pieces of PV are as indicated. (b) As in (a), but with the distribution of upper-tropospheric perturbation PV (blue contours), interior perturbation PV

(pink contours), and surface perturbation PV (orange contours) at 1200 UTC 26 November 2019 contoured every 0.5 PVU. Positive (negative) perturbation PV anomalies denoted by the solid (dashed) contours.

Static inversion is performed for the SFC and UPTROP PV as for the full perturbation PV, but with Φ and ψ on the horizontal boundaries being set to zero. Inversion of the INT PV is not performed; rather, its associated Φ and ψ (Φ_{INT} and ψ_{INT}, respectively) are presented as:

$$\Phi_{INT} = \Phi_{FULL\ PERT} - (\Phi_{SFC} + \Phi_{UPTROP}) \tag{4}$$

and

$$\psi_{INT} = \psi_{FULL\ PERT} - (\psi_{SFC} + \psi_{UPTROP}) \tag{5}$$

where Φ_{INT} and ψ_{INT} on the horizontal boundaries are set equal to the full perturbation Φ and ψ, not zero. The decision to prescribe these results was motivated by numerous unsuccessful trials in which the static inversion of the INT PV, though reaching convergence, consistently returned unphysical results. Similar unphysical results are detailed in both Ahmadi-Givi et al. (2004) and Bracegirdle and Gray (2009). Those studies concluded that such results derive from a breakdown of the Charney nonlinear balance condition (Charney 1955) in regions where strong divergence becomes collocated with regions of strong diabatic heating. The development of the NV19 DRW was strongly influenced by diabatic heating collocated with the lower-tropospheric vortex, hence, the governing physics were well outside the requisite nonlinear balance in equation (2). In such situations, convergence to a solution for the INT PV, characterized by heavy diabatic modification for extended periods of time, will produce a result in which the wind field is not dynamically consistent with the pressure field and the DE system of equations for piecewise PV inversion will no longer be valid. As the present analysis seeks to isolate the influence of the INT PV on aspects of the development, calculating it as a residual affords a tenable means to that end given the circumstances. This residual also predominantly corresponds to moist diabatic processes, as the influences of radiation and turbulence on the PV are much smaller in magnitude on the timescales considered.

2.3. Synoptic Evolution and Anomalous Nature

2.3.1. Overview

We use hourly data from the ERA5 to describe the synoptic overview of the NV19 storm and will focus on twelve hour increments from 1200 UTC 25 November 2019, prior to the nascent stage of development, to 0000 UTC 27 November 2019, past the period of its most rapid development and as the storm made landfall on the West Coast of the United States.

2.3.1.1. 1200 UTC 25 November 2019

Twelve hours before the NV19 storm developed its own closed circulation at sea-level, a predominantly zonally-oriented surface baroclinic zone, indicated by a strong gradient of 950 hPa equivalent potential temperature (θ_e) contours, was draped southeastward from an almost cutoff low pressure system to the west through the center of a strong surface anticyclone to the east (Fig. 2.2a). Though there was no closed isobar evident at this time, there was a 950 hPa relative vorticity maximum (yellow-highlighted "X") at the intersection of this baroclinic zone with a more meridionally oriented cold frontal baroclinic zone (Fig. 2.2a,b). The same baroclinic zones were reflected in the isentropes at 850 hPa, with strong positive frontogenesis occurring due east of the 950 hPa vorticity maximum along the warm front (Fig. 2.2c). Positive 2D frontogenesis, calculated using

$$\Im_{2D} = \frac{1}{|\nabla\theta|}\left[\left(\frac{\partial\theta}{\partial x}\right)\left(-\frac{\partial\vec{V}}{\partial x}\cdot\nabla\theta\right)+\left(\frac{\partial\theta}{\partial y}\right)\left(-\frac{\partial\vec{V}}{\partial y}\cdot\nabla\theta\right)\right] \tag{6}$$

was maximized between 850 and 900 hPa along the baroclinic zone on which the cyclone developed, with negative omega (ascent) focused on the warm side of a deep baroclinic zone in response to that frontogenesis (Fig. 2.2d). At 500 hPa, the surface development region was downstream of the nearly cutoff low pressure center to the southwest and a shortwave feature to the northwest over the Alaska Peninsula (Fig. 2.2e). The surface development region was centered in the right entrance region of a downstream, anticyclonically-curved jet streak at 300 hPa characterized by weak along-flow acceleration in the entrance region (Fig. 2.2f). A 300 hPa PV maximum over the Aleutians was the tropopause-level counterpart to the shortwave at 500 hPa (Fig. 2.2e,f).

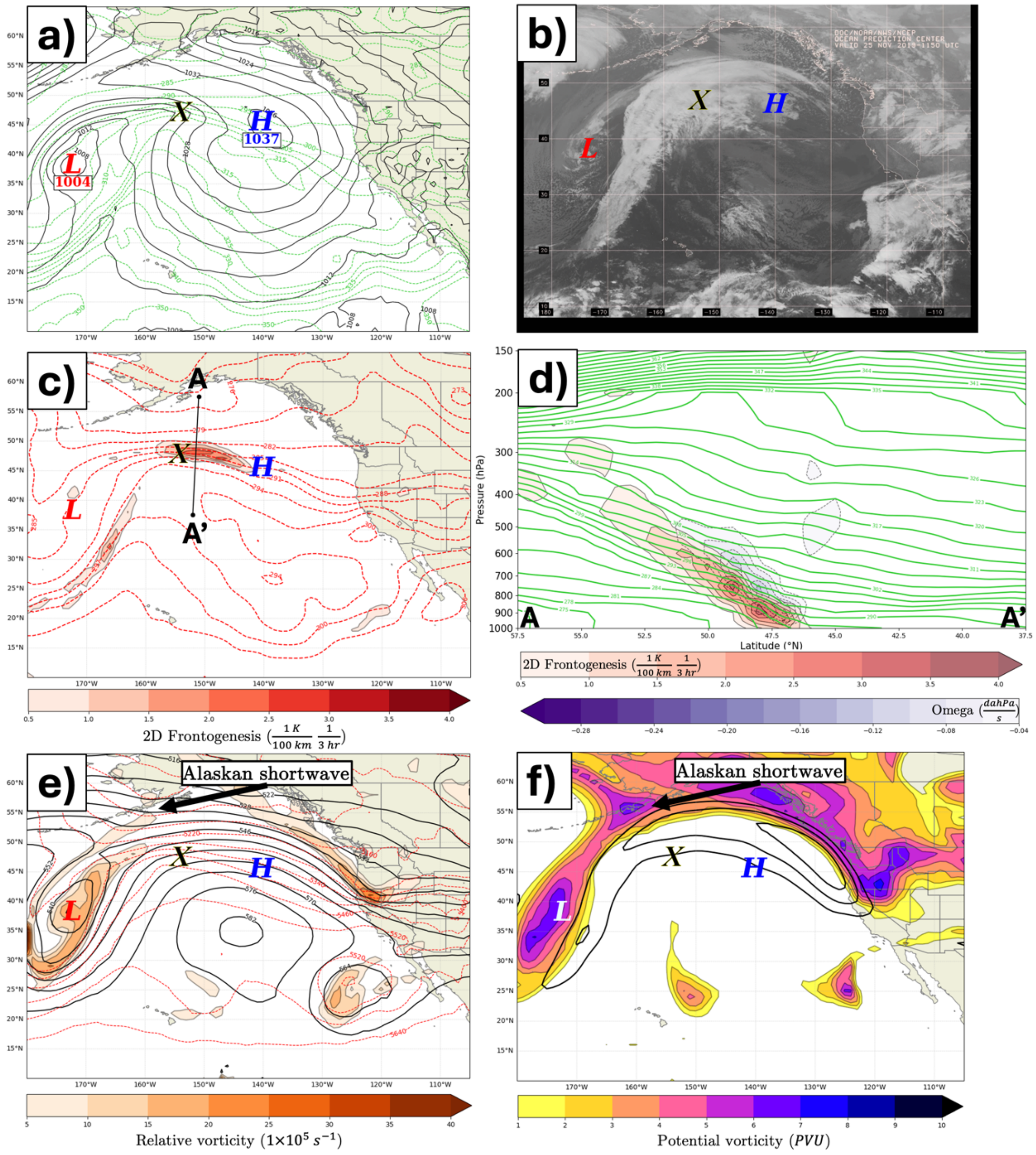

Fig. 2.2. (a) Sea-level pressure and 950 hPa equivalent potential temperature (θ_e) from the ERA5 reanalysis valid at 1200 UTC 25 November 2019. Solid, black lines are isobars contoured every 4 hPa. Dashed, green lines are 950 hPa moist isentropes contoured every 5 K. “H” denotes the centers of high pressure systems whereas “L” denotes centers of low pressure systems. “X” denotes the development region of NV19 storm. (b) GOES-17 infrared imagery of the northeast Pacific basin valid at 1150 UTC 25 November 2019. “H”, “L”, and “X” as in panel (a). (c) Potential temperature and positive horizontal frontogenesis at 850 hPa from the ERA5 reanalysis valid at 1200 UTC 25 November 2019. Dashed, red contours are isentropes contoured every 3 K. Shading indicates positive frontogenesis function values shaded every 0.5 K $(100\text{km})^{-1}$ $(3\text{hr})^{-1}$ starting at 0.5 K $(100\text{km})^{-1}$ $(3\text{hr})^{-1}$. “H”, “L”, and “X” as in panel (a). Black line indicates the cross section shown in panel (d). (d) Cross section along A-A’ in panel (c) of potential temperature, frontogenesis, and negative omega valid at 1200 UTC 25 November 2019. Potential temperature (green) contoured every 3 K starting at 300 K. Positive frontogenesis function (red shading) shaded every 0.5 K $(100\text{km})^{-1}$ $(3\text{hr})^{-1}$. Negative omega (purple dashed shading) shaded every -0.04 daPa s^{-1} starting at -0.04 daPa s^{-1}. (e) 1000 hPa – 500 hPa thickness and relative vorticity at 500 hPa from the ERA5 reanalysis valid at 1200 UTC 25 November 2019. Red dashed contours are lines of constant thickness contoured every 60 meters. Shading indicates positive relative vorticity shaded every 5×10^{-5} s^{-1} starting at 5×10^{-5} s^{-1}. “H”, “L”, and “X” as in panel (a). (f) Potential vorticity and wind speed at 300 hPa from the ERA5 reanalysis valid at 1200 UTC 25 November 2019. Solid, black contours are wind speeds contoured every 10 m s^{-1} starting at 50 m s^{-1}. Shading indicates potential vorticity at 300 hPa shaded every 1 PVU (1 PVU $= 1 \times 10^{-6}$ m^2 s^{-1} K kg^{-1}) starting at 1 PVU. “H”, “L”, and “X” as in panel (a). “L” denoting the low pressure system changed to light blue for visibility.

2.3.1.2. 0000 UTC 26 November 2019

By 0000 UTC 26 November 2019, a weak surface cyclone was discernable along the baroclinic zone that stretched zonally through the anticyclone (Fig. 2.3a). This disturbance had begun to develop its own separate cloud feature by this time (Fig. 2.3b). The 850 hPa baroclinic zone and positive frontogenesis maintained its previous spatial relationship with the developing surface cyclone (Fig. 2.3c), with frontogenesis located to the east and northeast of the surface cyclone along the developing warm front. Positive frontogenesis was now maximized at 800 hPa as the frontal slope notably steepened from the previous time (compare Fig. 2.2d to Fig. 2.3d). In response to this evolution, the ascent associated with the lower-tropospheric frontogenesis was deeper. The shortwave feature at 500 hPa began to strengthen to the northwest of the surface cyclone, indicated by the increase in positive relative vorticity along the shortwave axis (Fig. 2.3e). The proximity of this shortwave resulted in a region of cyclonic vorticity advection (CVA) by the thermal wind, indicative of column mean divergence and ascent (Sutcliffe 1947), coincident with the surface cyclone at this time. At 300 hPa, the surface cyclone maintained its position relative to the right entrance region of the downstream, anticyclonically-curved jet streak with now stronger along-flow speed change characterizing the entrance region (Fig. 2.3f). The shortwave feature at 300 hPa had also strengthened as indicated by the expanding region of large 300 hPa positive PV to the north-northwest of the surface cyclone (Fig. 2.3f).

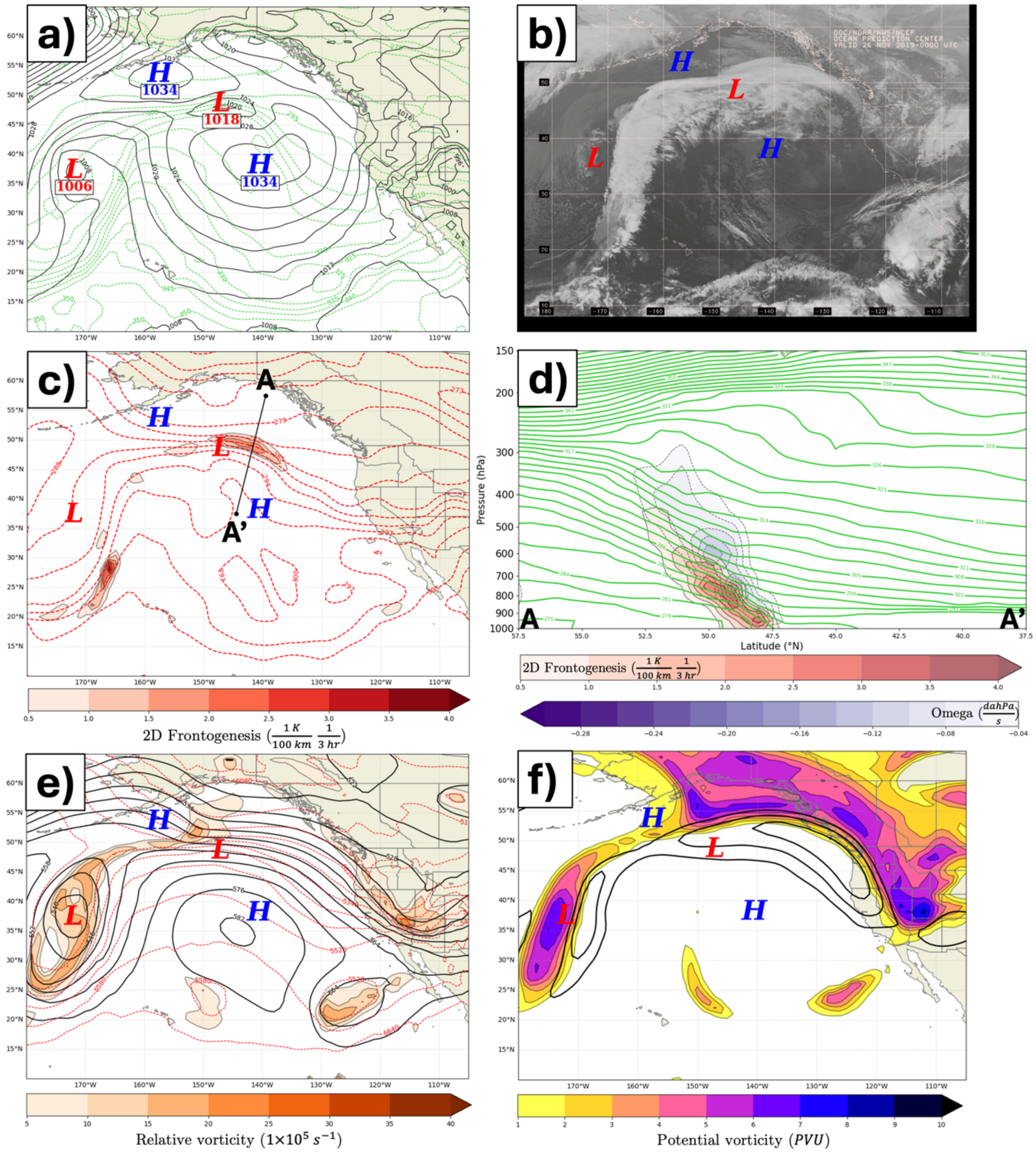
a)
H
1034
L
1018
L
1006
H
1034
b)
DOC/NOAA/NWS/NCEP
OCEAN PREDICTION CENTER
VALID 26 NOV 2019 0000 UTC
H
L
L
H
c)
A
H
L
L
A'
H
2D Frontogenesis $(\frac{1\,K}{100\,km}\frac{1}{3\,hr})$
d)
Pressure (hPa)
Latitude (°N)
A
A'
2D Frontogenesis $(\frac{1\,K}{100\,km}\frac{1}{3\,hr})$
Omega $(\frac{dahPa}{s})$
e)
H
L
L
H
Relative vorticity $(1\times10^{5}\,s^{-1})$
f)
H
L
L
H
Potential vorticity (PVU)

Fig. 2.3. (a) As in Fig. 2.2a except for 0000 UTC 26 November 2019. (b) As in Fig. 2.2b except for 0000 UTC 26 November 2019. (c) As in Fig. 2.2c except for 0000 UTC 26 November 2019. (d) As in Fig. 2.2d except for 0000 UTC 26 November 2019. (e) As in Fig. 2.2e except for 0000 UTC 26 November 2019. (f) As in Fig. 2.2f except for 0000 UTC 26 November 2019.

2.3.1.3. 1200 UTC 26 November 2019

Twelve hours after initial development (Fig. 2.4a), the NV19 storm completely bisected the anticyclone within which it initially developed (see Fig. 2.3a). Well-defined cold and warm fronts now characterized the cyclone, as shown by the 950 hPa θ_e, with pressure troughs associated with both fronts. At this time, the storm was beginning its twelve-hour period of most rapid deepening as it approached the California-Oregon border. The storm was also beginning to transition from a baroclinic leaf (R. B. Weldon 1979) to a more classic comma shape (Fig. 2.4b). The primary band of positive frontogenesis at 850 hPa remained robust and associated with the surface warm front while a band of weaker, positive frontogenesis developed along the cold front (Fig. 2.4c). The cyclone center was now clearly located at the apex of the 850 hPa thermal ridge. Positive frontogenesis peaked at 700 hPa as the warm front neared its maximum strength and the associated ascent expanded and intensified throughout the depth of the mid- to lower-troposphere, now being maximized around 750 hPa (Fig. 2.4d). Rapid intensification and elongation of the 500 hPa positive vorticity feature occurred to the west-northwest of the surface cyclone, coincident with a sharp temperature gradient, indicative of the development of a potent upper-level jet/front system (Fig. 2.4e). This intensification focused vigorous CVA by the thermal wind directly above the surface cyclone and, consequently, the central pressure of the NV19 storm began to rapidly drop. The trough in the 1000-500 hPa thickness also lagged the geopotential height trough resulting in along-flow cold air advection coincident with the 500 hPa relative vorticity maximum (Fig. 2.4e). The thermal gradient directly west of the cyclone had intensified within this same twelve-hour interval. The region of increased baroclinicity was reflected in an increase in wind speed at 300 hPa, at the base of the shortwave feature (Fig. 2.4f). This wind speed intensification also situated the NV19 storm in the left exit region of a newly formed jet streak tied to the development of the upper-level jet/front system (e.g. Shapiro 1981, 1983; Lackmann et al. 1997; Martin 2014), providing another mechanism for enhancing upper-tropospheric mass evacuation and lower-tropospheric cyclogenesis.

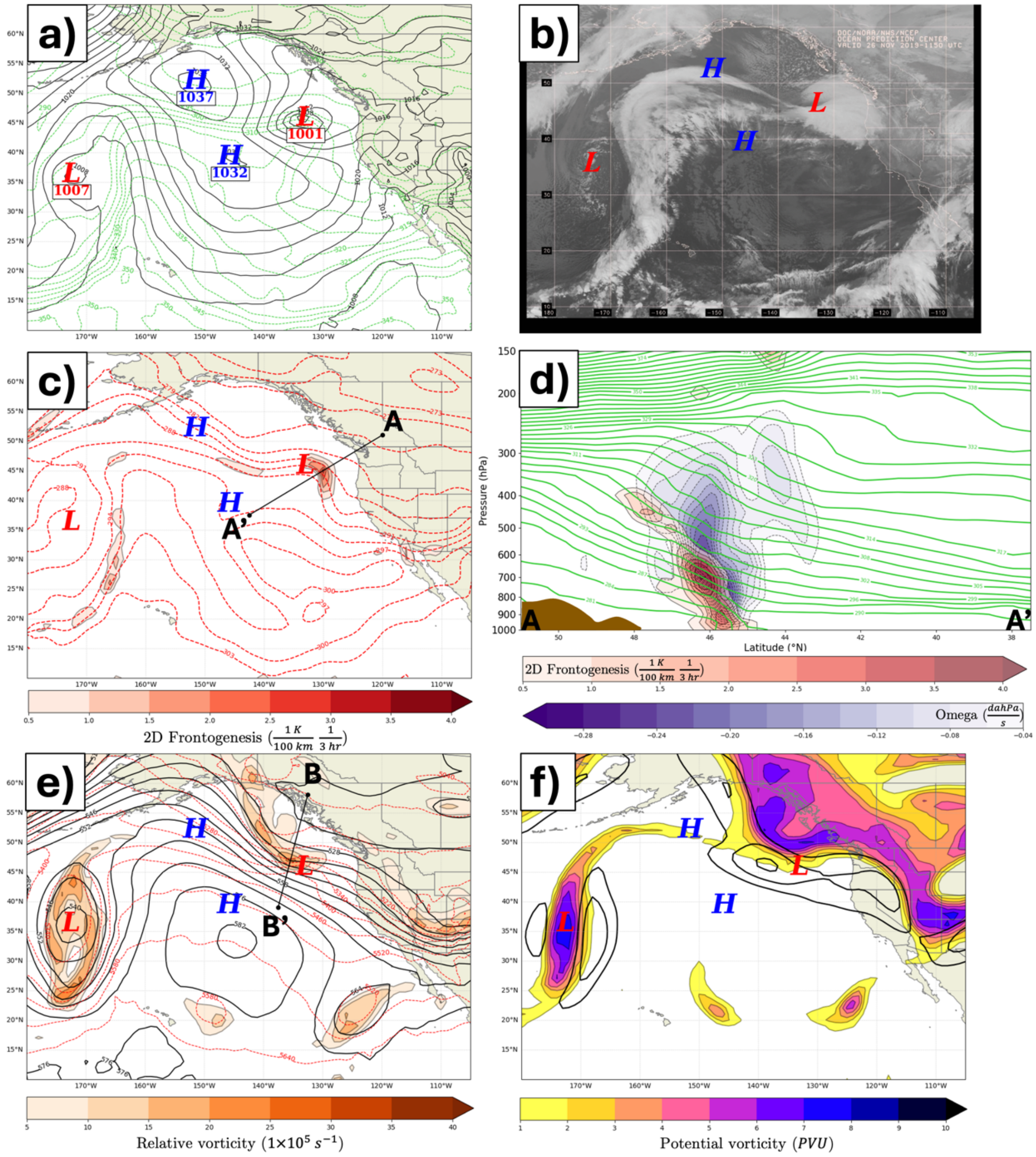

Fig. 2.4. (a) As in Fig. 2.3a except for 1200 UTC 26 November 2019. (b) As in Fig. 2.3b except for 1150 UTC 26 November 2019. (c) As in Fig. 2.3c except for 1200 UTC 26 November 2019. (d) As in Fig. 2.3d except for 1200 UTC 26 November 2019. (e) As in Fig. 2.3e except for 1200 UTC 26 November 2019. (f) As in Fig. 2.3f except for 1200 UTC 26 November 2019.

2.3.1.4. 0000 UTC 27 November 2019

In the twenty-four hours after initial development, the storm had deepened a total of 47 hPa to a central MSLP of 971 hPa, well exceeding the definition of explosive cyclogenesis (at least 24 hPa of deepening in 24 hours) first defined in Sanders and Gyakum (1980) (Fig. 2.5a). In fact, the storm had deepened from 1020 hPa at 2200 UTC 25 November to 971 hPa at 2200 UTC 26 November, resulting in a maximum 24-hour deepening rate of 49 hPa. At 0000 UTC 27 November, the NV19 storm was just a few hours from making landfall on the west coast of the United States near Crescent City, California (Fig. 2.5a,b). The intense pressure gradient to the south of the cyclone center resulted in surface winds greater than 45 m s^{-1} near the California-Oregon border and 24 m waves off the California coast (094 Cape Mendocino buoy). By this time, the positive frontogenesis at 850 hPa associated with the warm front was undoubtedly influenced by the steep topography adjacent to the United States West Coast (Fig. 2.5c,d) as the frontal structure had clearly weakened (Fig. 2.5d). Lower-tropospheric ascent at this time reached its largest values of the cyclone lifecycle, also undoubtedly influenced by the steep topography. A well-developed trough with substantial CVA by the thermal wind and an elongated streamer of vorticity at 500 hPa were both still forcing ascent in and around the surface cyclone (Fig. 2.5e), with the strongest CVA by the thermal wind situated south of the cyclone (not shown). The intensified vortex strip was a manifestation of the continued development of the associated upper-level jet/front system (Fig. 2.5e). The jet streak to the west of the surface cyclone increased in intensity and the surface cyclone remained in the left exit region as the jet raced southeastward on the upstream side of a newly carved out upper trough (Fig. 2.5f). The surface cyclone was now vertically stacked as the 300 hPa PV and 500 hPa vorticity were all maximized at the same location directly above the surface cyclone (Fig. 2.5e,f).

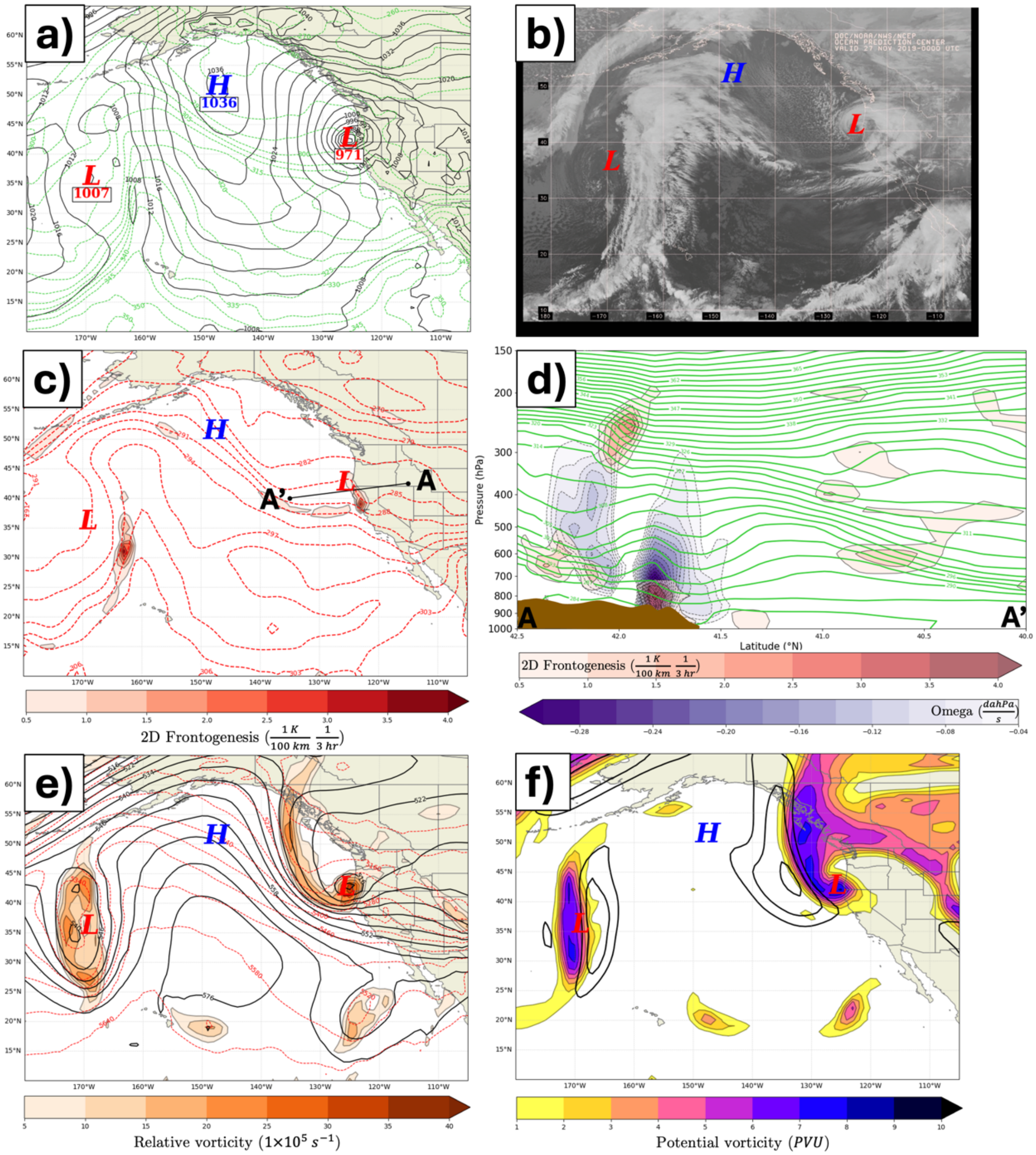
a)
H
1036
L
1007
L
971
b)
DOC/NOAA/NWS/NCEP
OCEAN PREDICTION CENTER
VALID 27 NOV 2019-0000 UTC
H
L
L
c)
H
L
L
A'
A
2D Frontogenesis ($\frac{1\,K}{100\,km}\,\frac{1}{3\,hr}$)
d)
Pressure (hPa)
Latitude (°N)
A
A'
2D Frontogenesis ($\frac{1\,K}{100\,km}\,\frac{1}{3\,hr}$)
Omega ($\frac{dahPa}{s}$)
e)
H
L
L
Relative vorticity ($1{\times}10^5\,s^{-1}$)
f)
H
L
L
Potential vorticity (PVU)

Fig. 2.5. (a) As in Fig. 2.4a except for 0000 UTC 27 November 2019. (b) As in Fig. 2.4b except for 0000 UTC 27 November 2019. (c) As in Fig. 2.4c except for 0000 UTC 27 November 2019. (d) As in Fig. 2.4d except for 0000 UTC 27 November 2019. (e) As in Fig. 2.4e except for 0000 UTC 27 November 2019. (f) As in Fig. 2.4f except for 0000 UTC 27 November 2019.

2.3.2. The NV19 cyclone as a Diabatic Rossby wave

As first introduced by Raymond and Jiang (1990), Snyder and Lindzen (1991), and Parker and Thorpe (1995) and first classified by Moore and Montgomery (2004, 2005), a DRW is a lower-tropospheric vortex borne of positive PV production in the vicinity of a lower-tropospheric baroclinic zone that is situated below mid-tropospheric latent heat release. During the early development phase of the NV19 storm, a nearly cutoff low pressure system south of the Aleutian Islands and an expansive high pressure system off the coast of the Pacific Northwest conspired to produce southerly flow which overan a predominantly zonal baroclinic zone stretching across the northeast Pacific Ocean at 1200 UTC 25 November 2019 (Fig. 2.6a). This flow induced strong lower-tropospheric frontogenesis which, in turn, spawned the production of precipitation along the baroclinic zone as indicated by the 12-hour rainfall rates from the ERA5 data. The ERA5 12-hour rainfall rates agreed with 24-hour rainfall rates from the Integrated Multi-satellitE Retrievals for the Global Precipitation Measurement (GPM) mission (IMERG) in terms of spatial distribution and location of maxima (not shown). A lower-tropospheric circulation developed as a result of the latent heat release that accompanied the production of precipitation. This circulation then propagated along the baroclinic zone for at least the next 12 hours as shown by the location of the SLP minimum along the mean 950 hPa θ_e gradient averaged between 1200 UTC 25 November and 0000 UTC 26 November 2019 (Fig. 2.6b). Thus, there was strong frontogenesis and moist ascent along the baroclinic zone (Fig. 2.2c,d and Fig. 2.3c,d) driving precipitation development and latent heat release which, in turn, mobilized lower-tropospheric diabatic PV "production" (Fig. 2.6a,b). The resulting diabatically-generated vortex provided differential temperature advection near the surface which then propagated the DRW vortex. Propagation speeds averaged 24.4 m s^{-1} throughout the entire DRW lifecycle with a maximum 1-hourly propagation speed of 47.6 m s^{-1} between 1200 UTC and

1300 UTC 26 November. This average far exceeded the threshold of 11.6 m s^{-1} for DRW propagation established in Boettcher and Wernli (2013) and neared the rapid average propagation speeds of ~30 m s^{-1} associated with *Lothar* (Wernli et al. 2002).

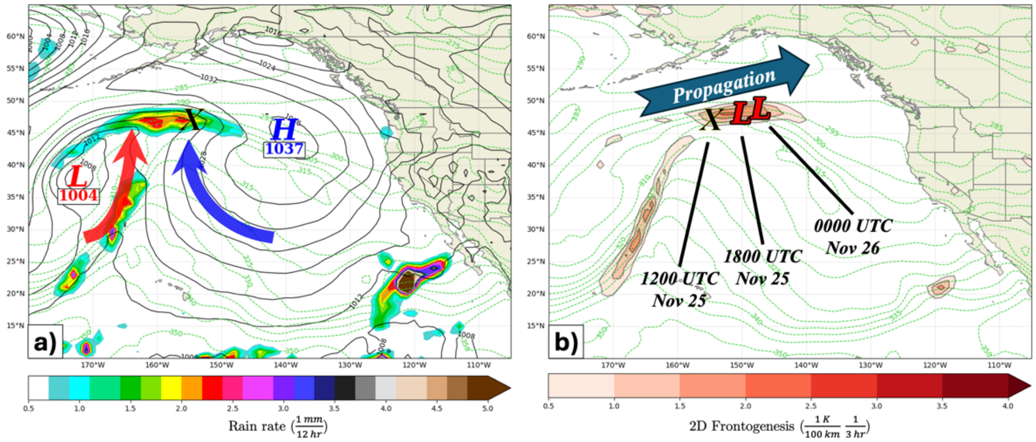

Fig. 2.6. (a) Sea-level pressure and 950 hPa equivalent potential temperature (θ_e) from the ERA5 reanalysis valid at 1200 UTC 25 November 2019. Solid, black lines are isobars contoured every 4 hPa. Dashed, green lines are 950 hPa moist isentropes contoured every 5 K. Shading indicates the rainfall rate valid at 1800 UTC 25 November 2019 shaded every 0.25 mm 12hr^{-1} starting at 0.5 mm 12hr^{-1}. "H" denotes the center of the high pressure system whereas "L" denotes the centers of the low pressure systems. "X" denotes the development region of NV19 storm. Red and blue annotated arrows indicate the lower-tropospheric synoptic-scale flow. (b) Propagation of sea-level pressure minima along the 12-hour mean 950 hPa θ_e between 1200 UTC 25 November and 0000 UTC 26 November 2019, as indicated by arrow. Shading indicates the 12-hour mean 950 hPa positive horizontal frontogenesis between 1200 UTC 25 November and 0000 UTC 26 November 2019 shaded every 0.5 K (100km)$^{-1}$ (3hr)$^{-1}$. Moist isentropes contoured as in (a). "L" and "X" as in panel (a).

Lastly, the diabatic PV generation rate was assessed according to Eq. (74a) in Hoskins et al. (1985):

$$\dot{Q}_{diab} = Q\frac{\partial\dot{\theta}}{\partial p}\left(\frac{\partial\theta}{\partial p}\right)^{-1} - \dot{\theta}\frac{\partial Q}{\partial p}\left(\frac{\partial\theta}{\partial p}\right)^{-1} \tag{7}$$

where Q is the potential vorticity, θ is the potential temperature, and $\dot{\theta}$ is the potential temperature tendency, $\frac{\partial\theta}{\partial t}$. The generalized PV generation rate, which combines the effects of diabatic PV generation (first term on right-hand side of (7)) and diabatic vertical advection of PV (second term on right-hand side of (7)), was averaged over two layers of near equal height following Kohl and O'Gorman (2022) and across a 10° × 10° box centered on the NV19 MSLP minimum throughout its evolution. The average rate of diabatic PV generation in the lower-layer, 950 hPa to 550 hPa, (upper-layer, 500 hPa to 150 hPa,) was zero (negative) as the DRW formed from 1800 UTC 25 November to 0000 UTC 26 November, and then positive (remained negative) as the NV19 DRW strengthened and propagated eastward from 0000 UTC to 0900 UTC 26 November (Fig. 2.7). The positive PV anomaly in the lower-layer, the NV19 DRW, and the negative PV anomaly in the upper-layer were both growing through the diabatic generation of PV as DRW propagation and strengthening began, which agrees with the DRW growth mode presented in Kohl and O'Gorman (2022) and adds additional support to the notion that the NV19 storm originated as a DRW.

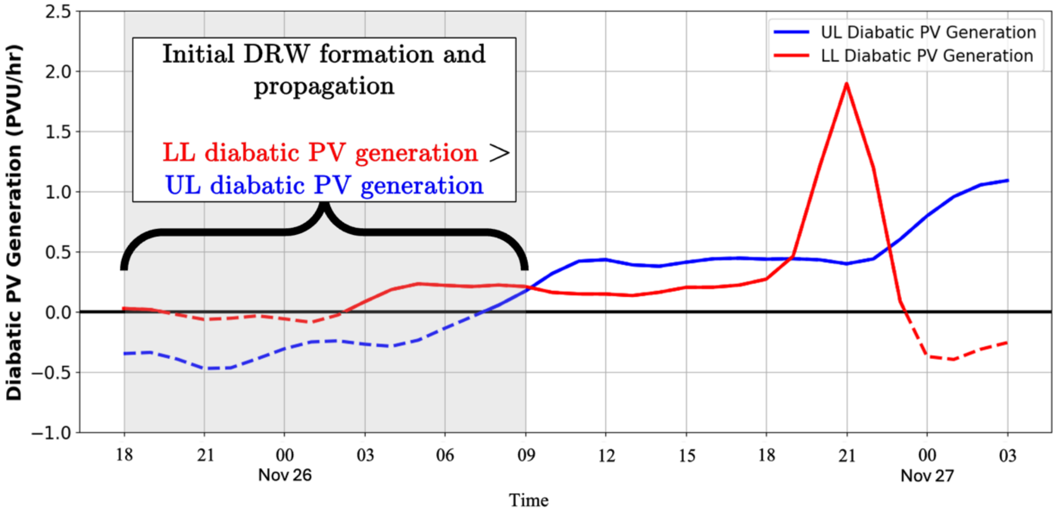

Fig. 2.7. The layer-averaged diabatic PV generation rate in PVU hr^{-1} (1 PVU $= 1 \times 10^{-6}$ m^2 s^{-1} K kg^{-1}) for the upper-layer (500 hPa to 150 hPa, 'UL') and the lower-layer (950 hPa to 550 hPa, 'LL') from 1800 UTC 25 November to 0300 UTC 27 November 2019 averaged across a $10° \times 10°$ box centered on the NV19 storm. Diabatic PV generation rate is contoured in solid blue for the upper-layer and solid red for the lower-layer with negative diabatic PV generation rates for both layers represented as dashed contours.

2.3.3. The anomalous nature of the NV19 storm

Northwesterly flow cyclogenesis events over the northeast Pacific Ocean are common and well-documented (Reed and Albright 1986; Yoshiike and Kawamura 2009; Lang and Martin 2012; Iwao et al.

2012; Iizuka et al. 2013) along with explosive cyclogenesis (EC) events over this part of the Pacific Ocean (Roebber 1984; Wang and Rogers 2001; Boettcher and Wernli 2013; Zhang et al. 2017). Despite the relative frequency of EC events over the northeastern Pacific Ocean, the storm track, deepening rate, and location of maximum deepening for the NV19 storm were all well outside of established climatologies for this part of the world.

First, the NV19 storm had an unusual track. Roebber (1984) constructed a climatology of Northern Hemisphere EC events over the period from 1976 to 1982 while Wang and Rogers (2001) compiled a similar climatology for the period from 1985 to 1996. In still another climatology (from 2000 to 2015), Zhang et al. (2017) specifically focused on EC events over the northern Pacific Ocean. All three studies highlighted preferred regions for periodic EC events: off the east coast of Japan, off the east coast of the United States, and in the central Gulf of Alaska. After genesis, a majority of the cyclones track southwest to northeast based on the roughly 30-year period covered by the three, non-consecutive climatologies. Tamarin and Kaspi (2016) noted that the predominant region of latent heat release associated with DRWs typically occurs to the northeast of the DRW center, which propagates the DRW eastward and poleward. The NV19 cyclone also initially formed in the central Gulf of Alaska and tracked nearly due east before beginning a northwest to southeast track (Fig. 2.2-Fig. 2.5). Zhang et al. (2017) divided their database of EC storm tracks into separate regions of the northern Pacific in which clustering of cyclogenesis events occurred. The storm track of the NV19 cyclone was rotated approximately 90° to the right of both the northeastern Pacific Ocean EC storm tracks from the Zhang et al. (2017) climatology (their Fig. 5e) and the typical direction of DRW propagation from Tamarin and Kaspi (2016). The NV19 track was also mainly outside of the storm track densities presented in Roebber (1984), Wang and Rogers (2001), and Zhang et al. (2017). Thus, the storm track associated with the NV19 storm was unusual based on at least 30 years of non-consecutive climatologies presented in the literature.

Second, the deepening rate of EC events has been quantified using the "Bergeron" since it was originally defined by Sanders and Gyakum (1980) as

$$1\ \text{Bergeron} = \frac{24\ \text{hPa}}{24\ \text{hours}} \cdot \frac{sin(\phi)}{sin(60^\circ)} \tag{8}$$

where ϕ is the latitude of the cyclone center normalized to 60°N. A cyclogenesis event must accomplish a deepening rate equivalent to at least 1 Bergeron to be classified as explosive. Roebber (1984) and Zhang et al. (2017) used normalized latitudes of 42.5° and 45°, respectively, in the denominator of (8) as these mean latitudes were more representative of the mean latitude of explosive cyclogenesis events presented in their studies. The deepening rate of the NV19 storm using the Roebber (1984) and the Zhang et al. (2017) definitions was 2.14 Bergerons and 2.04 Bergerons, respectively. This deepening rate ranks the NV19 storm in the 99th percentile when focusing on the 115 EC cases over the northern Pacific Ocean from the Roebber (1984) climatology and in the 93rd percentile when focusing on the 120 EC cases over the northeast Pacific region from the Zhang et al. (2017) climatology. Further, the maximum 6-hour deepening rate of 22 hPa between 1200 UTC to 1800 UTC 26 November 2019 rivals that of the maximum 6-hour deepening rate of 26 hPa accomplished by the *Braer* storm, the strongest extratropical cyclone on record based both on minimum SLP and deepening rate (Lim and Simmonds 2002; Odell et al. 2013). Therefore, the maximum 6-hour deepening rate of the NV19 storm was among the strongest ever recorded for all extratropical cyclones in the Pacific and Atlantic Ocean basins.

Finally, frequency contours of northern Pacific Ocean EC events are provided using the Roebber (1984), Wang and Rogers (2001), and Zhang et al. (2017) climatologies (Fig. 2.8). The furthest eastward extent of any of these frequency contours is 130°W (Fig. 2.8c). The maximum deepening of the NV19 storm occurred between 1700 UTC and 1800 UTC 26 November 2019 to the east of 130°W longitude. Out of a combined 30-year period of northern Pacific Ocean EC events, no other EC event has had a maximum deepening location as far east as the NV19 storm, yet another aspect of its anomalous nature.

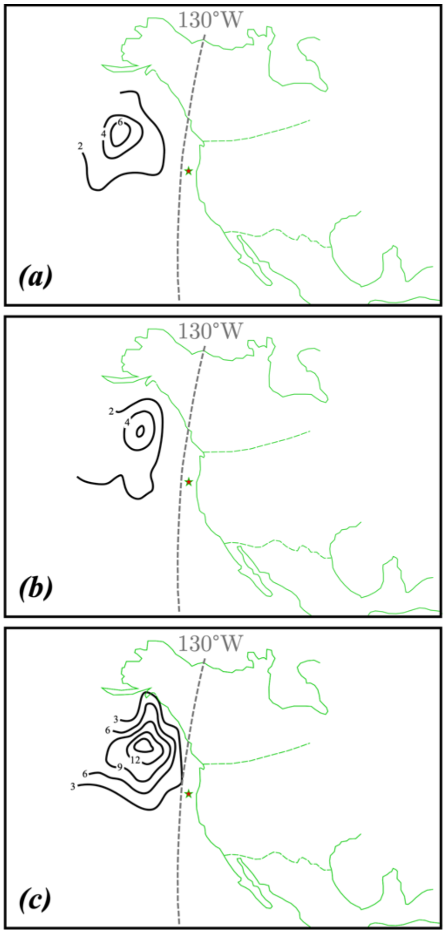

Fig. 2.8. Composite of maximum deepening locations (MDL) for "bomb" cyclogenesis events over the northeastern Pacific Ocean as defined by Sanders and Gyakum (1980) and Zhang et al. (2017). (a) Adapted from Roebber (1984) for MDL between 1976 and 1982. Red star indicates MDL for November 2019 storm. (b) Adapted from Wang and Rogers (2001) for MDL between 1985 and 1996. Red star indicates MDL for November 2019 storm. (c) Adapted from Zhang et al. (2017) for MDL between 2000 and 2015. Red star indicates MDL for November 2019 storm. Dashed, gray line indicates 130°W meridian.

Another unique aspect of this development was that the NV19 storm formed during the second strongest and most persistent marine heatwave (MHW) in the northeast Pacific basin (Chen et al. 2021). This MHW, colloquially known as the 'Blob 2.0', was a result of prolonged weakening of the climatological North Pacific anticyclone which characterizes the northeast Pacific basin during the northern hemisphere summer (Amaya et al. 2020). The weaker North Pacific anticyclone reduced the pressure gradient over the entire region, which decreased the surface winds, the evaporative cooling, and the wind-driven upper ocean mixing. The resultant increased upper ocean SSTs then led to decreased low clouds over the region, which increased solar insolation and further reinforced the increased upper ocean SSTs. The first of four peaks of the Blob 2.0 occurred in November 2019 and was concentrated above 50 m depth (Chen et al. 2021). This shallow peak in the MHW undoubtedly increased lower-tropospheric temperatures through sea surface heat flux, although attenuated as noted above, which reinforced the lower-tropospheric baroclinic zone stretching across the northeast Pacific along which the DRW initially formed (see Fig. 2.2). The influence of the most persistent and near-record strength Blob 2.0 MHW on constructing the environment in which the NV19 storm developed adds yet another extraordinary detail to this unusual cyclogenesis event.

2.4. Analysis

Subsequent analysis will concentrate on the 950 hPa isobaric surface as this level was the lowest available isobaric surface in the inversion output. Fig. 2.9 compares 950 hPa geopotential height (Φ_{950}) at the location of the 950 hPa vorticity maximum of the NV19 storm from the ERA5 analyses and the full PV inversion. Though the full inversion results consistently return a higher Φ_{950}, the hourly positions demonstrate excellent agreement. Results of inverting the 2-month mean PV are not discussed as the analysis is primarily concerned with the perturbation PV introduced into the domain by the NV19 storm.

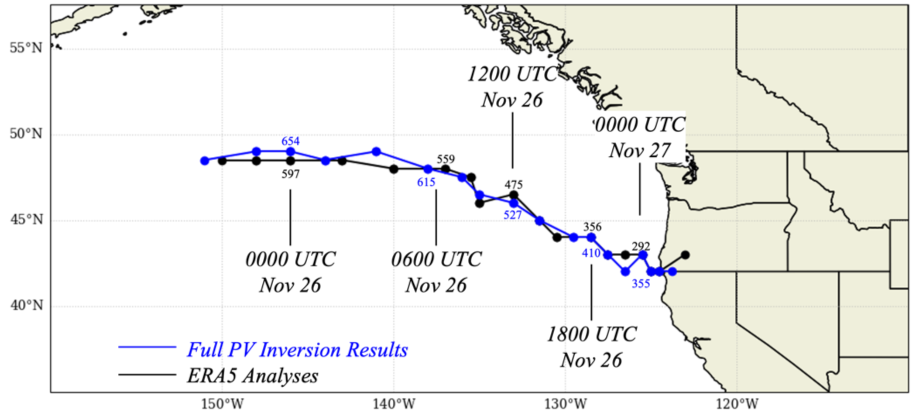

Fig. 2.9. Comparison of the full PV inversion results and the ECMWF reanalysis version 5 (ERA5) analysis of storm track based on location of the 950 hPa vorticity maxima. Location of vorticity maxima in the full PV inversion results are shown in blue with geopotential height at the vorticity maxima plotted in meters. Location of ERA5 analysis vorticity maxima are shown in black with geopotential height at the vorticity maxima plotted in meters.

2.4.1. Piecewise frontogenesis

Piecewise PV inversion allows computation of the horizontal frontogenesis function (6) using the recovered balanced flow from the inversion of the full column perturbation PV and each of the three partitioned pieces of the perturbation PV. The goal is to determine which features in the perturbation PV distribution are controlling the strength and evolution of the initial lower-tropospheric frontogenesis (e.g. Korner and Martin 2000). We hypothesize that the SFC PV controlled the initial genesis as intense lower-tropospheric frontogenesis and associated latent heat release within the thermally-direct circulation spawned the DRW which became the NV19 storm (Fig. 2.2d,Fig. 2.3d, andFig. 2.6). Therefore, we are only partitioning the balanced flow field, not the thermal field, and are considering the kinematic effects of the separate circulations on the total thermal field.

2.4.1.1. 1200 UTC 25 November 2019

Ascent during the initial development of the NV19 storm was situated on the warm side of a frontogenesis maximum at 850 hPa forced by differential θ advection by the FULL PERT balanced flow (Fig. 2.10a). There is good agreement between the distribution and orientation of the frontogenesis calculated using the FULL PERT balanced flow and the frontogenesis calculated using the ERA5 horizontal winds (compare Fig. 2.2d and Fig. 2.10a). A majority of the FULL PERT frontogenesis was forced by the UPTROP PV balanced flow associated with the upstream upper-tropospheric shortwave (Fig. 2.2f and Fig. 2.10b). The balanced flow associated with the INT PV resulted in no notable frontogenesis along the cross section at this time (Fig. 2.10c). A strong, negative INT PV anomaly in the upper-troposphere was located directly above the development region (not shown) due to persistent, differential lower-tropospheric high θ_e flow fueling convection along the baroclinic zone (e.g. Fig. 2.6a). Despite the emergence of a lower-tropospheric positive INT PV anomaly in response to the associated heating, the negative (upper-tropospheric) piece of the INT PV exerted the predominant influence on the total INT PV-induced flow in the development region and, consequently, the INT PV contributed near-zero frontogenesis (Fig. 2.10c). The remaining portion of the lower-tropospheric frontogenesis was forced by the SFC PV balanced flow (Fig. 2.10d). This portion of perturbation frontogenesis was a result of anomalously warm near-surface potential temperatures underneath the 950 and 850 hPa thermal ridge stretching southwest of the development region which facilitated strong differential warm air advection in the lower-troposphere across the baroclinic zone (Fig. 2.2a,c).

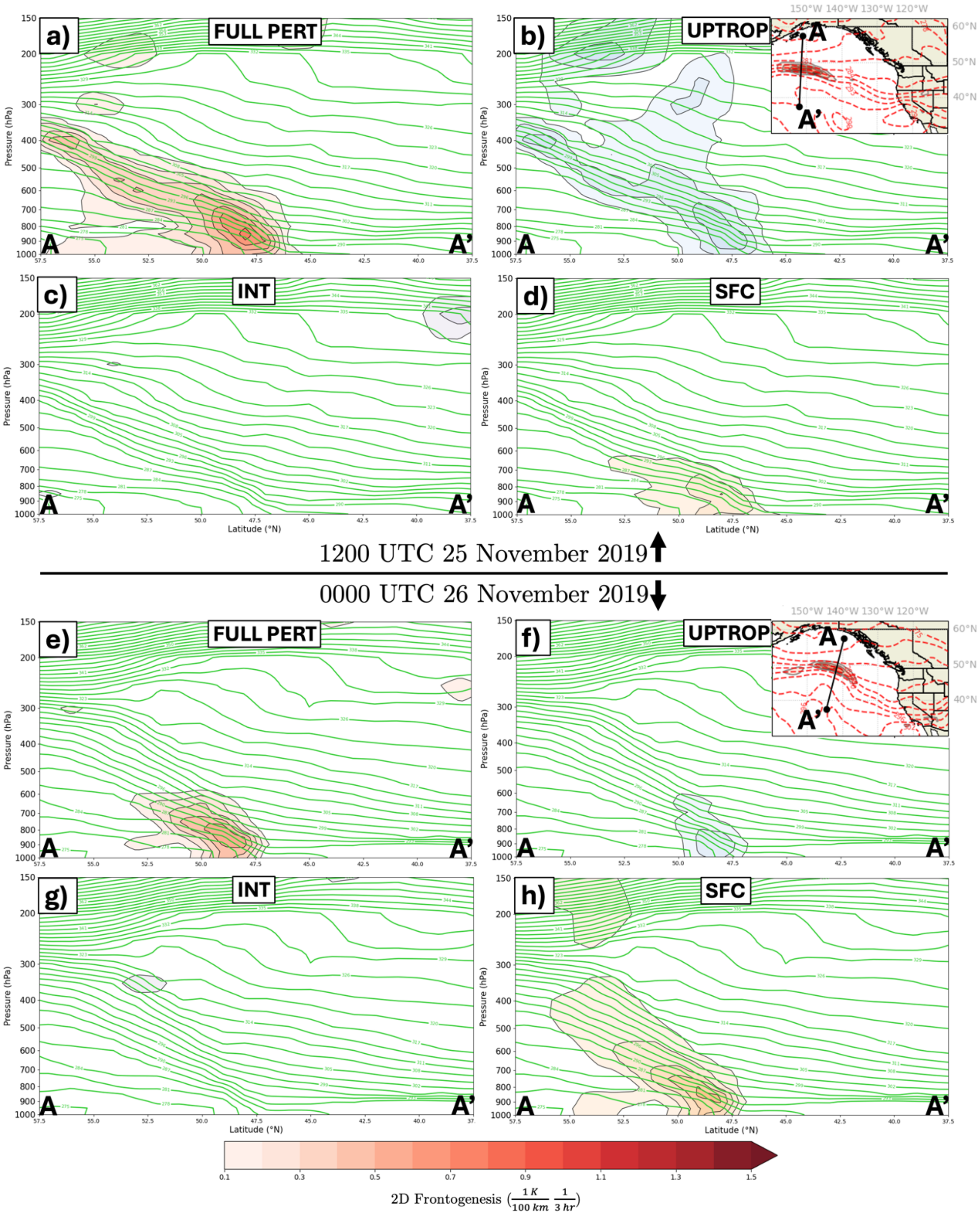

Fig. 2.10. Frontogenesis associated with discrete portions of the balanced flow derived from piecewise PV inversion. (a) Cross section along A-A' in Fig. 2.2c of potential temperature and frontogenesis valid at 1200 UTC 25 November 2019. Potential temperature (green) contoured every 3 K starting at 300 K. Positive frontogenesis function from the full perturbation PV (FULL PERT) balanced flow (red shading) shaded every 1×10^{-1} K (100km)$^{-1}$ (3hr)$^{-1}$ and smoothed using a 9-point smoother. (b) Cross section along A-A' in Fig. 2.2c of potential temperature and frontogenesis valid at 1200 UTC 25 November 2019. Potential temperature (green) contoured every 3 K starting at 300 K. Positive frontogenesis function from the UPTROP PV balanced flow (blue shading) shaded every 1×10^{-1} K

$(100\text{km})^{-1}$ $(3\text{hr})^{-1}$ and smoothed using a 9-point smoother. (c) As in panel (b) but for the positive frontogenesis function from the INT PV balanced flow (pink shading). (d) As in panel (c) but for the positive frontogenesis function from the SFC PV balanced flow (orange shading). (e) As in panel (a) but for a cross section along A-A' in Fig. 2.3c valid at 0000 UTC 26 November 2019. (f) As in panel (b) but for a cross section along A-A' in Fig. 2.3c valid at 0000 UTC 26 November 2019. (g) As in panel (c) but for a cross section along A-A' in Fig. 2.3c valid at 0000 UTC 26 November 2019. (h) As in panel (d) but for a cross section along A-A' in Fig. 2.3c valid at 0000 UTC 26 November 2019.

2.4.1.2. 0000 UTC 26 November 2019

The FULL PERT frontogenesis function became focused in the lower-troposphere as the DRW vortex developed into a weak center of low pressure (Fig. 2.10e). There was still good agreement between the frontogenesis calculated using the FULL PERT balanced flow and the frontogenesis calculated using the ERA5 horizontal winds (compare Fig. 2.3d and Fig. 2.10e). The perturbation frontogenesis forced by the UPTROP PV balanced flow was now both shallower and weaker as compared to twelve hours prior (Fig. 2.10b,f). The DRW was still situated beneath an upper-tropospheric negative INT PV anomaly, and so the balanced flow from the INT PV once again resulted in insubstantial perturbation frontogenesis (Fig. 2.10g). At this time, the majority of the lower-tropospheric frontogenesis appeared forced by the balanced flow attributable to lower-tropospheric potential temperature perturbations (Fig. 2.3a,c and Fig. 2.10h). Perturbation southerly flow introduced via lower-tropospheric potential temperature anomalies provided most of the lower-tropospheric frontogenesis and subsequent latent heat release as NV19 DRW intensification and eastward propagation began.

2.4.2. Hourly height changes

After a coherent lower-tropospheric vortex had formed, the intensification of the NV19 storm was assessed by considering the effects of each of the three pieces of the perturbation PV on near-surface height changes recovered from the piecewise PV inversion process. First, perturbation heights from the ERA5, FULL PERT, UPTROP, and SFC PV inversions, and the INT PV residual, were recorded at the location of the 950 hPa vorticity maximum associated with the NV19 storm. Then the perturbation height change at time t, associated with the ERA5, full perturbation PV, and each of the three pieces, was the result of subtracting the perturbation heights at time $t + 1hr$ from the perturbation heights at time $t -$

$1 hr$ and dividing by the time interval of 2 hrs. The results of these calculations are shown in Fig. 2.11, which displays the various height changes from 2100 UTC 25 November to 0600 UTC 27 November 2019.

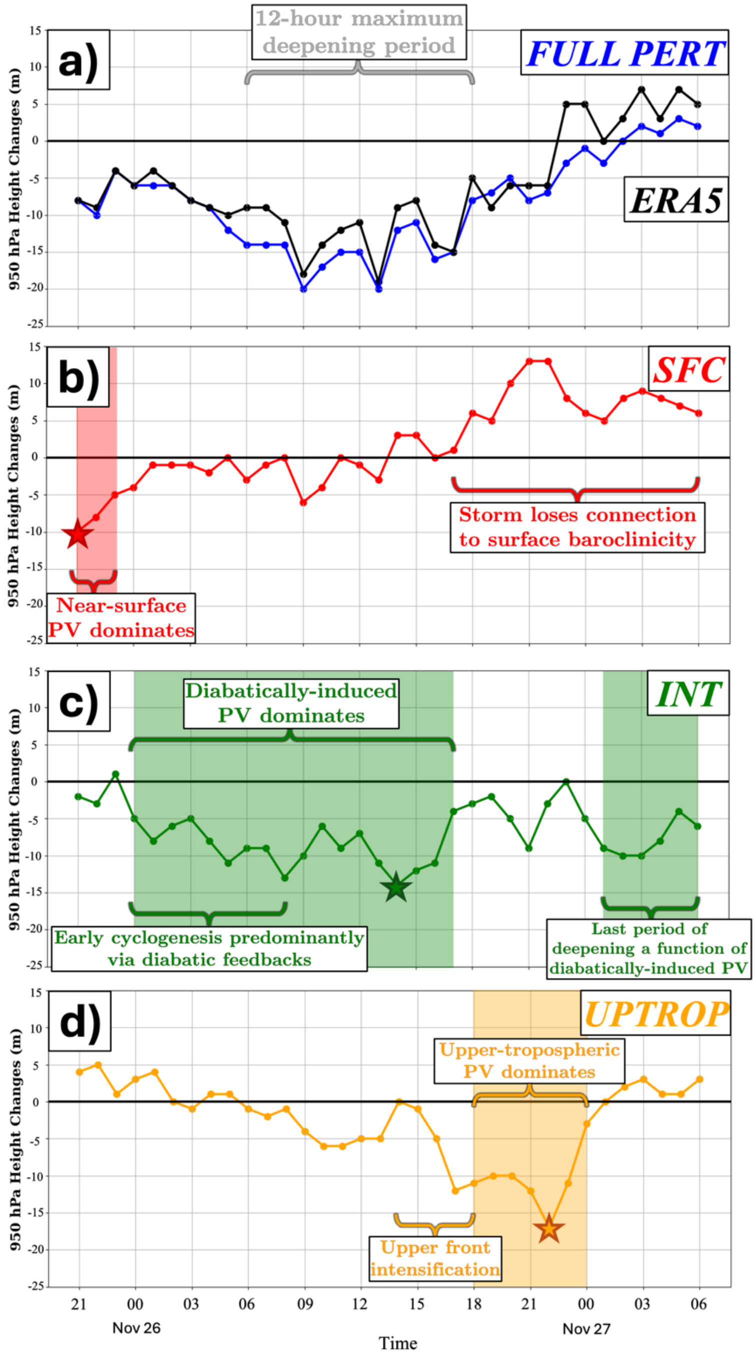

Fig. 2.11. 950 hPa 1-hourly height changes from the inversion of the pieces of the perturbation PV at the location of the 950 hPa vorticity maximum of the November 2019 storm. (a) 950 hPa 1-hourly height changes from the inversion of the FULL PERT PV (blue) as defined in Section 3 (see text) along with the observed ERA5 1-hourly height changes (black). Notable time period(s) are annotated. (b) As in (a) but for 1-hourly height changes associated with the SFC PV. Red shading indicates the time period in which the SFC PV contributed the most negative 950 hPa height changes of all three perturbation PV pieces. Red star indicates the time of most negative 950 hPa 1-hourly height change from the SFC PV inversion. (c) As in (b) but for 1-hourly height changes associated with the INT PV. Green shading indicates time periods in which the INT PV contributed the most negative 950 hPa height changes of all three perturbation PV pieces. Green star indicates the time of most negative 950 hPa 1-hourly height change from the INT PV inversion. (d) As in (c) but for 1-hourly height changes associated with the UPTROP PV. Orange shading indicates the time period in which the UPTROP PV contributed the most negative 950 hPa height changes of all three perturbation PV pieces. Orange star indicates the time of most negative 950 hPa 1-hourly height change from the UPTROP PV inversion.

Perturbation height changes from the ERA5 data and the inversion of the full perturbation PV were negative at the location of the 950 hPa vorticity maximum for a majority of the 33-hour analysis period, with peak negative values occurring between 0900 UTC and 1300 UTC 26 November before exhibiting a steady increase until the end of the analysis period (Fig. 2.11a). The ERA5 and the full perturbation PV inversion height changes were in very good agreement. The 12-hour maximum deepening period spanned from 0600 UTC to 1800 UTC 26 November, with the storm having experienced consecutive MSLP falls greater than 1 hPa hr^{-1} beginning at 0900 UTC 26 November until making landfall. The influence of surface potential temperature anomalies on near-surface height changes were initially negative, and then were negligible until the NV19 storm lost connection to surface baroclinicity after 1600 UTC 26 November (Fig. 2.11b). Diabatically-induced PV had the most dominant influence throughout an overwhelming majority of the development (Fig. 2.11c). Near-surface height changes associated with the INT PV residual were negative beginning at 0000 UTC 26 November until the end of the storm lifecycle, including throughout the entire 12-hour maximum deepening period. In fact, INT PV contributed the most negative height changes during the early and late stages of cyclogenesis (Fig. 2.11). The influence of the upper-tropospheric and stratospheric PV (the UPTROP PV) on near-surface height changes was minimal until 1500 UTC 26 November, by which time the developing upper-level jet/front system had finally encroached upon the NV19 storm, quickly inducing strong negative height changes (Fig. 2.11d). These height changes were the most negative of any associated with the three pieces of the perturbation PV directly outside of the 12-hour maximum deepening period. Interrogations of the various physical mechanisms responsible for this period of development, including potential interaction between the lower-tropospheric DRW vortex and the upper-level jet/front system, which initially developed independently of each other, will be explored separately in future work.

2.4.3. Mutual amplification

The influence of specific PV anomalies (i.e., UPTROP, INT, and SFC) on the strength of the flow throughout the column is described via the PV superposition principle (Davis and Emanuel 1991; Morgan and Nielsen-Gammon 1998). The anomalous flow associated with, for instance, an UPTROP PV anomaly can interact with the INT PV distribution (at a given isobaric level) to amplify the magnitude of the INT PV anomaly via horizontal advection. In a statically stable atmosphere, local increases in EPV translate to increases in cyclonic circulation. Additionally, positive advection of lower boundary potential temperature anomalies by any discrete portion of the balanced flow will induce similar increases in cyclonic circulation (Bretherton 1966). Therefore, any location experiencing positive advection of perturbation EPV by a balanced flow, which would increase the anomalous EPV there, will also experience an increase in the perturbation cyclonic circulation. Any such increase is a manifestation of the PV superposition principle and is labeled mutual cyclonic amplification.

The hour at which the associated perturbation height changes are most negative for the UPTROP, INT, and SFC PV (indicated by the starred times in Fig. 2.11b-d) are considered next. The analysis assesses if such favorable superposition amongst the various balanced flows attributable to the UPTROP, INT, and SFC PV contributed to an increase in the cyclonic flow throughout the column at these times during the NV19 storm.

2.4.3.1. 2100 UTC 25 November 2019

The initial near-surface height changes of the NV19 storm, from 2100 UTC to 2300 UTC 25 November, were predominantly driven by the influence of lower-boundary PV (Fig. 2.11b). The most negative of these 950 hPa height changes occurred at 2100 UTC 25 November, which corresponds to the time of initial formation of the SLP minimum which became the NV19 cyclone. Cyclonic PV advection (CPVA) by the balanced flow at three different isobaric levels from the inversion of the UPTROP and SFC PV and the INT PV residual at 2100 UTC 25 November are shown in Fig. 2.12. The yellow contours on each of the nine panels indicate where there is either appreciable CPVA or positive surface potential temperature advection by the balanced flow from a specified perturbation PV anomaly at the given isobaric level. In the upper troposphere, the balanced flows from the UPTROP and INT resulted in CPVA of upper-tropospheric PV to the north of the NV19 storm (Fig. 2.12a,b) while upper-tropospheric CPVA from the SFC balanced flow was occurring well to the northwest of the storm (Fig. 2.12c). No distinct diabatically-induced PV anomaly had formed in the mid-troposphere early in the storm lifecycle, so no notable cyclonic advection of this type of PV was occurring (Fig. 2.12d-f). Cyclonic advection of lower-boundary PV by the UPTROP and INT balanced flows was not occurring in the vicinity of the NV19 storm (Fig. 2.12g,h). Only the balanced flow from the SFC was resulting in lower-boundary CPVA immediately over the NV19 storm center (Fig. 2.12i). Therefore, at this early time in storm development, lower-boundary CPVA was being amplified only by SFC anomalies and no substantial mutual cyclonic amplification of PV anomalies throughout the depth of the troposphere was occurring.

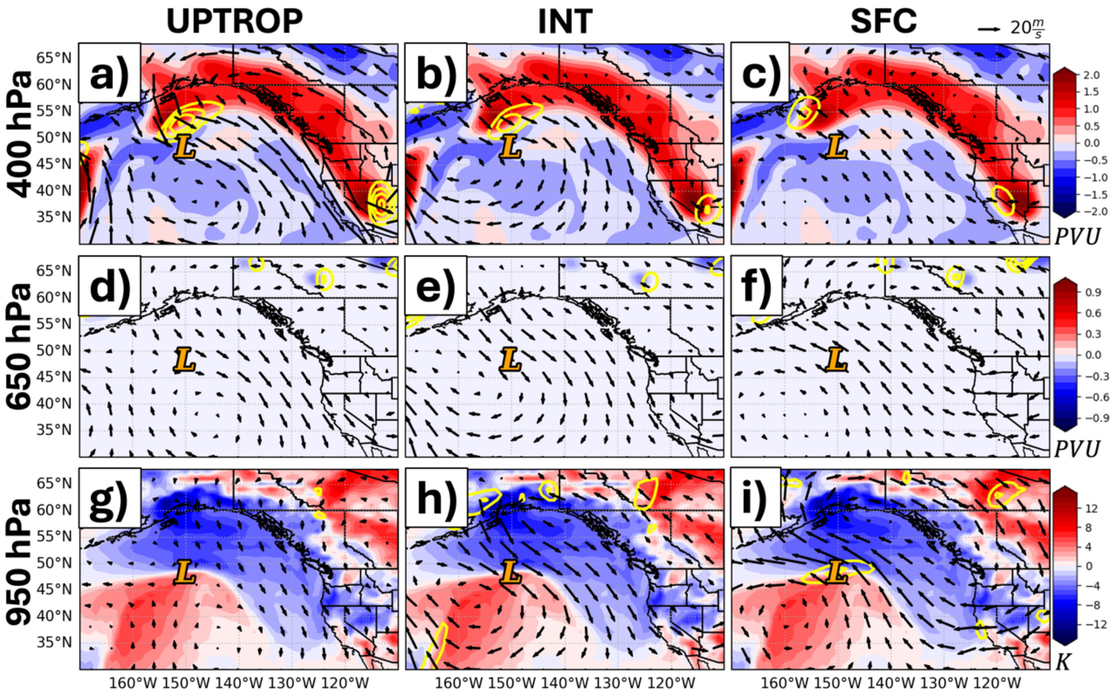

Fig. 2.12. Balanced flow attributable to the UPTROP, INT, and SFC perturbation PV and the influence of that balanced flow on the 3D PV and potential temperature anomaly structure valid at 2100 UTC 25 November 2019. (a-c) 400 hPa UPTROP PV anomalies shaded every 0.25 PVU (1 PVU = 1×10^{-6} m^2 s^{-1} K kg^{-1}) starting at 0.25 PVU and 400 hPa balanced flow (arrows) from the inversion of the (a) UPTROP, (b) INT, and (c) SFC. Yellow, solid contours represent positive UPTROP PV advection by the (a) UPTROP, (b) INT, and (c) SFC balanced flows contoured every 0.1 PVU hr^{-1} starting at 0.1 PVU hr^{-1}. Location of the 950 hPa relative vorticity maximum indicated by the orange 'L'. (d-f) 650 hPa INT PV anomalies shaded every 0.1 PVU starting at 0.1 PVU and 650 hPa balanced flow (arrows) from the inversion of the (d) UPTROP, (e) INT, and (f) SFC. Yellow, solid contours represent positive INT PV advection by the (d) UPTROP, (e) INT, and (f) SFC balanced flows contoured every starting 0.1 PVU hr^{-1} at 0.1 PVU hr^{-1}. Location of the 950 hPa relative vorticity maximum indicated by the orange 'L'. (g-i) 975 hPa potential temperature anomalies (SFC PV anomalies) shaded every 1 K and the 950 hPa balanced flow from the inversion of the (g) UPTROP, (h) INT, and (i) SFC as represented by the arrows. Yellow, solid contours represent positive surface potential temperature advection by the (g) UPTROP, (h) INT, and (i) SFC balanced flows contoured every 1 K hr^{-1} starting at 1 K hr^{-1}. Location of the 950 hPa relative vorticity maximum indicated by the orange 'L'.

2.4.3.2. 1400 UTC 26 November 2019

A majority of the subsequent cyclogenesis in terms of 950 hPa height changes was attributable to diabatically-induced PV, which dominated near-surface intensification from 0000 UTC to 1600 UTC 26 November (Fig. 2.11c). Near-surface 1-hourly height changes associated with the diabatically-induced PV were most negative at 1400 UTC 26 November, which was during the last hours of the 12-hour period of most rapid deepening. At that time, the balanced flows from the inversion of the UPTROP and INT residual were responsible for CPVA of upper-tropospheric PV directly over the NV19 storm (Fig. 2.13a,b) while the balanced flow from the inversion of SFC induced CPVA well to the northwest (Fig. 2.13c). By this time, diabatic heating had generated a notable cyclonic mid-tropospheric PV anomaly due east of the surface cyclone. CPVA by the UPTROP and INT balanced flows was occurring to the east-southeast of the storm center (Fig. 2.13d,e). Advection of this mid-tropospheric PV by the balanced SFC winds was also occurring directly northeast of the storm (Fig. 2.13f). No appreciable advection of lower-boundary potential temperature by the UPTROP winds was occurring at this time (Fig. 2.13g). The balanced flow attributable to the INT resulted in lower-boundary CPVA to the southeast of the NV19 storm (Fig. 2.13h) while the SFC winds resulted in lower-boundary CPVA directly over the NV19 storm (Fig. 2.13i). Mutual cyclonic amplification throughout the column was ongoing at this time as CPVA induced by both UPTROP and INT was occurring in the upper-troposphere (Fig. 2.13a,b), CPVA induced by UPTROP, INT, and SFC was evident in the mid-troposphere (Fig. 2.13d-f) and CPVA induced by INT and SFC was ongoing in the lower-troposphere (Fig. 2.13h,i).

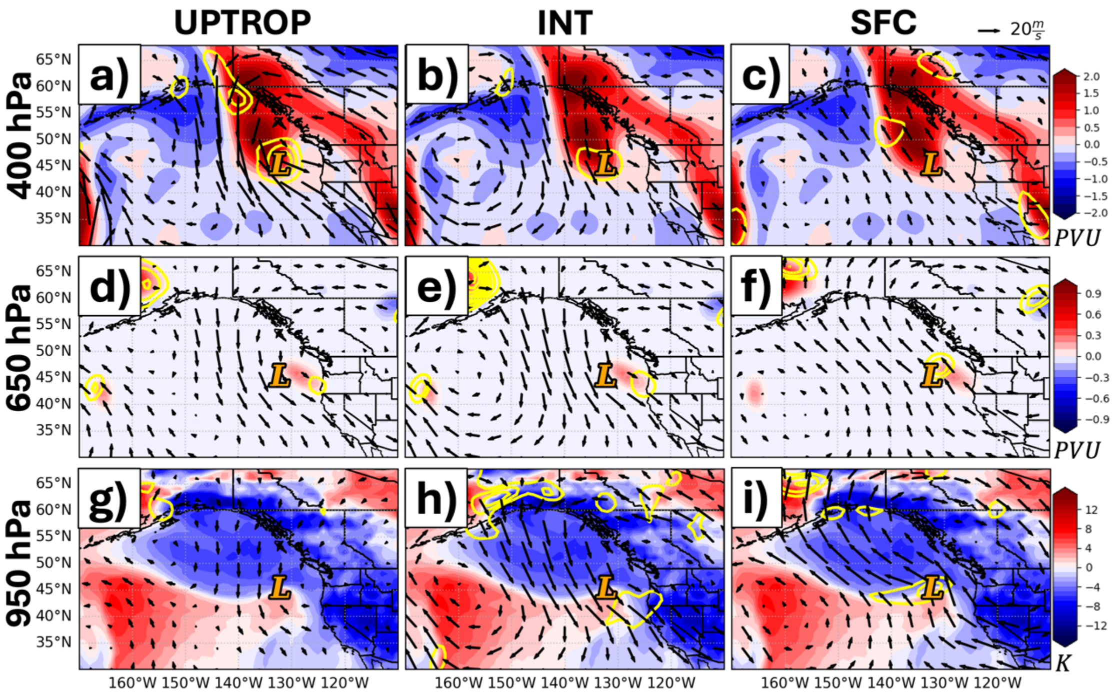

Fig. 2.13. (a) As in Fig. 2.12a except for 1400 UTC 26 November 2019. (b) As in Fig. 2.12b except for 1400 UTC 26 November 2019. (c) As in Fig. 2.12c except for 1400 UTC 26 November 2019. (d) As in Fig. 2.12d except for 1400 UTC 26 November 2019. (e) As in Fig. 2.12e except for 1400 UTC 26 November 2019. (f) As in Fig. 2.12f except for 1400 UTC 26 November 2019. (g) As in Fig. 2.12g except for 1400 UTC 26 November 2019. (h) As in Fig. 2.12h except for 1400 UTC 26 November 2019. (i) As in Fig. 2.12i except for 1400 UTC 26 November 2019.

2.4.3.3. 2200 UTC 26 November 2019

Upper-tropospheric PV anomalies dominated near-surface development directly following the 12-hour most rapid deepening period of the NV19 storm (Fig. 2.11d). Near-surface 1-hourly height changes from the inversion of the UPTROP peaked at 2200 UTC 26 November, which was nearly coincident with the time at which the upper-level jet/front system was most intense (not shown). At this time, the winds associated with UPTROP and INT induced CPVA to the east and south of the NV19 storm, respectively (Fig. 2.14a,b). There was again no advection of upper-tropospheric PV by the SFC balanced flow near the storm at this time (Fig. 2.14c). Diabatically-induced PV anomalies in the mid-troposphere were weaker at this time, with mid-tropospheric CPVA from each piece of the perturbation flow occurring to the east of the storm center (Fig. 2.14d-f). Lower-boundary CPVA from the UPTROP and INT balanced flows was situated to the southeast of the NV19 storm center (Fig. 2.14g,h) with no substantial lower-boundary CPVA arising from the SFC balanced flow (Fig. 2.14i). Therefore, it appears that mutual cyclonic amplification was primarily occurring in the mid-troposphere (Fig. 2.14d-f) and upper-troposphere (Fig. 2.14a,b) late in the development of the cyclone.

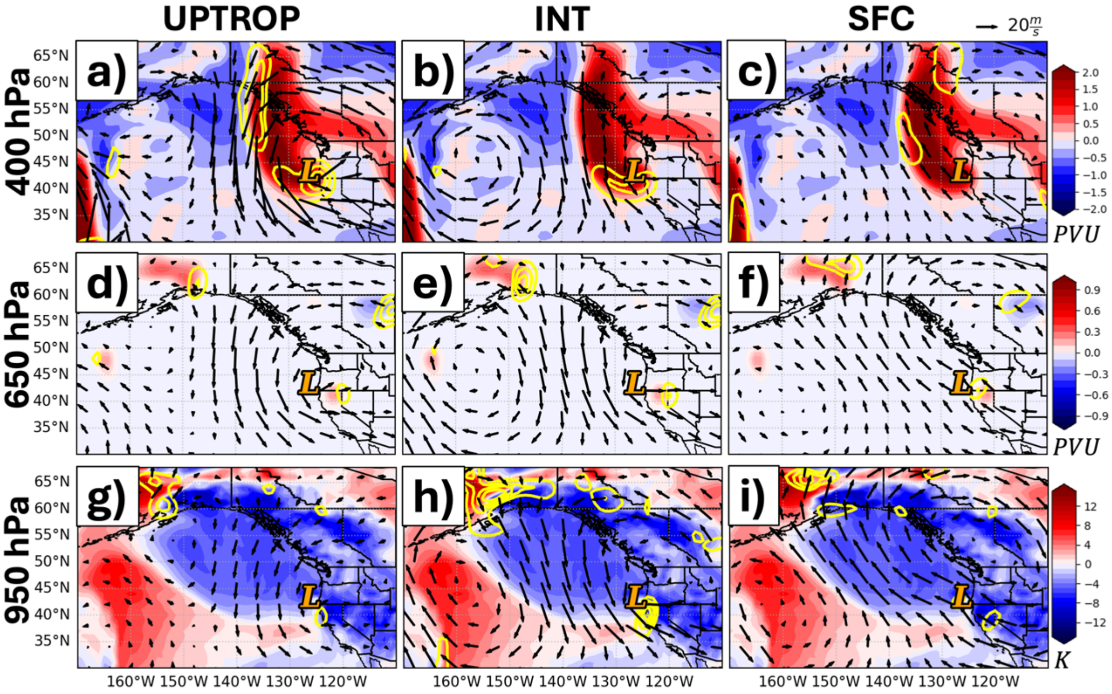

Fig. 2.14. (a) As in Fig. 2.13a except for 2200 UTC 26 November 2019. (b) As in Fig. 2.13b except for 2200 UTC 26 November 2019. (c) As in Fig. 2.13c except for 2200 UTC 26 November 2019. (d) As in Fig. 2.13d except for 2200 UTC 26 November 2019. (e) As in Fig. 2.13e except for 2200 UTC 26 November 2019. (f) As in Fig. 2.13f except for 2200 UTC 26 November 2019. (g) As in Fig. 2.13g except for 2200 UTC 26 November 2019. (h) As in Fig. 2.13h except for 2200 UTC 26 November 2019. (i) As in Fig. 2.13i except for 2200 UTC 26 November 2019.

2.4.4. Summary

The foregoing analysis reveals that the early propagation of the NV19 DRW was facilitated by column stretching tied to lower-tropospheric frontogenesis along the pre-existing baroclinic zone. This frontogenesis was predominantly forced by differential temperature advection associated with the UPTROP balanced flow at 1200 UTC 25 November, and then by the SFC balanced flow at 0000 UTC 26 November 2019, at the start of DRW intensification. Analysis of the near-surface height changes suggests that the diabatically-induced INT PV was the most prominent contributor to near-surface height changes during the intensification of the NV19 storm. The upper-tropospheric/lower-stratospheric UPTROP PV contributed the most to near-surface height changes during the last 12 hours of storm intensification just prior to landfall. The lower-tropospheric SFC PV influenced near-surface height changes only very early in the development. Since the SFC PV isolates the effects of lower-boundary θ anomalies, which are influenced by near-surface heat fluxes, the piecewise PV inversion presented here suggests that such fluxes exerted only a marginal influence on intensification of the NV19 storm.

This suggestion is supported by consideration of ERA5 surface sensible heat data across a $10° \times 10°$ box centered on the NV19 MSLP minimum throughout its evolution. Surface sensible heat flux anomalies are calculated with respect to two different time means: 1) from 1200 UTC 25 November to 0000 UTC 28 November 2019, which captures the entire NV19 storm lifecycle, and 2) from 0000 UTC 01 November to 2300 UTC 31 December 2019, the 2-month time mean. Employing the first time mean approach, surface sensible heat flux was anomalously negative throughout the majority of the NV19 storm evolution and was only positive between 0900 and 1600 UTC 26 November 2019 (Fig. 2.15). Using the 2-month time mean, anomalous surface sensible heat flux was negative throughout the entire NV19 lifecycle (Fig. 2.15). Thus, the surface sensible heat flux was anomalously negative for at least a majority, or perhaps all, of the NV19 lifecycle. This marginal influence of both near-surface and surface heat fluxes is a notable difference from previous piecewise PV inversions of DRW explosive cyclogenesis events (Moore et al. 2008; Rivière et al. 2010). The anomalously negative surface sensible heat flux also suggests that the Blob 2.0 MHW over the North Pacific (e.g. Amaya et al. 2020; Chen et al. 2021), which first peaked in November 2019, had minimal direct impact on heat flux into the NV19 storm. It is quite possible, however, that the Blob 2.0 MHW could have enhanced the background baroclinicity across the northeast Pacific basin through reduced but persistent surface heat flux as it reached peak intensity for the first time. Future work is needed to confirm or refute this suspicion.

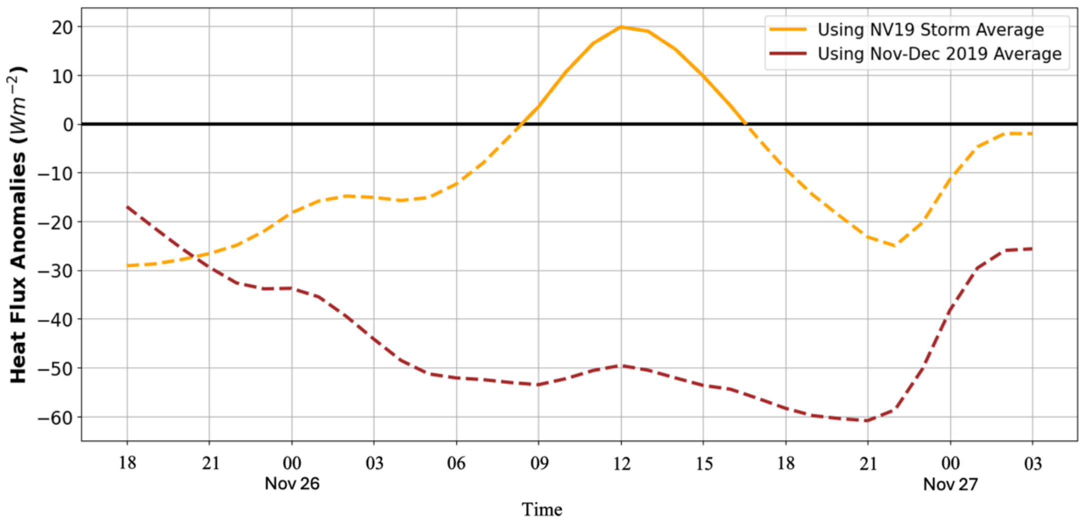

Fig. 2.15. Surface sensible heat flux anomalies ($W\,m^{-2}$) from 1800 UTC 25 November to 0300 UTC 27 November 2019 averaged across a $10° \times 10°$ box centered on the NV19 storm. Surface sensible heat flux anomaly relative to the NV19 storm time mean (1200 UTC 25 November to 0000 UTC 28 November 2019) is contoured in solid orange with negative surface sensible heat flux anomaly represented by dashed contours. Surface sensible heat flux anomaly relative to the 2-month time mean (0000 UTC 01 November to 2300 UTC 31 December 2019) is contoured in solid brown with negative surface sensible heat flux anomaly represented by dashed contours.

It is also suggested that mutual amplification between discrete pieces of perturbation PV progressed from the lower to the upper-troposphere as the NV19 storm experienced a 29-hour period of uninterrupted 950 hPa height falls. This progression is visualized in schematic form in Fig. 2.16 with the colored illustrations representing each piece of the perturbation PV and similarly colored arrows indicating the strength and at which isobaric levels that piece of the perturbation PV contributed to mutual amplification.

Early in the lifecycle, only the balanced flow from the INT PV contributed to amplification of another PV anomaly, namely the UPTROP PV (Fig. 2.16a). Therefore, *mutual* amplification was relatively absent. As the storm began its period of rapid intensification, *mutual* amplification became more pervasive as the balanced flow associated with the UPTROP PV amplified the INT PV anomaly, the balanced flow associated with the INT PV amplified both the UPTROP PV and SFC PV anomalies, and the balanced flow associated with the SFC PV served to amplify the INT PV anomaly (Fig. 2.16b). The mutual amplification signal at this time was strongest from the SFC PV. Towards the end of the rapid deepening period, the balanced flow associated with the SFC PV continued to amplify the INT PV anomaly, but the predominant mutual amplification involved the INT PV and UPTROP PV acting throughout the column (Fig. 2.16c). At this later time, the mutual amplification signal was strongest in association with the mid- to upper-tropospheric PV anomalies. The strength of the INT PV mutual amplification escalated as the NV19 storm matured and the influence of the UPTROP PV mutual amplification progressively extended throughout the whole depth of the troposphere (Fig. 2.16). The absence of an initial upper-tropospheric cyclogenetic precursor, coupled with the upward march of dominant developmental processes, suggests that the NV19 storm underwent a bottom-up development like that of *Lothar* (Wernli et al. 2002). Also, the NV19 storm propagated in the direction of the lower-tropospheric diabatically-generated PV anomaly which was located to the east (Fig. 2.13d-f) and southeast (Fig. 2.14d-f) of the cyclone center, fitting with the DRW propagation mechanism explained in Tamarin and Kaspi (2016) but with an equatorward rather than a poleward track.

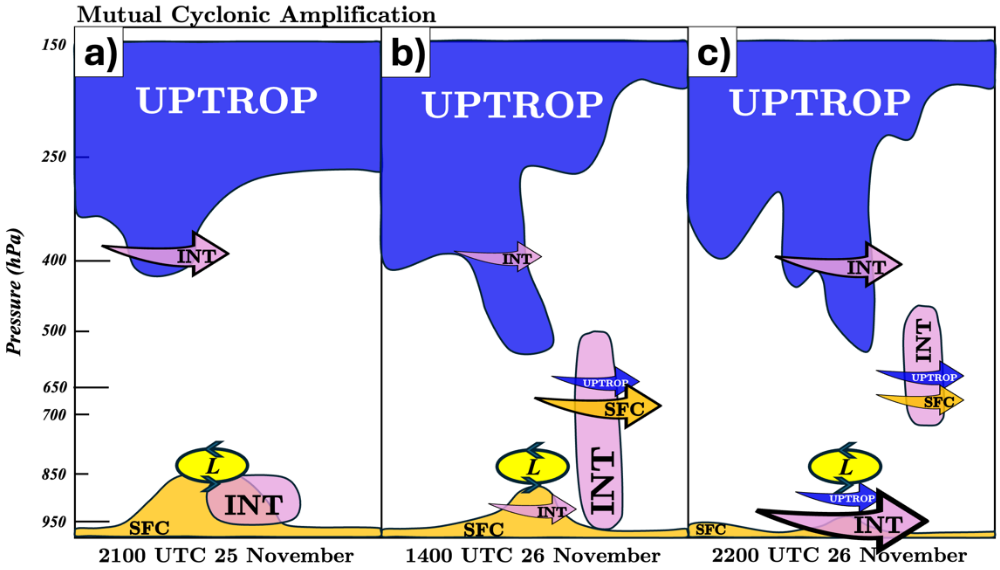

Fig. 2.16. Schematic of mutual cyclonic amplification during the development of the November 2019 Northeast Pacific bomb cyclone. Orange, pink, and blue shapes represent the positive perturbation potential vorticity (PV) of the SFC, INT, and UPTROP PV, respectively, throughout the

troposphere and lower stratosphere (see text for definition of SFC, INT, and UPTROP). Orange, pink, and blue arrows indicate the perturbation balanced flow of the SFC, INT, and UPTROP PV, respectively, which is resulting in mutual cyclonic amplification at a specific isobaric level. Size of arrow indicates relative strength of mutual cyclonic amplification. Yellow oval and "L" represents location of November 2019 Northeast Pacific bomb cyclone center. (a) Mutual cyclonic amplification valid at 2100 UTC 25 November 2019. (b) Mutual cyclonic amplification valid at 1400 UTC 26 November 2019. (c) Mutual cyclonic amplification valid at 2200 UTC 26 November 2019.

2.5. Conclusions and Discussion

Piecewise PV inversion of an extratropical cyclone in late November 2019 reveals a case of explosive DRW development that was predominantly a function of the influence of diabatic generation of PV associated with latent heat release. Only the late stages of cyclogenesis were dominated by upper-tropospheric and lower-stratospheric PV associated with an upper-level jet/front system. Analysis of the piecewise frontogenesis, the 1-hourly height changes at the location of the 950 hPa vorticity maximum, and mutual cyclonic amplification between perturbation PV anomalies in different layers of the troposphere suggest that the NV19 storm followed a bottom-up development similar to that described by Wernli et al. (2002) in association with *Lothar*. The current study is, to the authors' knowledge, unique in that it interrogates the nature of an explosive DRW development over a cold ocean surface.

Specific findings from the case study include:

1) The development of the NV19 storm was unusual in several ways; the storm track was notably out of phase with other EC events in the northeast Pacific Ocean and the typical DRW propagation direction, the deepening rate ranked higher than the 90th percentile in two separate climatologies, and the maximum deepening location of this storm occurred further east than any other EC event over the northeast Pacific Ocean in a non-consecutive 30-year period.
2) Piecewise frontogenesis analysis, or frontogenesis calculated using the balanced flows from the full column perturbation PV and the three partitioned pieces of the perturbation PV, reveals that frontogenesis along the baroclinic zone stretching across the northeast Pacific Ocean was predominantly a function of balanced winds associated with the UPTROP PV prior to NV19 storm formation and then almost entirely a function of balanced winds associated with the SFC PV as the

storm formed and began to strengthen. Thus, the dominant forcing for the lower-tropospheric frontogenesis that mobilized the DRW was transferred from the upper-troposphere prior to initial cyclogenesis to the surface layer once more substantial development had begun.

3) Height falls associated with lower-tropospheric PV dominated in the very early stages of cyclogenesis via the northward transport of high θ (θ_e) air along the cold front of a cutoff cyclone situated to the west of an expansive anticyclone. There was no signal of mutual cyclonic amplification between perturbation PV anomalies throughout the troposphere during this initial formation as the lower-tropospheric DRW formed.
4) Diabatic generation and rearrangement of PV throughout the depth of the troposphere dominated near-surface height falls over the subsequent 16-hour period. These diabatic feedbacks were in response to vigorous lower-tropospheric frontogenesis which was situated along the warm front of the NV19 storm. The diabatic feedbacks conspired to force mutual cyclonic amplification of perturbation PV anomalies notably extending throughout the depth of the troposphere. This period encompassed the entire 12-hour maximum deepening period during which the storm deepened 34 hPa as it moved southeastward.
5) The final period of development was dominated by upper-tropospheric PV associated with an intense upper-level jet/front system which focused vigorous CVA by the thermal wind directly over the surface cyclone as it approached the coast. Mutual cyclonic amplification was primarily occurring between perturbation PV anomalies in the mid- and upper-troposphere during this final period of deepening.
6) The direct effects of near-surface heat fluxes, which are indirectly included in the SFC PV by its definition, were quite unimportant to storm intensification in this case of explosive DRW cyclogenesis. In fact, in contrast to previous piecewise PV inversion studies on rapidly deepening DRWs (Moore et al. 2008; Rivière et al. 2010), the SFC PV was the least important forcing for 950 hPa height falls after the very initial stages of cyclogenesis. This result suggests that explosive

DRW developments over a cold ocean rely either on different circumstances or a different sequencing of forcings than explosive DRWs that develop over a warm ocean.

Like *Lothar*, the NV19 storm featured a bottom-up rapid intensification of a DRW dependent upon diabatic generation of lower-tropospheric PV to spawn a potent surface cyclone. DRW bottom-up rapid developments resemble the type-C cyclogenesis events described in Plant et al. (2003) wherein cyclone intensification is driven by latent heat release, with the addition of strong lower-tropospheric baroclinicity (Boettcher and Wernli 2013; Tamarin and Kaspi 2016). Despite several similarities, the NV19 storm did not follow the same developmental sequence as *Lothar*. Wernli et al. (2002) showed that the circulation attributable to the lower-tropospheric PV anomaly of *Lothar*, which was produced via intense latent heating, was substantial enough to extend to the jet level and aid in the formation of an upper-tropospheric PV anomaly which then further intensified the low-level PV anomaly through PV superposition (Davis and Emanuel 1991; Morgan and Nielsen-Gammon 1998). Though the preceding analysis does not consider the problem directly, it appears that both the lower- and upper-tropospheric PV anomalies associated with the lower-tropospheric DRW vortex and upper-level jet/front system, respectively, initially intensified independently of one another. Additionally, it does not appear that the lower-tropospheric PV anomaly forced the development of the upper-tropospheric PV anomaly, as was the case with *Lothar*, despite appearing to follow a similar bottom-up development.

Systematic investigation of whether, and to what degree, the simultaneously strengthening lower-tropospheric DRW vortex and upper-level jet/front system had notable influences on one another during the NV19 development is a topic for future work. Specific analysis will focus on whether the circulation associated with the lower-tropospheric DRW vortex contributed to a mobilization of the "Shapiro effect" (Rotunno et al. 1994) thereby instigating the development of the upper-level jet/front system when the two features superposed. This proposition will be explored using piecewise PV inversion in a forthcoming, complimentary study on this unusual cyclogenesis event.

POSTSCRIPT

As the current study neared completion, a DRW over the northeastern Pacific Ocean underwent explosive cyclogenesis from 1200 UTC 18 November to 0000 UTC 20 November 2024. This event displayed striking dynamical similarities to the event presented in this paper, including a similar structural evolution and very rapid intensification. At 1200 UTC 18 November, the cyclone developed along a zonally-oriented baroclinic zone which bisected an anticyclone over the northeast Pacific and was initially driven by lower-tropospheric latent heat release. By 0000 UTC 19 November, an upper-tropospheric shortwave had moved into close proximity to the DRW and focused substantial CVA by the thermal wind (Sutcliffe 1947) over the cyclone center. In the subsequent 24 hours, the cyclone deepened an additional 66 hPa, including a 26 hPa pressure fall between 1200 UTC and 1800 UTC 19 November, matching the maximum 6-hour deepening rate accomplished by the *Braer* storm. The result was an impressive 945 hPa cyclone situated off the Washington, USA and British Columbia coastline.

Both the NV19 storm and this recent event originated as innocuous-looking warm frontal waves, perhaps both as DRWs. Intense and geographically restricted lower-tropospheric frontogenesis produced heavy precipitation which, in turn, generated lower-tropospheric positive PV anomalies along the front. These anomalies orchestrated a period of modest growth before both cyclones were overtaken by potent tropopause-level disturbances which facilitated ascent and the stretching of vorticity-rich air that drove the rapid cyclogenesis.

Further investigation of this extraordinary storm is ongoing with the goal of determining the physical importance of the similarities that appear to characterize these two extreme events.

3. The Development and Influence of an Upper-Level Jet/Front on Rapid Cyclogenesis

3.1. Introduction

The analysis presented in Chapter 2 describes the lifecycle of a record-setting extratropical cyclogenesis event that occurred over the northeast Pacific Ocean in late November 2019 from a piecewise potential vorticity (PV) perspective. It was shown that the cyclone of interest began as a diabatic Rossby wave (DRW) mobilized by localized lower-tropospheric frontogenesis along a pre-existing baroclinic zone. After a period of eastward propagation characterized by little surface development, the cyclone began an extended period of rapid development upon becoming favorably aligned with an intensifying upper-level jet/front system (ULJF) that developed in north-northwesterly flow over the Gulf of Alaska. The analysis in Chapter 2 found that development followed a bottom-up sequencing by which near-surface PV dominated initial cyclogenesis, diabatically-induced PV controlled a prolonged interval of subsequent intensification, and upper-tropospheric PV dominated the final period of development.

The existence of upper-tropospheric frontal structures that are essentially independent of the surface frontal zones described by the Norwegian Cyclone Model (Bjerknes and Solberg 1922) has been known for some time (e.g. Reed and Sanders 1953; Newton 1954; Reed 1955; Reed and Danielsen 1958). These pioneering studies hypothesized that differential vertical motion, with subsidence preferentially on the warm side of an upper-level baroclinic zone, was responsible for tilting both vertical shear and vertical potential temperature gradients into the horizontal. The result of such differential subsidence was a local increase in baroclinicity, an increase in absolute vorticity, and a downward penetration of stratospheric potential vorticity (PV). These are the essential structural elements of what have come to be known as upper-level jet/front (ULJF) systems by virtue of the frontal zone's connection to the tropopause-level jet stream (Shapiro 1981). Though the development of ULJFs has been directly indicted as a predecessor to lower-tropospheric cyclogenesis via its connection to the emergence of the associated mid-tropospheric wave and attendant vorticity maxima, the direct role, via CVA by the thermal wind, of a developing ULJF on surface cyclogenesis has not been as closely examined.

At its core, lower-tropospheric cyclogenesis depends on the evacuation of mass from an atmospheric column which compels near-surface convergence and an associated spin-up of cyclonic vorticity. Thus, a non-uniform distribution of synoptic-scale vertical motion is necessary to instigate cyclogenesis. In one of the earliest dynamical treatments of the subject, Sutcliffe (1947) identified thermal wind advection of geostrophic vorticity as a primary forcing for the production of the requisite mid-latitude vertical motions. Subsequent investigations (e.g. Trenberth 1978; Hoskins et al. 1978; Martin 1998) have reiterated this fundamental insight in a variety of alternative forms. It is the primacy of CVA by the thermal wind in forcing mid-latitude ascent that vests ULJF development with such potency with respect to lower-tropospheric cyclogenesis.

ULJF development preferentially occurs in the presence of geostrophic cold air advection in cyclonic shear (Keyser and Shapiro 1986), a synoptic circumstance that mobilizes what Rotunno et al. (1994) called the "Shapiro effect" – the production of a transverse secondary ageostrophic circulation that encourages subsidence on the warm side of the developing ULJF. In a recent examination of ULJF development, Martin (2014) showed that tilting forced by geostrophic cold air advection in cyclonic shear is physically identical to geostrophic shear vorticity advection by the thermal wind and that this form of shearwise ω is the predominant source of frontogenetic tilting in the ULJF environment. Since tilting increases both the horizontal temperature gradient and the vertical vorticity along a quasi-2D frontal zone of finite length, the downshear end of that ULJF stands to experience a continual increase in CVA by the thermal wind throughout the ULJF development period. The increasing CVA by the thermal wind, in turn, encourages more robust ascent, enhanced mass evacuation and intensified lower-tropospheric cyclogenesis – also on the downshear end of the ULJF.

Though identified as a prominent feature in the lifecycle of the NV19 storm, the development of the ULJF, and the piecewise contributions to that development, were not included in Chapter 2. Prior work has examined the interaction between DRWs and upper-tropospheric troughs (e.g. Wernli et al.

2002; Moore et al. 2008; Rivière et al. 2010; Boettcher and Wernli 2011, 2013; McKenzie 2014; Tamarin and Kaspi 2016; Zhang and Wang 2018), as well as the interaction of discrete upper- and lower-tropospheric circulation and thermal anomalies on the development of an ULJF within the context of an explosive cyclogenesis event (Huo et al. 1999; Boettcher and Wernli 2013; Fu et al. 2014; Heo et al. 2015). The novelty of the current study is that we first isolate the circulation and thermal anomalies attributable to discrete pieces of the PV associated with distinct physical processes. We then assess the contribution of these anomalies on the development of an ULJF within the context of a rapid cyclogenesis event involving the interaction between a DRW and an upper-tropospheric trough.

The present Chapter examines aspects of both the influence of the ULJF system on the developmental life cycle of the November 2019 storm as well as the influences of the various pieces of the perturbation PV field (e.g., their balanced flow and thermal anomalies) on the development of the influential ULJF that characterized this case. The presentation begins in Section 3.2 with a short description of the data and the piecewise PV inversion method employed here. Section 3.3 provides a short synoptic description of the event emphasizing the role of the ULJF on the cyclogenesis. After establishing its substantial influence, Section 3.4 presents a quasi-geostrophic omega-based analysis of the ULJF development utilizing the kinematic and thermal anomaly fields derived from the piecewise PV inversion analysis of Chapter 2. Conclusions and suggestions for further analysis are offered in Section 3.5.

3.2. Data and Methods

3.2.1. Dataset

Wind speed and direction, temperature, geopotential height, relative humidity, and MSLP data for the NV19 storm were extracted on a limited area domain extending from 10°N to 75°N and 180° to 90°W from the hourly ECMWF reanalysis version 5 (ERA5; Hersbach et al. 2020) data set obtained from the Copernicus Climate Data Store. The analysis employs this hourly ERA5 data at 1-hour intervals from 0000 UTC 1 November to 2300 UTC 31 December 2019 with horizontal grid spacing of 0.25° x 0.25°

and 19 vertical levels from 1000 hPa to 100 hPa at 50 hPa intervals. ERA5 data were then regridded to a grid spacing of 1.0° × 1.0° as coarse data with smooth gradients is more amenable to the PV inversion process (Hoskins et al. 1985) as well as the calculation of QG-omega (Martin 1999).

3.2.2. Piecewise PV inversion

Ertel (1942) expressed the potential vorticity, first formulated by Rossby (1940) as

$$EPV = -g(\zeta_\theta + f)\frac{\partial\theta}{\partial p},$$

where g is gravitational acceleration, ζ_θ is the isentropic relative vorticity, f is the planetary vorticity, $-\frac{\partial\theta}{\partial p}$ is a measure of the static stability, and EPV stands for Ertel PV. EPV is conserved for adiabatic, inviscid flow. Information about the flow associated with a distribution of EPV can be extracted through the process of PV inversion (Hoskins et al. 1985; Davis and Emanuel 1991). Details about the PV inversion method used in this study are described in depth in Chapter 2 and will not be repeated here in the interests of brevity.

In order that the PV inversion operation be accurately described as "piecewise", discrete pieces of the PV must be identified and inverted separately. The present work, derived as it is from the study of Chapter 2, follows a modified version of the piecewise partitioning described in Davis (1992), Korner and Martin (2000), and Winters and Martin (2017) which employ both isobaric and relative humidity criteria. The details of the scheme are described in Chapter 2 and result in three pieces of the perturbation PV; UPTROP (for the upper tropospheric PV, PV in unsaturated air in the 650 to 150 hPa layer), INT (for the diabatically-generated PV, PV in saturated air in the 950 to 150 hPa layer), and SFC (for the "surface" PV, PV in unsaturated air in the 950 to 700 hPa layer including perturbation θ on the bottom boundary of the domain). Finally, as in Chapter 2, inversion of the INT PV is not performed and geopotential and streamfunction anomalies associated with that piece of the total perturbation PV are calculated as differences between the full inversion values of each variable and the sum of the SFC and UPTROP values of each variable.

3.2.3. Quasi-geostrophic omega diagnostics

Gridded analyses from the piecewise PV inversion analysis, derived from the ERA5 dataset, are used in the calculation of quasi-geostrophic (QG) omega. These analyses were first bilinearly interpolated from their original output grids to a 1.0° × 1.0° latitude/longitude grid at 19 isobaric levels from 1000 to 100 hPa at 50 hPa increments using an interpolation program included in the General Meteorological Package (GEMPAK). The grid-point height and temperature data were then subjected to a Gaussian smoother that eliminates roughly two-thirds of the energy at wavelengths < 660 km, yielding results similar to those achieved using the cowbell filter described by Barnes et al. (1996) for use in QG diagnostics with mesoscale models. Employing the technique of successive over-relaxation (SOR), the *f*-plane version of the ***Q***-vector form of the QG-omega equation (Eq. (9) is solved using a spatially-averaged static stability that varies for each time with f_o set equal to the central latitude of the domain. Though calculations are made for each of the five species of QG-omega presented in Martin (2014)[1], the subsequent analyses focus only on the total QG-omega and conforms to solutions of (9)

$$\sigma\left(\nabla^2 + \frac{{f_o}^2}{\sigma}\frac{\partial^2}{\partial p^2}\right)\omega = -2\nabla\cdot\vec{Q} \tag{9}$$

where $\vec{Q}$ is given by $\vec{Q} = -\frac{R}{p}\left[\left(\frac{\partial\vec{V}_g}{\partial x}\cdot\nabla T\right)\hat{\imath}, \left(\frac{\partial\vec{V}_g}{\partial y}\cdot\nabla T\right)\hat{\jmath}\right]$. The piecewise PV inversion analysis of Chapter 2 isolated a mean PV, upper-tropospheric PV (UPTROP), a diabatically-generated PV (INT), and a near-surface PV which included boundary temperature anomalies (SFC). The sum of UPTROP, INT and SFC represented the FULL perturbation PV and inverting that for the balanced streamfunction and geopotential height fields returns what is referred to as the *perturbation inversion*. Adding the mean PV to the full perturbation PV and inverting that sum will be referred to as the *total inversion*. Inversion of each of these 4 pieces returned associated streamfunction and geopotential height fields, labeled Φ_m (ψ_m), Φ_{uptrop} (ψ_{uptrop}), Φ_{int} (ψ_{int}), and Φ_{sfc} (ψ_{sfc}), respectively. Since the geostrophic wind is defined as

---

[1] These species include ω_n and ω_s, those QG ω fields derived from divergences of the across- and along-isentrope components of ***Q***, respectively. Calculations are also made of ω_{curv} and ω_{shear}, those QG ω fields derived from consideration of curvature and shear vorticity advections by the thermal wind, respectively.

$$\vec{V}_g = -\frac{1}{f_o}(\hat{k} \times \nabla\phi), \tag{10}$$

the geostrophic wind associated with each piece of the PV is returned by substituting the appropriate geopotential height field into (10). Similarly, the perturbation temperature associated with each discrete piece of geopotential can be determined via the hydrostatic relationship

$$\frac{\partial\phi'}{\partial p} = \frac{-RT'}{p},$$

where ϕ' and T' are the ϕ and T associated with each of the four pieces of the total PV distribution defined earlier. The geostrophic wind and temperature anomalies associated with each piece of the total PV can be substituted into various expressions for the components of $\boldsymbol{Q}$ in (9) to calculate $\boldsymbol{Q}$-vectors arising from interactions between the geostrophic wind associated with one piece of the PV and the thermal field associated with any other piece of the PV.

The total QG-omega can thus be partitioned into 16 distinct pieces (schematically illustrated in Fig. 3.1), each of which arises from forcing terms derived from the geostrophic winds and thermal fields associated with discrete portions of the total PV field as defined in the inversion process. A similar partitioning of the total QG-omega was used in Winters et al. (2020) to examine the production of vertical motions in the vicinity of jet superposition events. In subsequent portions of this analysis, the QG-omega associated with forcing derived from the UPTROP winds and the UPTROP thermal anomaly will, as illustrated in Fig. 3.1, be denoted as ω_{uu} where the first subscript refers to the piece of the total PV from which the geostrophic winds in the associated forcing term originate (UPTROP) while the second points to the piece from which the thermal field derives (UPTROP).

ω_{mm}	ω_{mu}	ω_{mi}	ω_{ms}	*MEAN* $\boldsymbol{V_g}$
ω_{um}	ω_{uu}	ω_{ui}	ω_{us}	*UPTROP* $\boldsymbol{V_g}$
ω_{im}	ω_{iu}	ω_{ii}	ω_{is}	*INT* $\boldsymbol{V_g}$
ω_{sm}	ω_{su}	ω_{si}	ω_{ss}	*SFC* $\boldsymbol{V_g}$
MEAN ***T***	*UPTROP* ***T***	*INT* ***T***	*SFC* ***T***	

Fig. 3.1. Matrix illustrating the 16 separate QG-ω calculations resulting from combining each of the 4 wind components from the inversion with each of the 4 thermal components. Convention for each QG-ω species is that the 1st subscript refers to the geostrophic wind that was used and the 2nd subscript to the thermal component used to calculate the given QG-ω.

3.3. Synoptic Description

By 0000 UTC 26 November a weak surface cyclone had emerged along the warm front of a weak stationary cyclone south of the Aleutian Islands (Fig. 3.2a). This new storm bisected a sprawling anticyclone that dominated the eastern north Pacific basin at this time. Upstream over the Bering Sea, a robust cyclone was still developing (not shown) and had a deep warm frontal zone that draped over western Alaska at this time, as evidenced by the notable 300:700 hPa thickness gradient there (Fig. 3.2b). An especially strong region of horizontal thermal contrast characterized a zonally-oriented baroclinic zone stretching eastward from southeast of Kodiak Island, AK to the Queen Charlotte Islands of British Columbia. A modest geostrophic vorticity maxima of ~12 x 10^{-5} s^{-1} was embedded within the associated strong vertical shear denting the 500 hPa ridge crest in the Gulf of Alaska (Fig. 3.2b). The associated 500 hPa geostrophic vorticity maximum was located too far upstream of the nascent surface cyclone to contribute substantially to its development at this time as QG-omega attributable to cyclonic vorticity advection (CVA) by the thermal wind (Sutcliffe 1947) – hereafter referred to as Sutcliffe omega[2] – associated with that feature was maximized well north of the surface cyclone (Fig. 3.2c). However, negative Sutcliffe omega at 700 hPa was located to the east of the cyclone center suggesting that CVA by the thermal wind in the lower troposphere was contributing to the storm’s eastward propagation, consistent with its designation as a diabatic Rossby wave in the analysis of Chapter 2. A vertical cross-section through the Sutcliffe omega maxima at both levels (Fig. 3.2d) emphasizes that, at this time, the Sutcliffe omega was vertically disjointed.

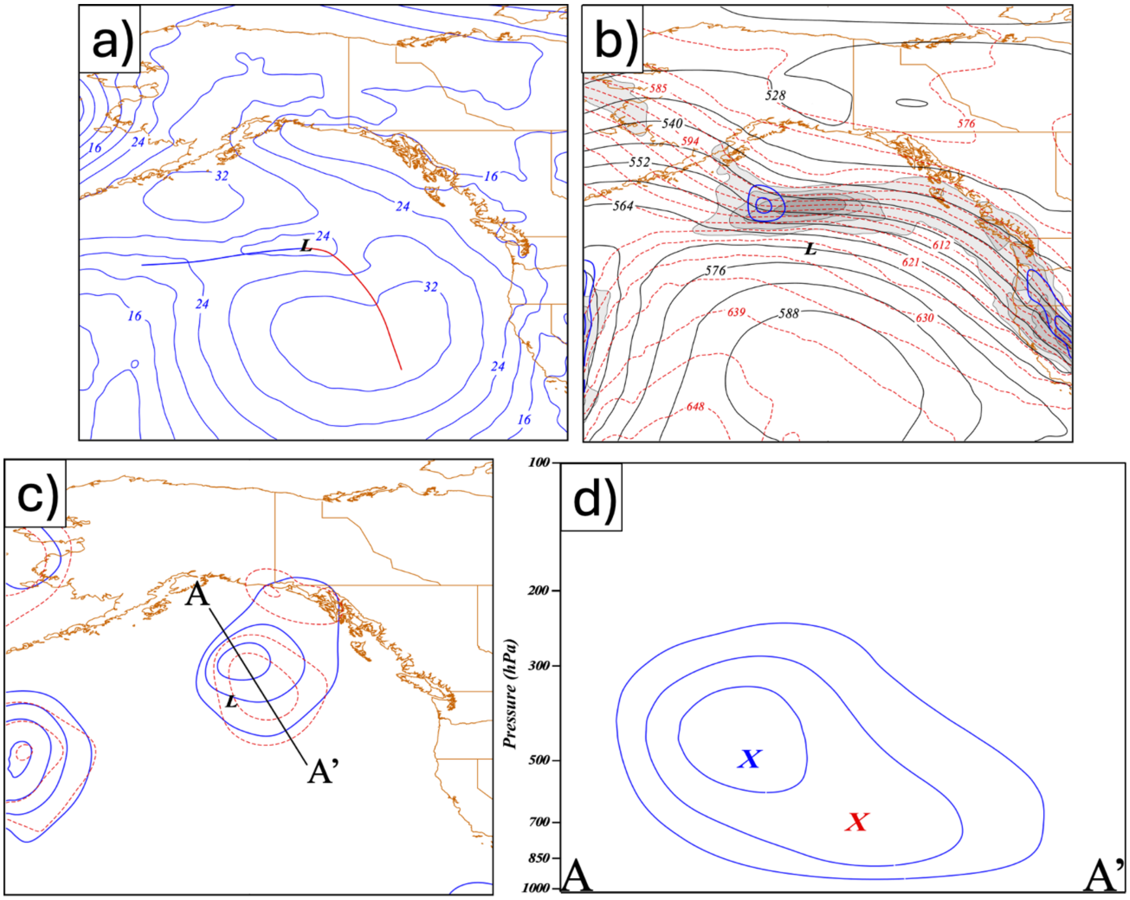

---

[2] “Sutcliffe omega” (ω_{SUT}) refers to solution to the following form of the QG ω equation;

$$\sigma\left(\nabla^2 + \frac{f_o{}^2}{\sigma}\frac{\partial^2}{\partial p^2}\right)\omega_{SUT} = 2[f_o\frac{\partial \vec{V}_g}{\partial p}\cdot\nabla(\zeta_g + f)]$$

Fig. 3.2. (a) Sea level pressure and frontal locations valid at 0000 UTC 26 November 2019. Solid, blue lines are sea level pressure contoured every 4 hPa starting at 1000 hPa. Thick red line indicates surface warm front and thick blue line indicates surface cold front. Position of the sea level pressure minimum associated with the bomb cyclone denoted as a black "L". (b) 500 hPa geopotential heights, 500 hPa geostrophic relative vorticity, 300:700 hPa thickness, and 500 hPa cyclonic vorticity advection (CVA) by the 300:700 hPa thermal wind. Solid, black lines are 500 hPa geopotential heights contoured every 6 dm starting at 540 dm. Dashed, red lines are 300:700 hPa thickness contoured every 4.5 dm starting at 603 dm. Solid, blue lines are 500 hPa geostrophic relative vorticity contoured every 4×10^{-5} s^{-1} starting at 8×10^{-5} s^{-1}. Gray shading is magnitude of the 300:700 hPa thickness gradient shaded every 10×10^{-5} m m^{-1} starting at 40×10^{-5} m m^{-1}. (c) Blue lines are negative 500 hPa QG-omega attributable to CVA by the 300:700 hPa thermal wind ("Sutcliffe omega") contoured every -1 dPa s^{-1}. Red lines are negative 700 hPa Sutcliffe omega contoured every +1 dPa s^{-1}. Black "L" as in (a). (d) Cross section of negative Sutcliffe omega taken along A-A' in (c) contoured every -1 dPa s^{-1}. Red "X" indicates Sutcliffe omega maximum at 700 hPa and blue "X" indicates Sutcliffe omega maximum at 500 hPa.

Six hours later, the surface cyclone had marginally deepened (Fig. 3.3a) as the upper-level short wave encroached from the northwest (Fig. 3.3b). The mid-tropospheric baroclinicity associated with the warm front of the Bering Sea cyclone had modestly intensified by this time with more acute intensification nearer to the shortwave axis upstream of the surface cyclone (Fig. 3.3b). The 500 hPa geostrophic vorticity had assumed a more linear, northwest to southeast orientation by this time (Fig. 3.3b) with a particularly intense, quasi-isotropic feature at its southeastern terminus. This more concentrated upper-tropospheric feature was associated with intensified 500 hPa Sutcliffe omega that was still to the north of the developing cyclone and too far removed to have a substantial impact on surface development at this time (Fig. 3.3c). Instead, the 700 hPa Sutcliffe omega was nearly collocated with the developing surface cyclone (Fig. 3.3c). A vertical cross-section through these two omega minima shows that the vertical disjuncture evident at 0000 UTC still characterized the development environment at this time (Fig. 3.3d).

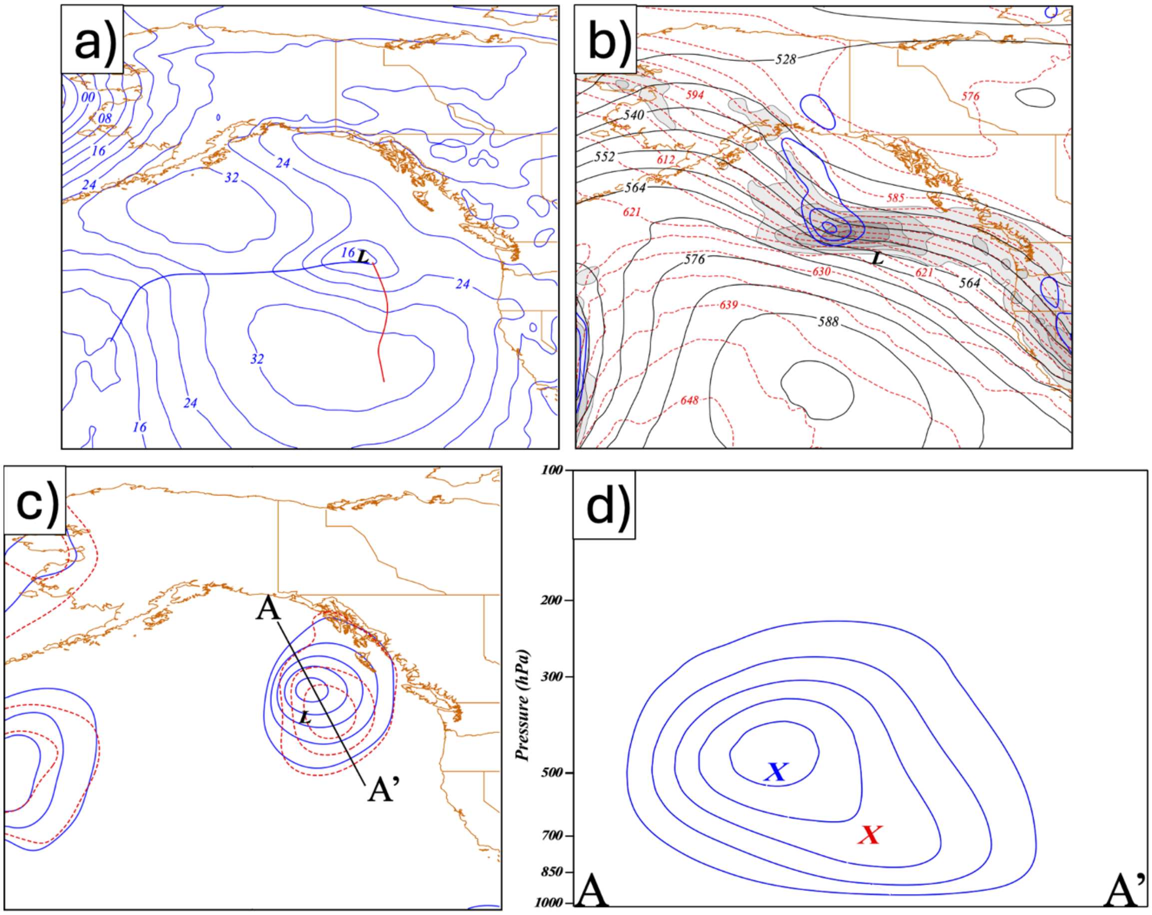

Fig. 3.3. (a) As in Fig. 3.2a but for 0600 UTC 26 November 2019. (b) As in Fig. 3.2b but for 0600 UTC 26 November 2019. (c) As in Fig. 3.2c but for 0600 UTC 26 November 2019. (d) As in Fig. 3.2d but for 0600 UTC 26 November 2019.

In the ensuing six hours rapid surface development began as the sea-level pressure minima of the surface cyclone dropped 12 hPa to 1004 hPa (Fig. 3.4a). Simultaneously, the 500 hPa shortwave developed much stronger geostrophic vorticity at the southeastern end of a now contiguous vortex strip more perfectly positioned to support continued rapid development via CVA by the thermal wind (Fig. 3.4b). This stronger, more linear vortex structure was accompanied by even stronger mid-tropospheric baroclinicity than before, indicating that a potent upper-level jet front system (ULJF) had emerged in the north-northwesterly flow by this time. The combination of stronger baroclinicity coincident with a stronger geostrophic vorticity gradient resulted in stronger 500 hPa Sutcliffe omega now located just about directly over the surface cyclone (Fig. 3.4c). The originally separate Sutcliffe ascent maxima at prior times were now nearly vertically juxtaposed (Fig. 3.4c,d) and much stronger than 12 hours before, resulting in a large, tropospheric-deep column of synoptic-scale ascent and subsequent surface cyclogenesis.

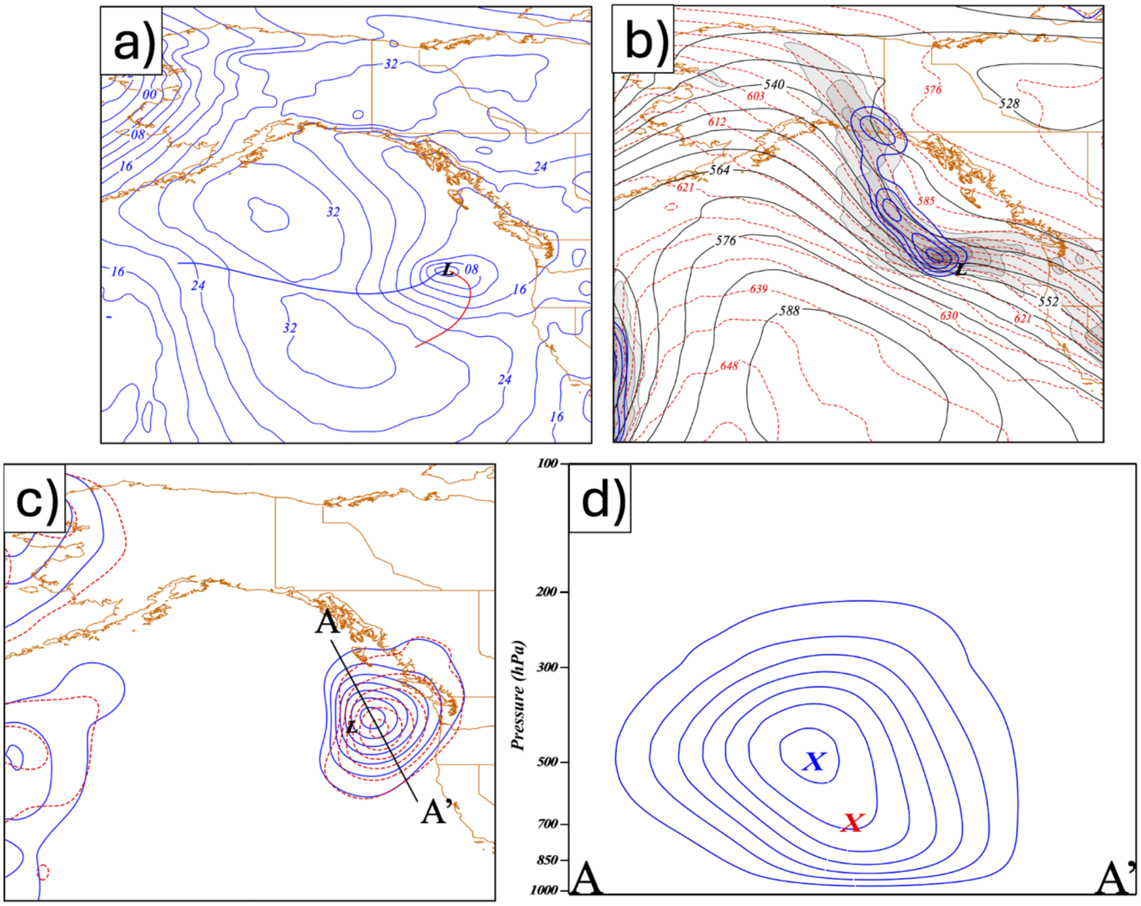

Fig. 3.4. (a) As in Fig. 3.3a but for 1200 UTC 26 November 2019. (b) As in Fig. 3.3b but for 1200 UTC 26 November 2019. (c) As in Fig. 3.3c but for 1200 UTC 26 November 2019. (d) As in Fig. 3.3d but for 1200 UTC 26 November 2019.

In the six hour period ending at 1800 UTC 26 November, the sea-level pressure minimum of the cyclone dropped 20 hPa to 984 hPa (Fig. 3.5a). The storm maintained a favorable orientation relative to the intensifying ULJF, which had developed a bulbous, isotropic nose at its southeastward extremity, that encouraged continued rapid development (Fig. 3.5b). By this time, the mid-tropospheric baroclinicity associated with the ULJF had greatly intensified and the feature now stretched nearly 2000 km across the eastern Gulf of Alaska. The 500 and 700 hPa Sutcliffe ascent maxima were almost perfectly coincident in the vertical at this time and located nearly directly above the SLP minima (Fig. 3.5c). A vertical cross-section through the ascent maxima emphasizes this coincidence and also illustrates the greater intensity of the QG-omega in the face of both the increased thermal wind and the increased vorticity gradient associated with the continued development of the ULJF (Fig. 3.5d).

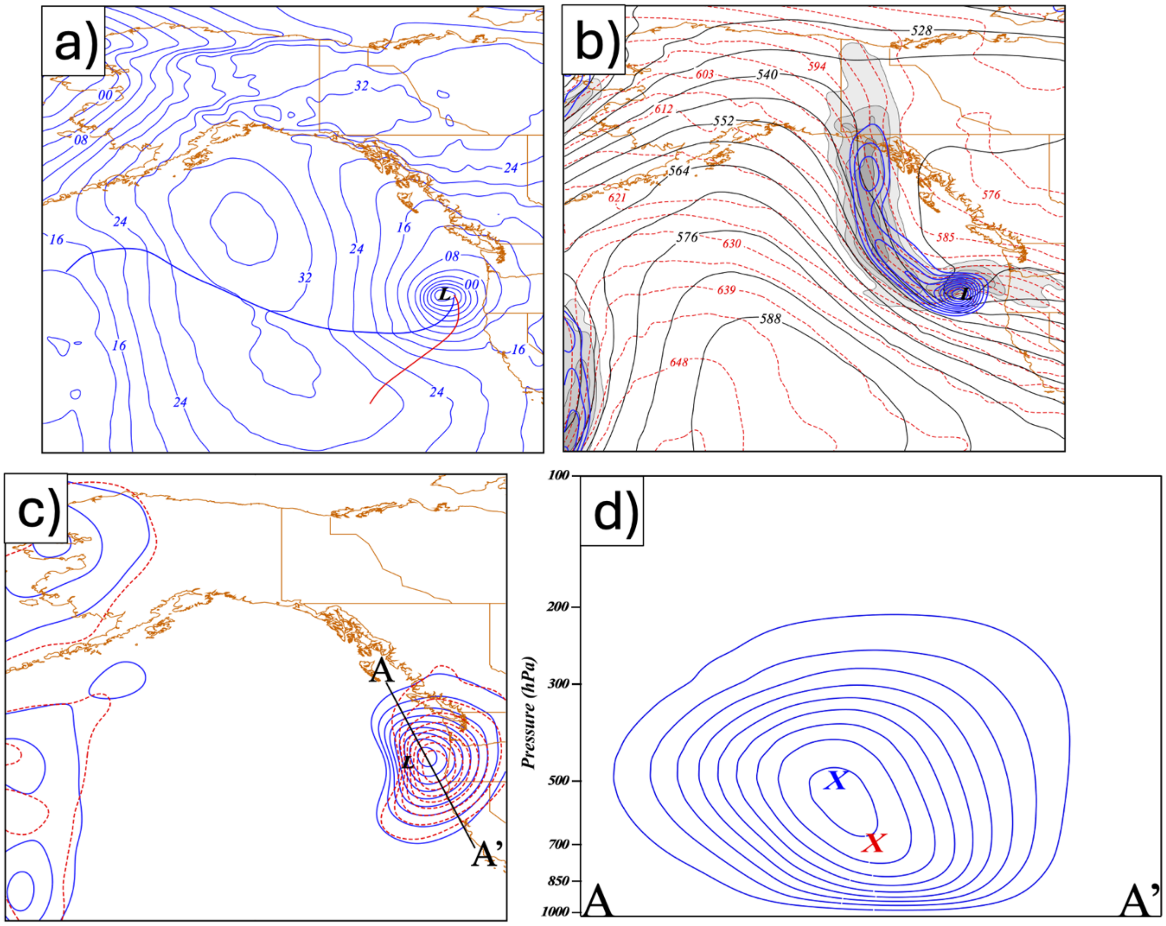

Fig. 3.5. (a) As in Fig. 3.4a but for 1800 UTC 26 November 2019. (b) As in Fig. 3.4b but for 1800 UTC 26 November 2019. (c) As in Fig. 3.4c but for 1800 UTC 26 November 2019. (d) As in Fig. 3.4d but for 1800 UTC 26 November 2019.

An additional 12 hPa of central pressure fall occurred by 0000 UTC 27 November (Fig. 3.6a) by which time the cyclone was just off the coast of the California-Oregon border driving record wave heights and establishing SLP minimum records for the states of California and Oregon (Chapter 2). The storm was located at the base of a tropospheric-deep column of cyclonic geostrophic vorticity, the upper portion of which was contributed by the robust ULJF that had intensified and lengthened in the intervening 6 hours (Fig. 3.6b). Finally, the 500 and 700 hPa Sutcliffe ascent maxima were perfectly coincident and located just east of the surface cyclone center (Fig. 3.6c). A vertical cross-section through the ascent maxima at this time (Fig. 3.6d) emphasizes this cyclogenetic vertical phasing and suggests a vertical migration of the maximum ascent to higher elevation consistent with the greater influence of upper-levels in the development late in the life cycle as suggested by the analysis of Chapter 2.

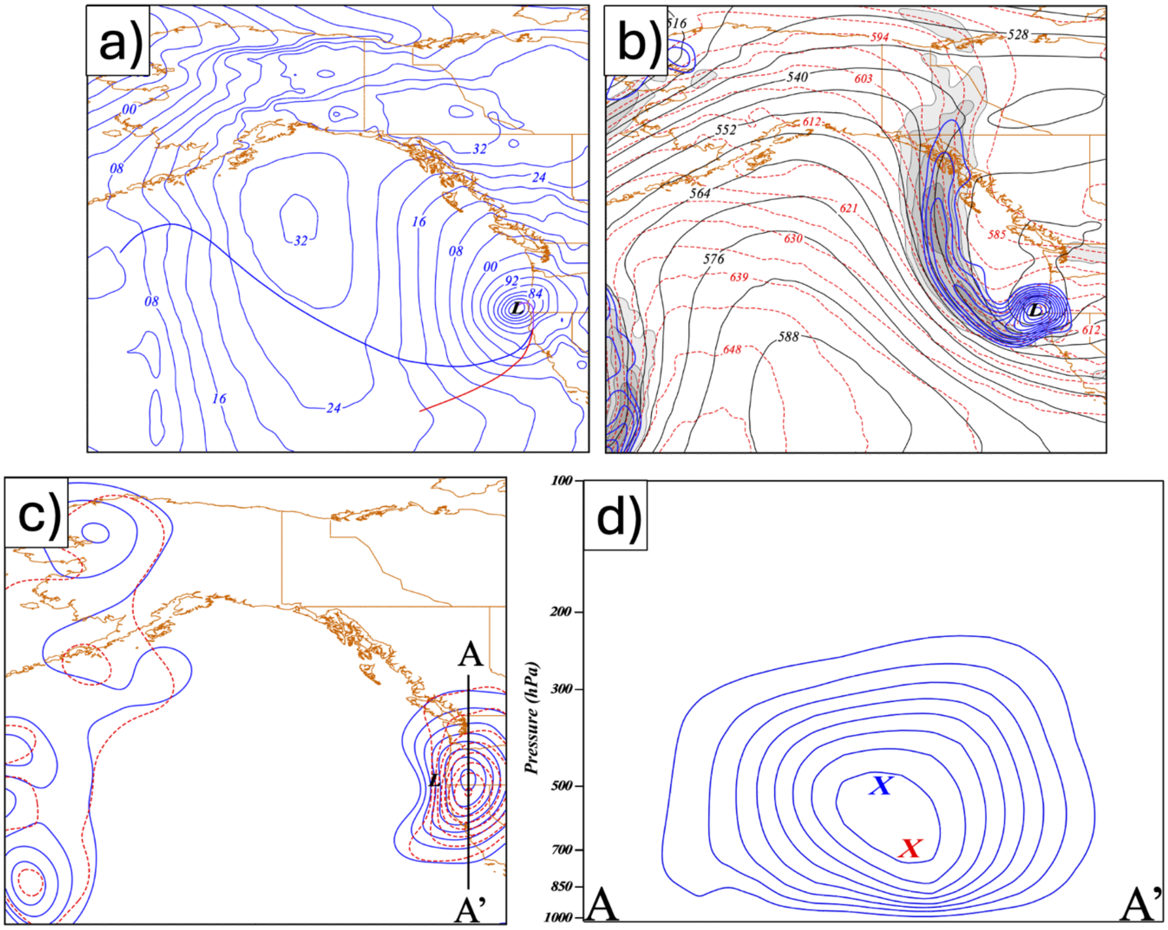

Fig. 3.6. (a) As in Fig. 3.5a but for 0000 UTC 27 November 2019. (b) As in Fig. 3.5b but for 0000 UTC 27 November 2019. (c) As in Fig. 3.5c but for 0000 UTC 27 November 2019. (d) As in Fig. 3.5d but for 0000 UTC 27 November 2019.

3.4. Analysis

An ULJF, like all other frontal structures, must be characterized by a local maxima in horizontal baroclinicity, a local maxima in cyclonic geostrophic vorticity, and high static stability. Given that fronts are quasi-linear features, in order to qualify as a frontal feature, the associated geostrophic vorticity maxima should also be notably anisotropic as well. ULJFs are important elements of a cyclogenetic environment as a consequence of their being characterized by large vorticity and large thermal contrast, a combination capable of providing robust forcing for vertical motion in the form of CVA by the thermal wind (Sutcliffe 1947; Martin 2006). As an individual ULJF progresses through its lifecycle, the vorticity and thermal structures evolve sometimes dramatically via vertical tilting. Tilting of originally horizontally-oriented isentropes into a more vertical orientation is known as tilting frontogenesis and can be quantified by

$$\mathcal{F}_{tilt} = \frac{\partial w}{\partial n}\frac{\partial \theta}{\partial p}$$

where $\hat{n}$ is the natural coordinate direction pointing into the cold air (i.e. $\hat{n} = -\frac{\nabla\theta}{|\nabla\theta|}$). Tilting can also impact the geostrophic vertical vorticity via

$$GeoVort_{tilt} = \hat{k} \cdot \left(\frac{\partial \vec{V}_g}{\partial p} \times \nabla\omega\right), \tag{11}$$

where ω is the vertical motion, $\frac{dp}{dt}$. And, since $\frac{\partial \vec{V}_g}{\partial p} = -\gamma\left(\hat{k} \times \nabla\theta\right)$, the prior expression can be written as

$$GeoVort_{tilt} = \gamma\left(\frac{\partial\theta}{\partial x}\frac{\partial\omega}{\partial x} + \frac{\partial\theta}{\partial y}\frac{\partial\omega}{\partial y}\right) = \gamma(\nabla\theta \cdot \nabla\omega) \tag{12}$$

where $\gamma = \frac{R}{fp_o}\left(\frac{p_o}{p}\right)^{c_v/c_p}$ as in Eliassen (1962). To the extent that ω can be partitioned, so too can the tilting frontogenesis (11) as well as the geostrophic vorticity production via tilting (12).

Fig. 3.7 shows 500 hPa geostrophic vorticity along with 300:700 hPa thickness at 5 different times during the evolution of the NV19 storm. It is clear, especially at the last four of these times (Fig. 3.7b,c,d, and e), that the geostrophic vorticity maxima was unambiguously linear and at least partly coincident with the local maxima in thermal contrast. To be proven shortly, the coincident vorticity and thermal gradient maxima were also regions of high static stability at these four times. Thus, the subsequent analysis will examine aspects of the structure and dynamics of the ULJF at 0600, 1200, and 1800 UTC 26 November as well as at 0000 UTC 27 November 2019.

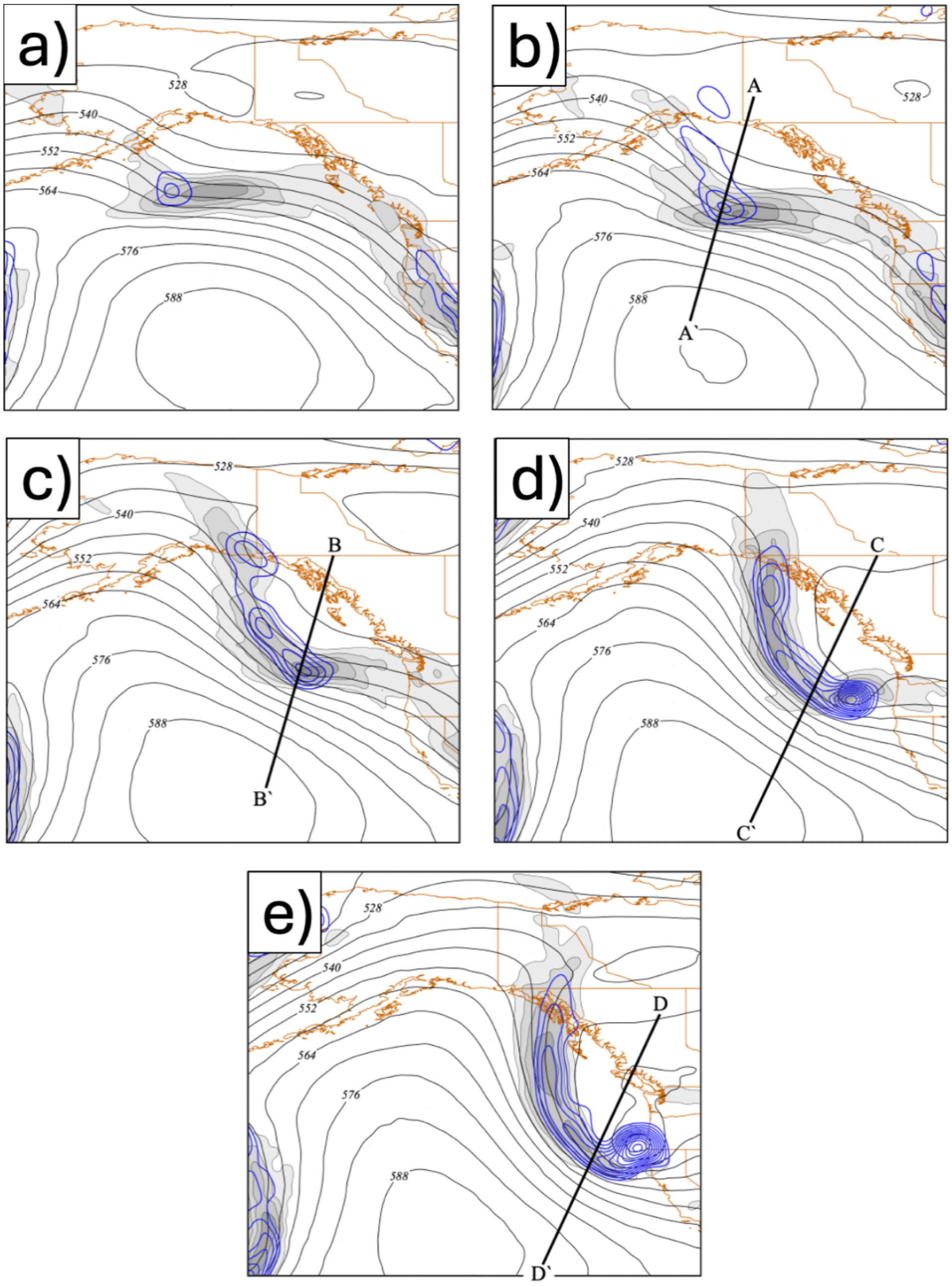

Fig. 3.7. Evolution of the 500 hPa geostrophic relative vorticity and the 300:700 hPa thickness fields during the evolution of the November 2019 northeast Pacific bomb cyclone. Solid, blue lines are 500 hPa geostrophic relative vorticity contoured every 4×10^{-5} s^{-1} starting at 8×10^{-5} s^{-1}. Solid, black lines are 300:700 hPa thickness in dm contoured every 6 dm starting at 540 dm. Gray shading is the magnitude of the 300:700 hPa thickness gradient contoured every 10×10^{-5} m m^{-1} starting at 40×10^{-5} m m^{-1}. Position of the sea level pressure minimum associated with the bomb cyclone denoted as a black "L". (a) 500 hPa geostrophic relative vorticity and magnitude of the 300:700 hPa thickness gradient fields valid at 0000 UTC 26 November 2019. (b) As in (a) but valid for 0600 UTC 26 November 2019. (c) As in (b) but valid for 1200 UTC 26 November 2019. (d) As in (c) but valid for 1800 UTC 26 November 2019. (e) As in (d) but valid for 0000 UTC 27 November 2019.

3.4.1. 0600 UTC 26 November 2019

The ULJF was just beginning to emerge in the northwesterly flow over the central Gulf of Alaska at this time. A vertical cross-section along A-A’ (in Fig. 3.7b) indicated a robust baroclinic zone emerging from the upper-troposphere coincident with a fold in the dynamic tropopause (1.5 PVU isertel) at this time (Fig. 3.8a). Also shown in Fig. 3.8a is the QG-ω from the total inversion. The associated tilting frontogenesis (Fig. 3.8b) was only modestly frontogenetical at this time. The same vertical motion distribution also contributed to a tendency for geostrophic vorticity increase via tilting in exactly the same location (Fig. 3.8c). Since both the horizontal baroclinicity and the geostrophic relative vorticity were increasing via tilting, it follows that the cyclogenetic potency of the ULJF was also increasing at this time.

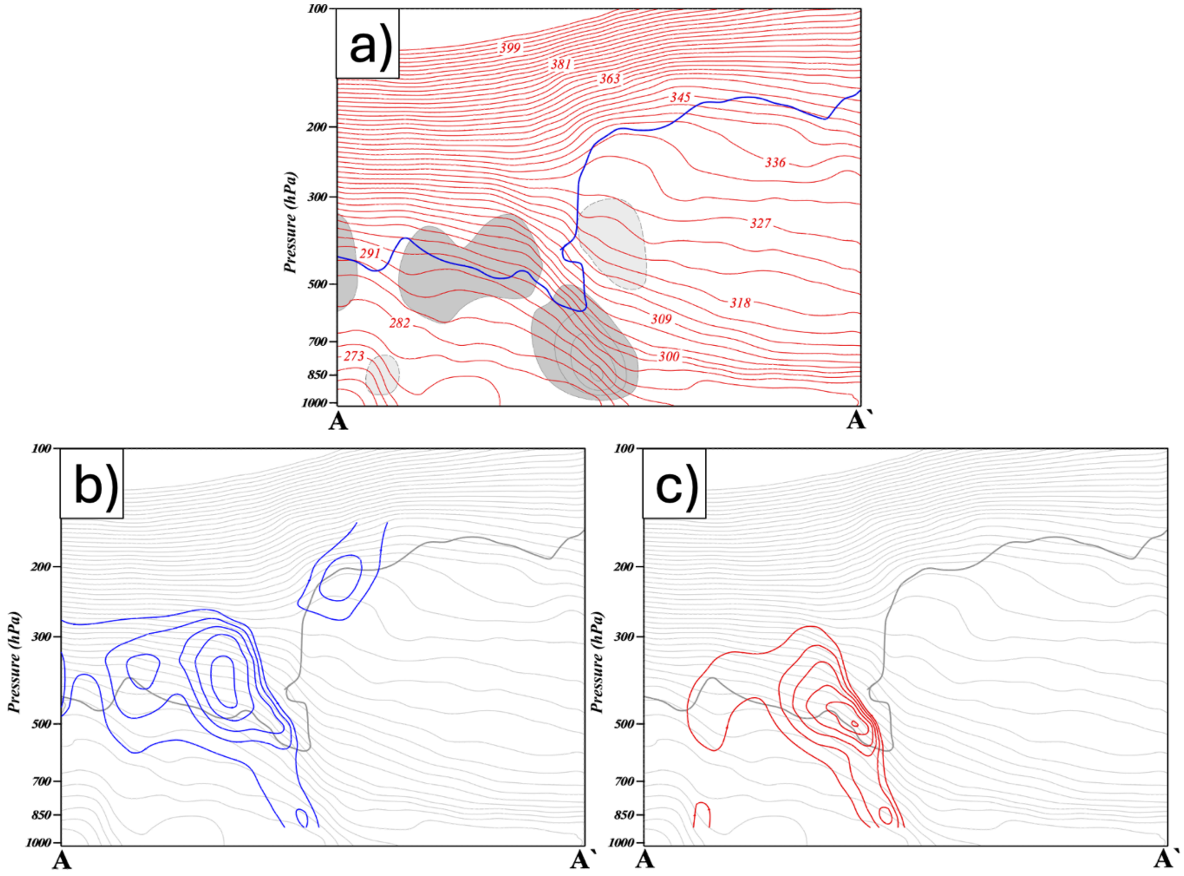

Fig. 3.8. Cross section taken along A-A' in Fig. 3.7b of the upper-level jet front system at 0600 UTC 26 November 2019. (a) Solid, red lines are isentropes in K plotted every 3 K starting at 300 K. Gray colorfill represents the total ω from the piecewise PV inversion with dark, solid gray indicating positive ω contoured every 1 dPa s^{-1} and light, dashed gray indicating negative ω contoured every -1 dPa s^{-1}. Dynamic tropopause, denoted by the 1.5 PV isertel, contoured in blue. (b) Tilting frontogenesis associated with the total ω as in (a) contoured in solid blue every 2.5 x 10^{-10} K m^{-1} s^{-1} starting at 2.5 x 10^{-10} K m^{-1} s^{-1}. Thin gray lines are isentropes as in (a). Thick gray line is the dynamic tropopause as in (a). (c) Geostrophic vorticity tendency via tilting associated with the total ω as in (a) contoured in solid red every 2.5 x 10^{-10} K m^{-1} s^{-1} starting at 2.5 x 10^{-10} K m^{-1} s^{-1}. Thin gray lines as in (b). Thick gray line as in (b).

The total tilting frontogenesis (Fig. 3.8b) can be further partitioned into contributions associated with the geostrophic flow and thermal perturbations attributable to the discrete PV anomalies considered in the piecewise PV inversion. Individual contributions to the tilting frontogenesis are made by 16 types of the QG-ω, each resulting from the interaction of one category of geostrophic winds with one of the four categories of thermal distributions that constitute the piecewise PV inversion results (see Fig. 3.1 and accompanying text). Careful analysis of the distribution of each tilting contribution in both the horizontal and in the vertical along selected vertical cross-sections (to be shown presently) underlies the selection of the results presented here. Though some minor details differ among the four object times, a first-order dynamical similarity underlies the forcing for tilting frontogenesis throughout the life cycle of this ULJF. Each of the QG-ω terms not mentioned in the following subsections were either small in magnitude or counteracted the positive contributions to both tilting frontogenesis and vorticity generation via tilting from the different QG-ω terms considered below.

It is apparent that the largest such contribution at 0600 UTC 26 November was made by the QG-omega forced by the combination of the UPTROP winds acting on the mean and UPTROP perturbation temperature fields (i.e., the sum of ω_{um} and ω_{uu}) (Fig. 3.9a). The mean winds acting on the mean temperature field (i.e. ω_{mm}) also contributed to the total tilting frontogenesis (Fig. 3.9b). A slightly larger contribution was made by the QG-omega arising from the interaction of the INT winds with the mean thermal field (Fig. 3.9c). Not surprisingly, a similar partition of forcing characterizes the generation of geostrophic vorticity via tilting as shown in Fig. 3.10. The largest contribution to the total tilting vorticity tendency (shown in Fig. 3.8c) was provided by the UPTROP winds acting on the mean and UPTROP thermal fields (Fig. 3.10a) followed by the contribution made by ω_{mm} (Fig. 3.10b). The smallest contribution was made by the QG-omega arising from the interaction of INT winds and the mean thermal field (Fig. 3.10c).

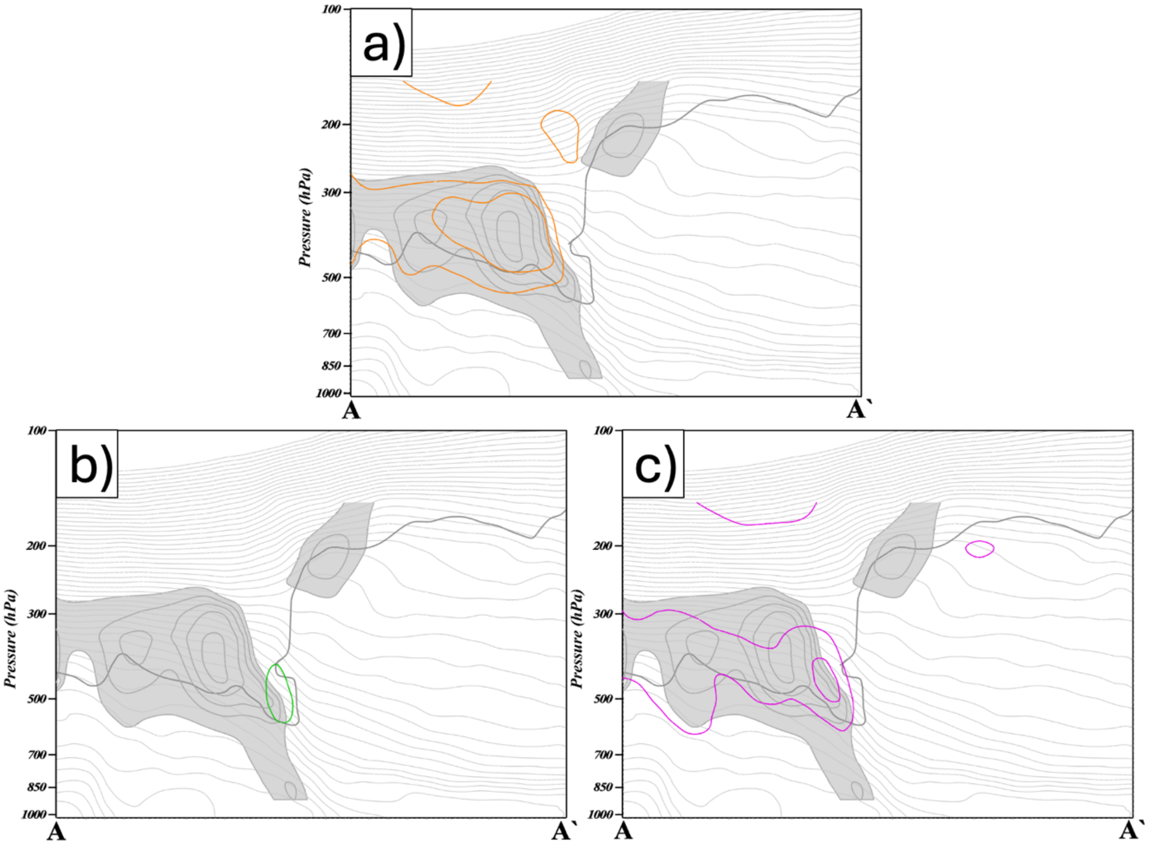

Fig. 3.9. (a) Tilting frontogenesis accomplished by ω_{um} and ω_{uu} valid at 0600 UTC 26 November 2019 contoured in solid orange every 2.5 x 10^{-10} K m^{-1} s^{-1} starting at 2.5 x 10^{-10} K m^{-1} s^{-1}. Light gray shading is tilting frontogenesis from the total ω as in Fig. 3.8b. Thin gray lines are isentropes as in Fig. 3.8a. (b) Tilting frontogenesis accomplished by ω_{mm} valid at 0600 UTC 26 November 2019 contoured in solid green every 2.5 x 10^{-10} K m^{-1} s^{-1} starting at 2.5 x 10^{-10} K m^{-1} s^{-1}. Light gray shading as in (a). Thin gray lines as in (a). (c) Tilting frontogenesis accomplished by ω_{im} valid at 0600 UTC 26 November 2019 contoured in solid pink every 2.5 x 10^{-10} K m^{-1} s^{-1} starting at 2.5 x 10^{-10} K m^{-1} s^{-1}. Light gray shading as in (b). Thin gray lines as in (b).

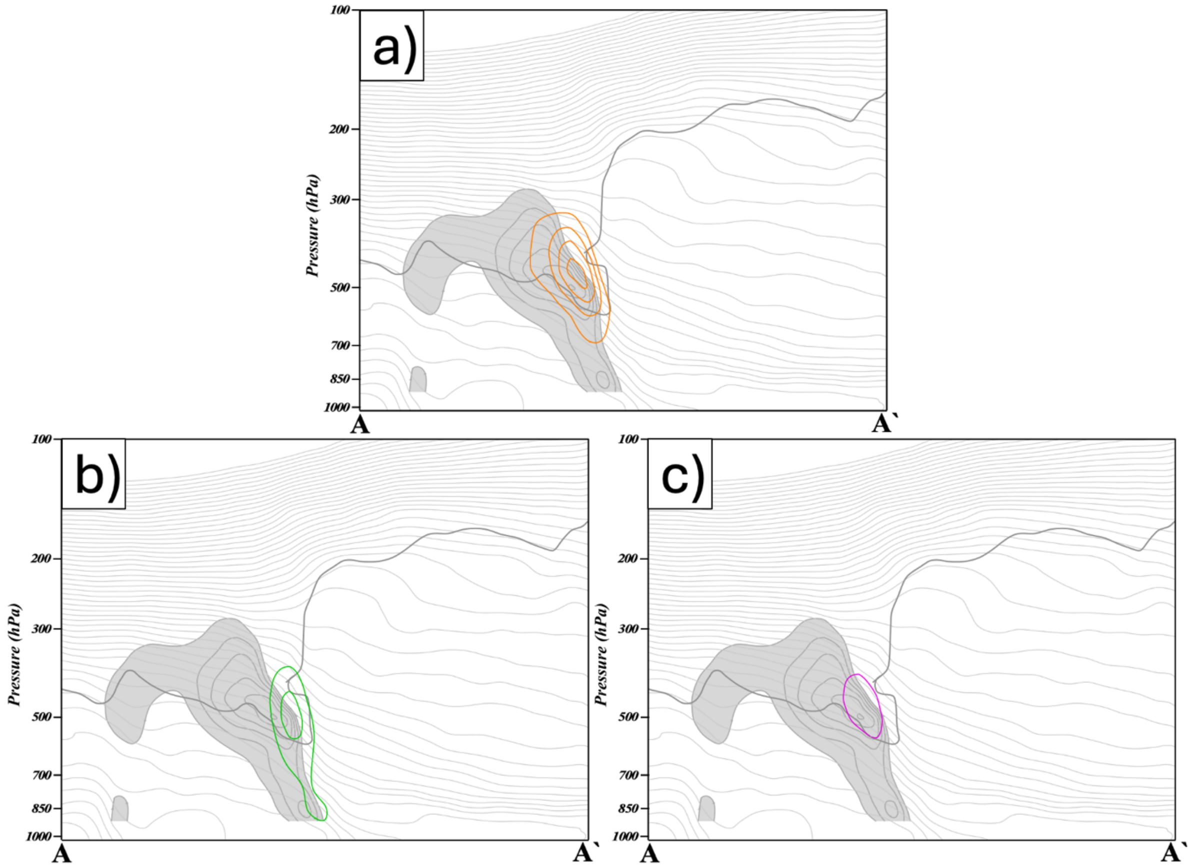

Fig. 3.10. (a) Geostrophic vorticity tendency via tilting accomplished by ω_{um} and ω_{uu} valid at 0600 UTC 26 November 2019 contoured in solid orange every 2.5 x 10^{-10} K m^{-1} s^{-1} starting at 2.5 x 10^{-10} K m^{-1} s^{-1}. Light gray shading is geostrophic vorticity tendency via tilting from the total ω as in Fig. 3.8c. Thin gray lines are isentropes as in Fig. 3.8a. (b) Geostrophic vorticity tendency via tilting accomplished by ω_{mm} valid at 0600 UTC 26 November 2019 contoured in solid green every 2.5 x 10^{-10} K m^{-1} s^{-1} starting at 2.5 x 10^{-10} K m^{-1} s^{-1}. Light gray shading as in (a). Thin gray lines as in (a). (c) Geostrophic vorticity tendency via tilting accomplished by ω_{im} valid at 0600 UTC 26 November 2019 contoured in solid pink every 2.5 x 10^{-10} K m^{-1} s^{-1} starting at 2.5 x 10^{-10} K m^{-1} s^{-1}. Light gray shading as in (b). Thin gray lines as in (b).

3.4.2. 1200 UTC 26 November 2019

The ULJF had undergone considerable development by 1200 UTC 26 November as both the horizontal temperature contrast and depth of the associated tropopause fold were more robust at this time (Fig. 3.11a). The total QG vertical motions were characterized by strong subsidence below 500 hPa straddled by weak ascent at higher elevations (Fig. 3.11a). This distribution produced stronger tilting frontogenesis at this time than at the previous six hours (Fig. 3.11b). Similarly stronger geostrophic vorticity tendency via tilting also occurred at this time (Fig. 3.11c). So, as had been the case six hours earlier, the ULJF continued to intensify as did its cyclogenetic potency at this time.

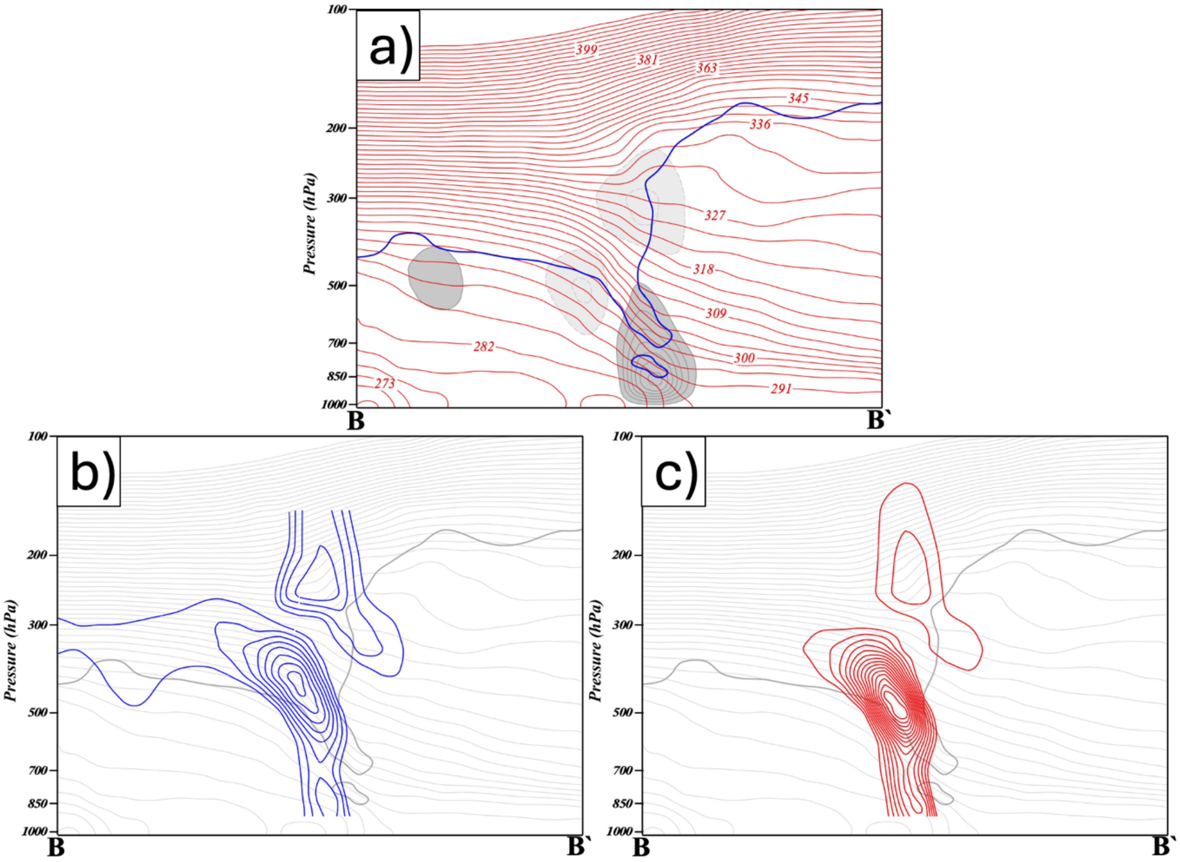

Fig. 3.11. Cross section taken along B-B' in Fig. 3.7c of the upper-level jet front system at 1200 UTC 26 November 2019. (a) As in Fig. 3.8a but for 1200 UTC 26 November 2019. (b) As in Fig. 3.8b but for 1200 UTC 26 November 2019. (c) As in Fig. 3.8c but for 1200 UTC 26 November 2019.

Partitioning the total tilting frontogenesis into its most substantial component contributions once again reveals that the largest tilting frontogenesis was contributed by the sum of ω_{uu}, and ω_{um} (Fig. 3.12a). At this time, the next most substantial contribution was made by the areas of QG-omega arising from the mean and INT winds acting on the mean temperature (ω_{mm} and ω_{im}) (Fig. 3.12b). A small contribution was also made by a residual collection of terms (ω_{mu}, ω_{ms}, ω_{us}, and ω_{iu}) (Fig. 3.12c).

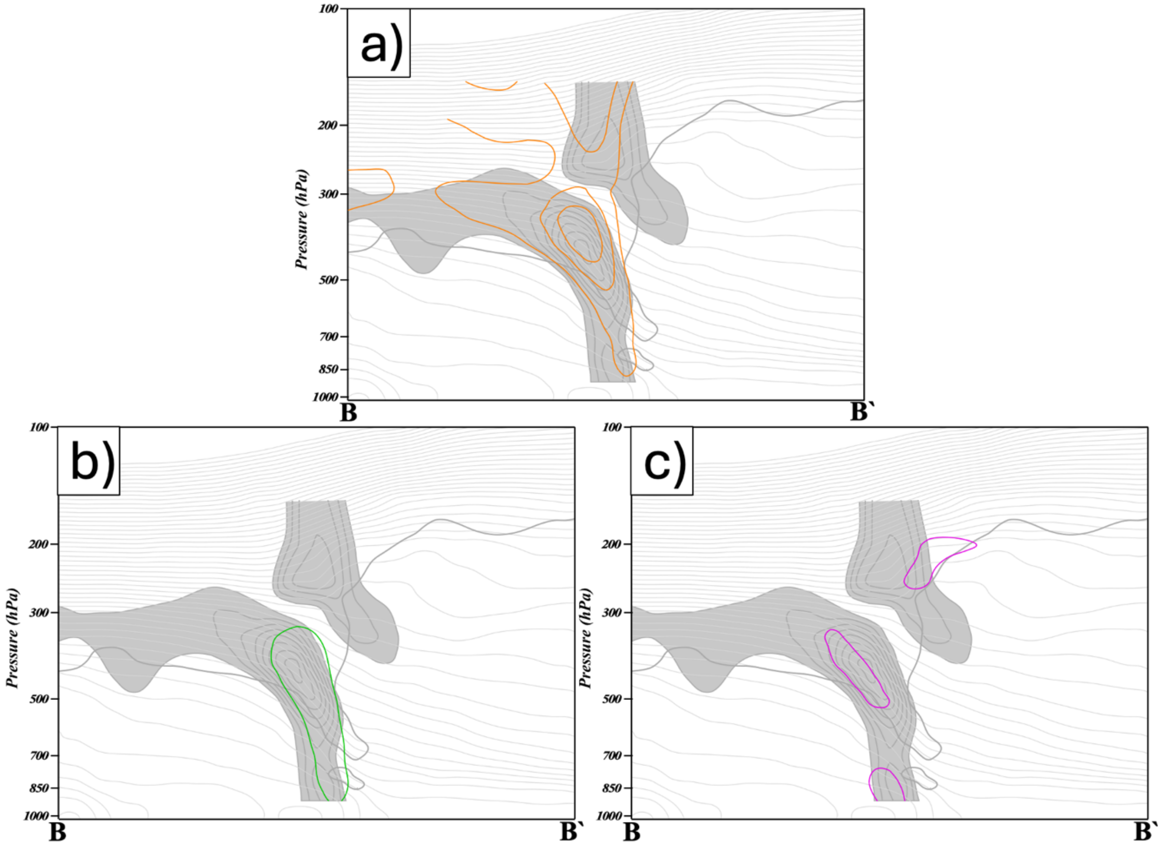

Fig. 3.12. (a) Tilting frontogenesis accomplished by ω_{um} and ω_{uu} valid at 1200 UTC 26 November 2019. Contours and shading as in Fig. 3.9a. (b) Tilting frontogenesis accomplished by ω_{mm} and ω_{im} valid at 1200 UTC 26 November 2019. Contours and shading as in Fig. 3.9b. (c) Tilting frontogenesis accomplished by the sum of ω_{mu}, ω_{ms}, ω_{us}, and ω_{iu} valid at 1200 UTC 26 November 2019. Contours and shading as in Fig. 3.9c.

As had been the case six hours earlier, the largest contribution to the total geostrophic vorticity tendency via tilting was provided by the QG-omega arising from the interaction of the UPTROP winds with the mean and UPTROP thermal fields (Fig. 3.13a) with a smaller contribution from the sum of ω_{mm} and ω_{im} (Fig. 3.13b). Only a very weak contribution was made by QG-omega attributable to the collection of residual terms (ω_{mu}, ω_{ms}, ω_{us}, and ω_{iu}) (Fig. 3.13c).

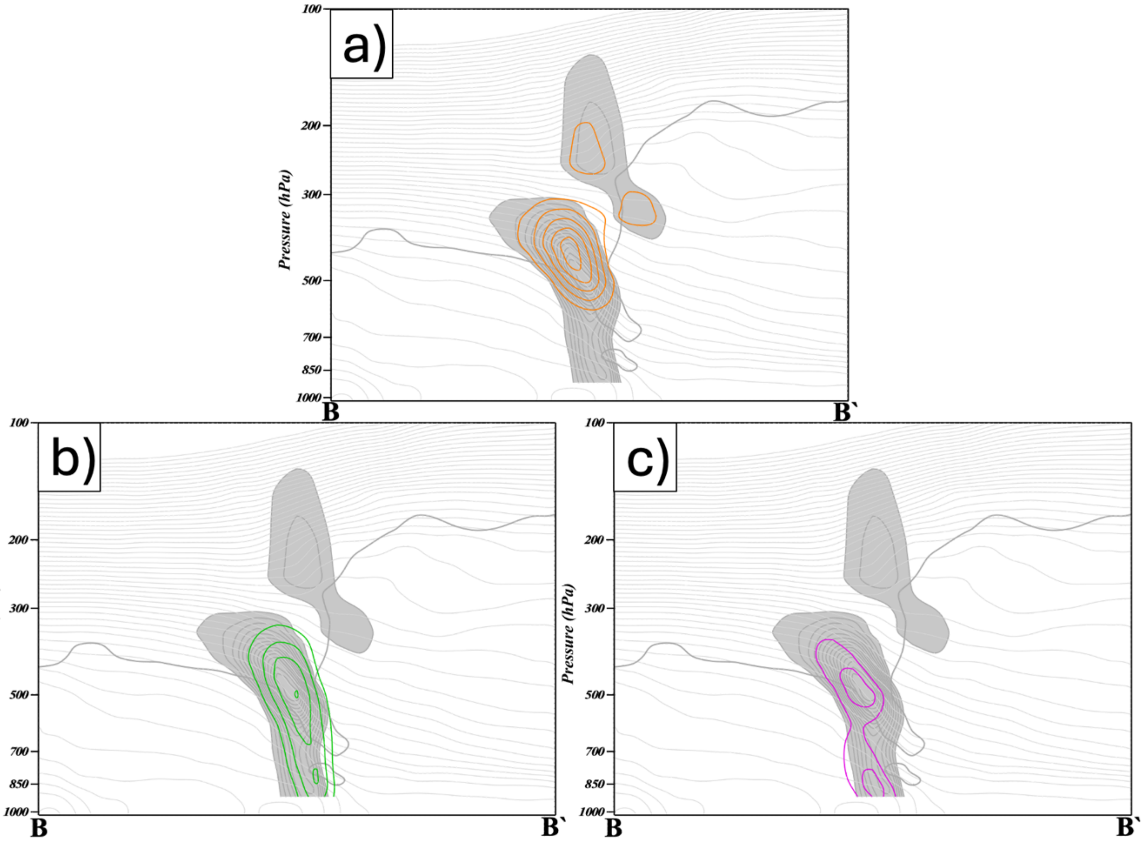

Fig. 3.13. (a) Geostrophic vorticity tendency via tilting accomplished by ω_{um} and ω_{uu} valid at 1200 UTC 26 November 2019. Contours and shading as in Fig. 3.10a. (b) Geostrophic vorticity tendency via tilting accomplished by ω_{mm} and ω_{im} valid at 1200 UTC 26 November 2019. Contours and shading as in Fig. 3.10b. (c) Geostrophic vorticity tendency via tilting accomplished by the sum of ω_{mu}, ω_{ms}, ω_{us}, and ω_{iu} valid at 1200 UTC 26 November 2019. Contours and shading as in Fig. 3.10c.

3.4.3. 1800 UTC 26 November 2019

The ULJF continued to strengthen through this time with a strong horizontal temperature contrast penetrating to lower-levels of the troposphere (Fig. 3.14a) under the influence of a much more robust total QG-omega subsidence maximum (Fig. 3.14b). This descent forced stronger, more coherent tilting frontogenesis that extended downward to around 600 hPa at this time (Fig. 3.14b). Nearly coincident geostrophic vorticity tendency via tilting continued to encourage intensification of the upper-tropospheric geostrophic vorticity maxima at this time (Fig. 3.14c).

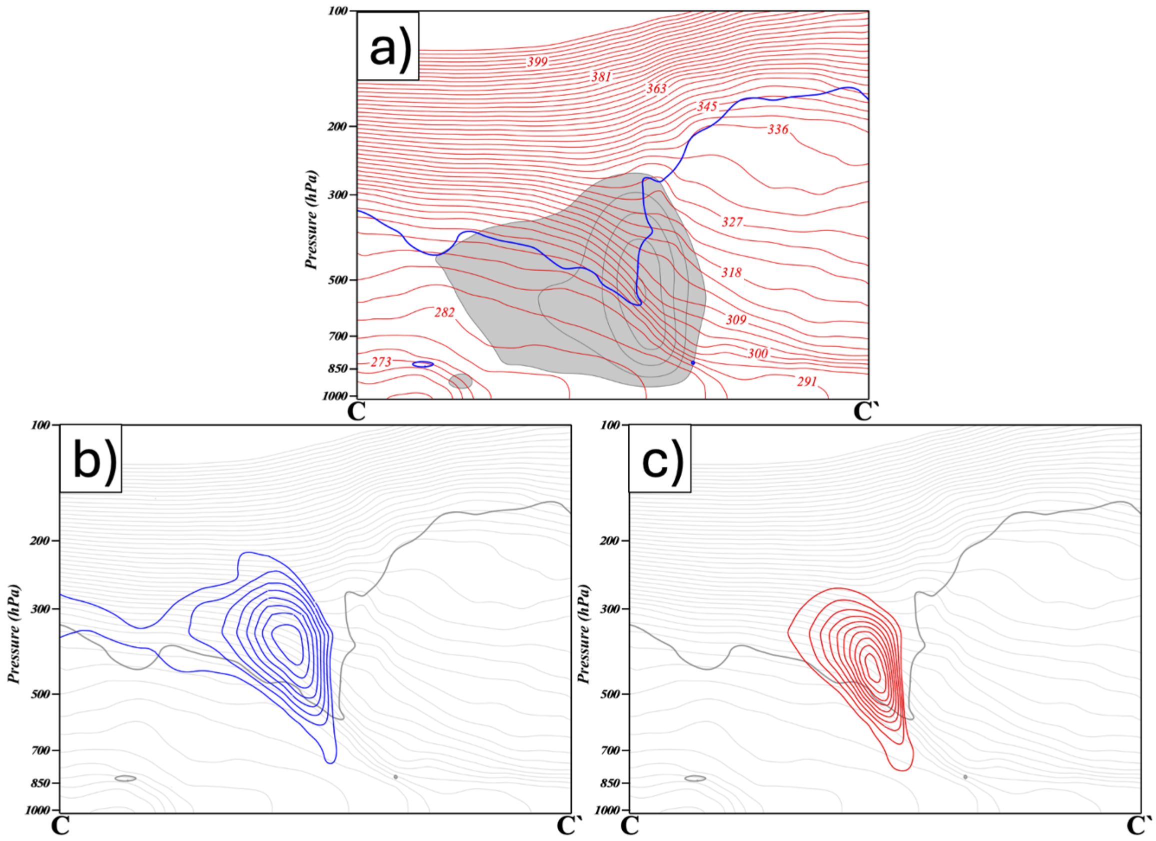

Fig. 3.14. Cross section taken along C-C' in Fig. 3.7d of the upper-level jet front system at 1800 UTC 26 November 2019. (a) As in Fig. 3.11a but for 1800 UTC 26 November 2019. (b) As in Fig. 3.11b but for 1800 UTC 26 November 2019. (c) As in Fig. 3.11c but for 1800 UTC 26 November 2019.

The partitioned tilting frontogenesis was different at this time than at the prior times. An even more overwhelming contribution to the total now came from the sum of ω_{uu} and ω_{um} (Fig. 3.15a). Much weaker contributions were made by the combination of ω_{mm} and ω_{im} (Fig. 3.15b) and the residual from the sum of ω_{mu} , ω_{ms} and ω_{us} (Fig. 3.15c). At this more well-developed stage of the ULJF lifecycle, a similar rearrangement in the contributions to vorticity production via tilting was evident at this time, with the overwhelming contribution coming from the sum of ω_{uu} and ω_{um} (Fig. 3.16a). Less than half as large was the contribution from the sum of ω_{mm} and ω_{im} (Fig. 3.16b). The residual terms (ω_{mu}, ω_{ms} and ω_{us}) made only a very modest contribution that extended into the lower troposphere (Fig. 3.16c).

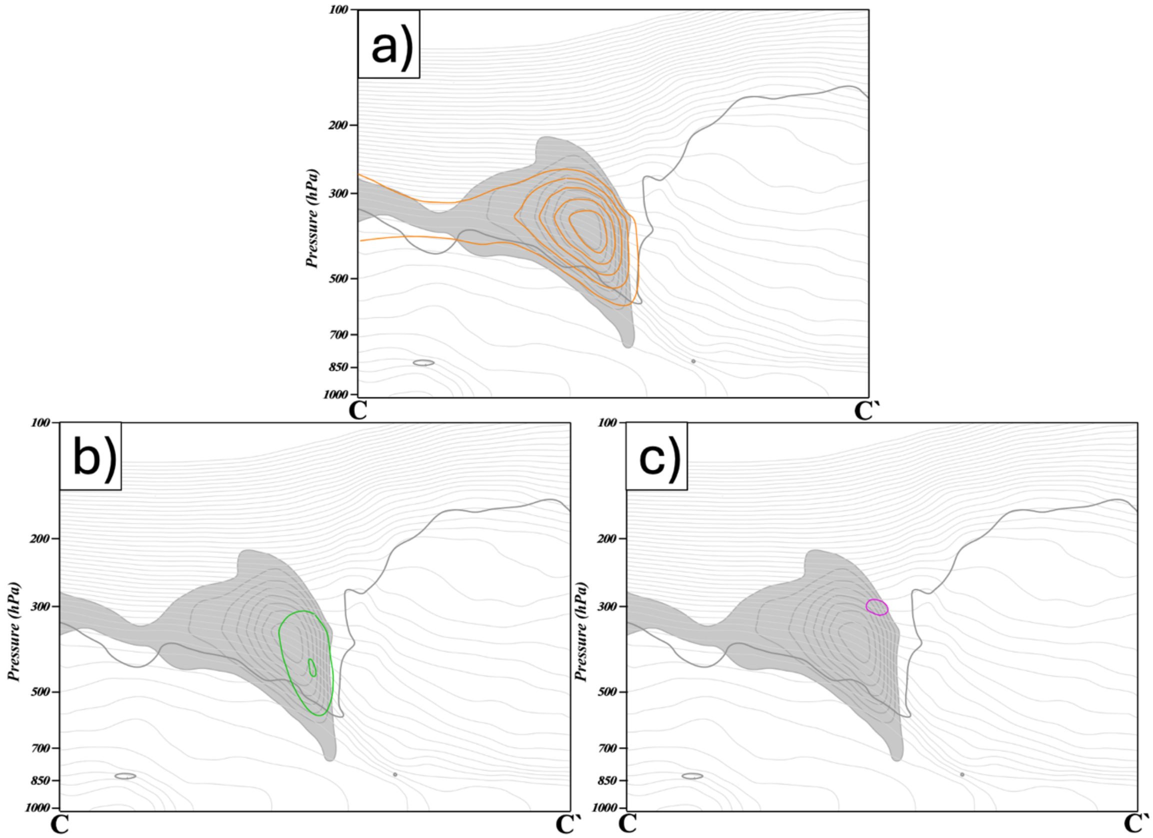

Fig. 3.15. (a) Tilting frontogenesis accomplished by ω_{um} and ω_{uu} valid at 1800 UTC 26 November 2019. Contours and shading as in Fig. 3.12a. (b) Tilting frontogenesis accomplished by ω_{mm} and ω_{im} valid at 1800 UTC 26 November 2019. Contours and shading as in Fig. 3.12b. (c) Tilting frontogenesis accomplished by the sum of ω_{mu}, ω_{ms}, and ω_{us} valid at 1800 UTC 26 November 2019. Contours and shading as in Fig. 3.12c.

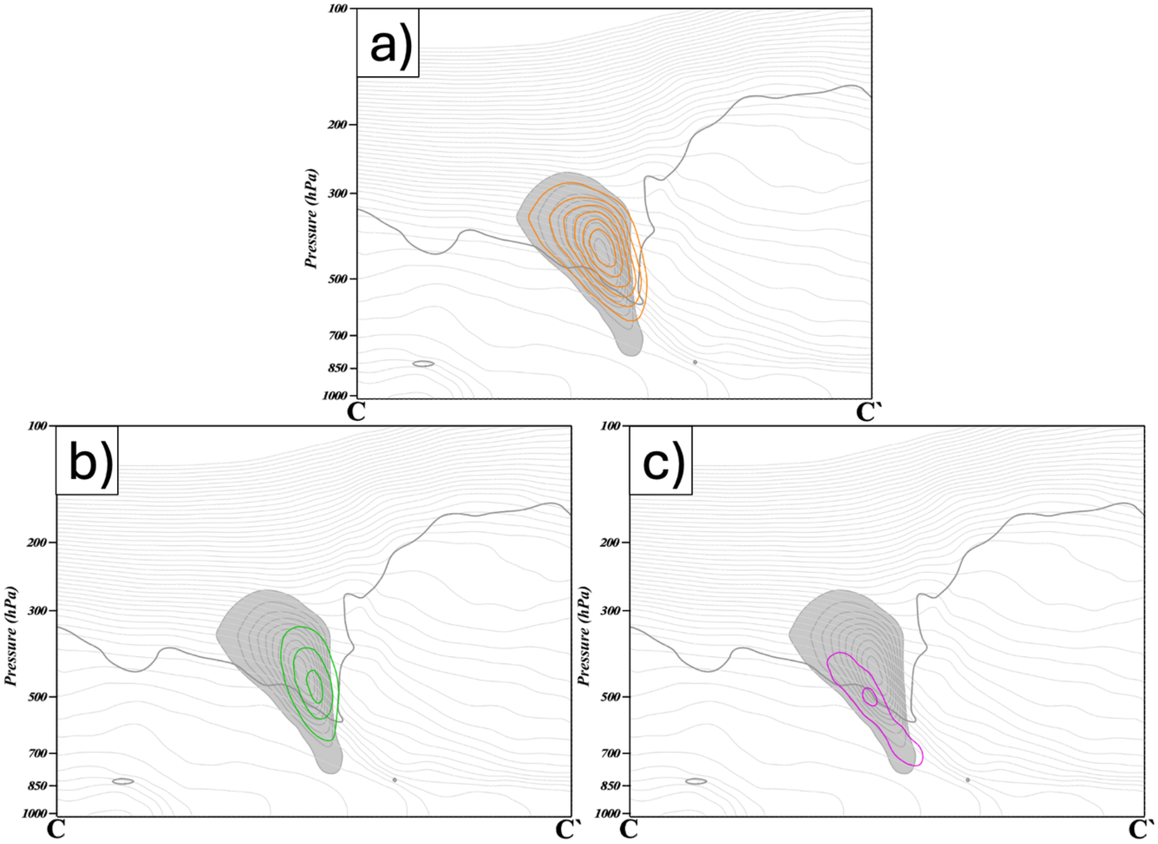

Fig. 3.16. (a) Geostrophic vorticity tendency via tilting accomplished by ω_{um} and ω_{uu} valid at 1800 UTC 26 November 2019. Contours and shading as in Fig. 3.13a. (b) Geostrophic vorticity tendency via tilting accomplished by ω_{mm} and ω_{im} valid at 1800 UTC 26 November 2019. Contours and shading as in Fig. 3.13b. (c) Geostrophic vorticity tendency via tilting accomplished by the sum of ω_{mu}, ω_{ms}, and ω_{us} valid at 1800 UTC 26 November 2019. Contours and shading as in Fig. 3.13c.

3.4.4. 0000 UTC 27 November 2019

By 0000 UTC 27 November, the ULJF had reached its maximum length and maximum intensity (see Fig. 3.6b and Fig. 3.7e) as the surface cyclone neared its maximum intensity. The thermal structure of the ULJF at this time was nearly indistinguishable from that which characterized it six hours earlier, though the dynamic tropopause had descended downward to around 600 hPa by this time as evidenced by the PV pendant associated with the ULJF (Fig. 3.17a). The QG descent maxima had shifted decidedly toward the cold side of the front resulting in an abrupt recission of a slightly weaker tilting frontogenesis maxima to around 350 hPa by this time (Fig. 3.17b). The tilting of geostrophic vertical shear into vertical vorticity had also weakened and retreated to higher elevation by this time (Fig. 3.17c). Thus, by 0000 UTC 27 November, the intensification of the ULJF via tilting had effectively ended.

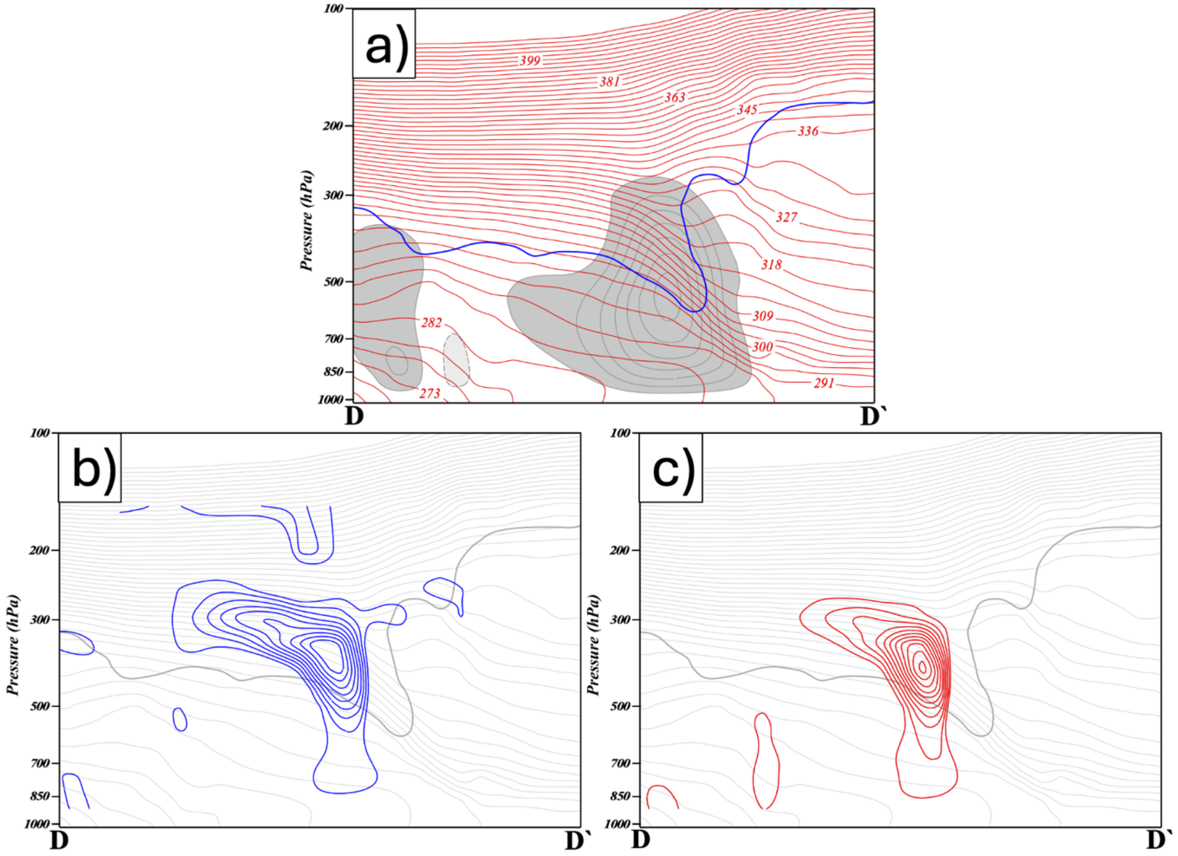

Fig. 3.17. Cross section taken along D-D’ in Fig. 3.7e of the upper-level jet front system at 0000 UTC 27 November 2019. (a) As in Fig. 3.14a but for 0000 UTC 27 November 2019. (b) As in Fig. 3.14b but for 0000 UTC 27 November 2019. (c) As in Fig. 3.14c but for 0000 UTC 27 November 2019.

The total tilting frontogenesis was, once again, largely forced by the combination of ω_{uu} and ω_{um} (Fig. 3.18a) with a much smaller contribution coming from the combination of ω_{mm} and ω_{im} (Fig. 3.18b). A slightly larger contribution, unique to this particular time, arose from the sum of ω_{mu} and ω_{us} (Fig. 3.18c). The now weaker vortex tilting was dominated by that forced by the sum of ω_{uu} and ω_{um} (Fig. 3.19a), followed by comparable contributions to tilting from the combination of ω_{mm} and ω_{im} (Fig. 3.19b) as well as from the sum of ω_{mu} and ω_{us} (Fig. 3.19c).

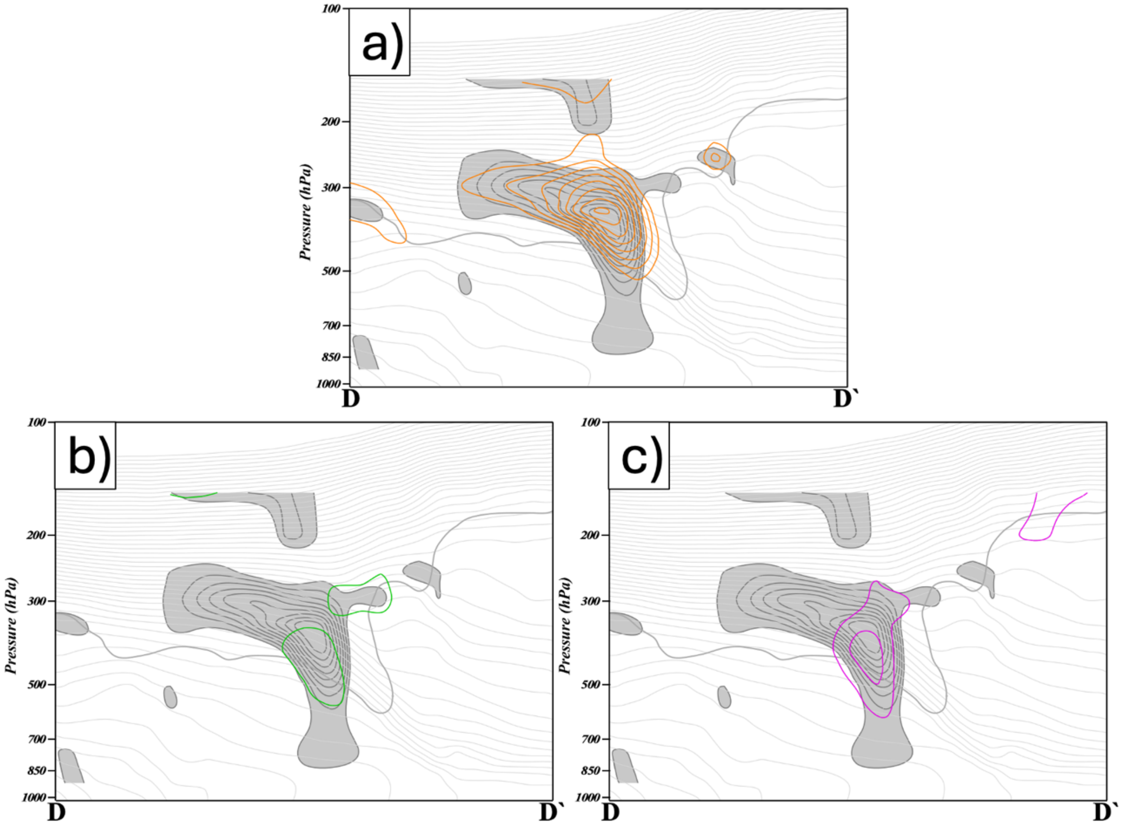

Fig. 3.18. (a) Tilting frontogenesis accomplished by ω_{um} and ω_{uu} valid at 0000 UTC 27 November 2019. Contours and shading as in Fig. 3.15a. (b) Tilting frontogenesis accomplished by ω_{mm} and ω_{im} valid at 0000 UTC 27 November 2019. Contours and shading as in Fig. 3.15b. (c) Tilting frontogenesis accomplished by ω_{mu} and ω_{us} valid at 0000 UTC 27 November 2019. Contours and shading as in Fig. 3.15c.

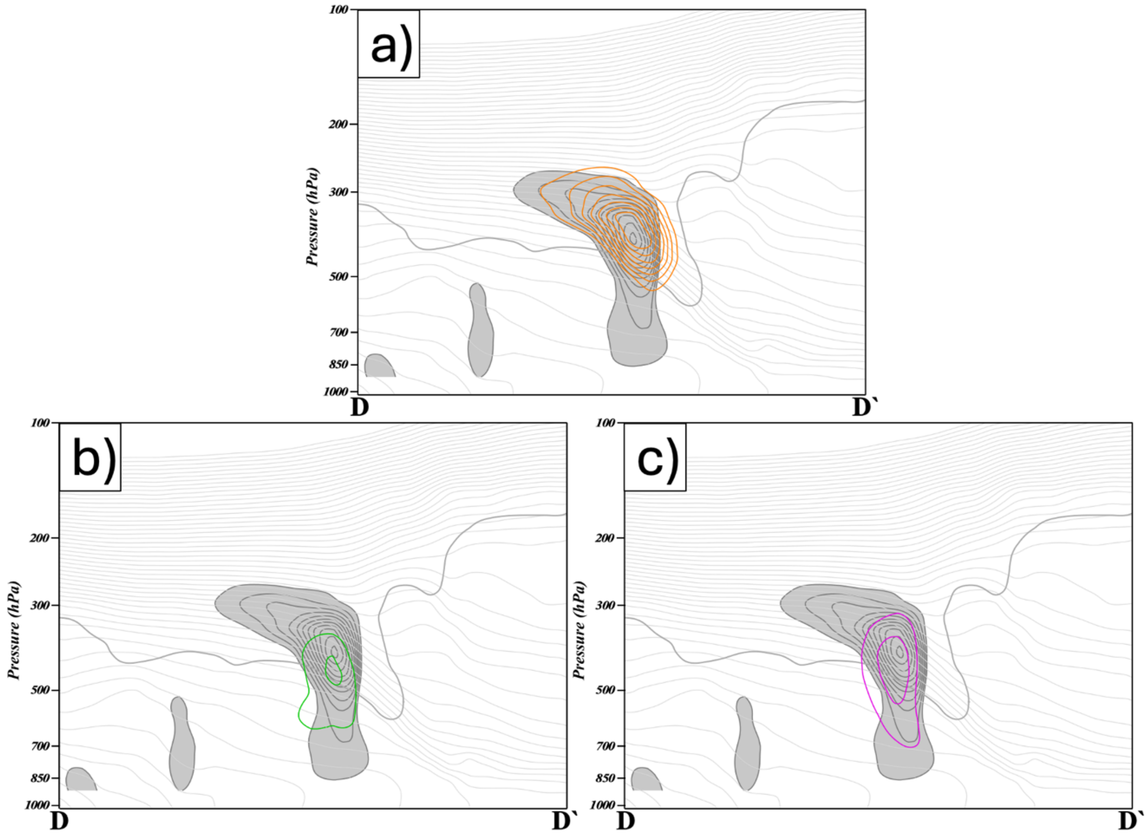

Fig. 3.19. (a) Geostrophic vorticity tendency via tilting accomplished by ω_{um} and ω_{uu} valid at 0000 UTC 27 November 2019. Contours and shading as in Fig. 3.16a. (b) Geostrophic vorticity tendency via tilting accomplished by ω_{mm} and ω_{im} valid at 0000 UTC 27 November 2019. Contours and shading as in Fig. 3.16b. (c) Geostrophic vorticity tendency via tilting accomplished by ω_{mu} and ω_{us} valid at 0000 UTC 27 November 2019. Contours and shading as in Fig. 3.16c.

3.5. Summary and Conclusions

The previous piecewise PV inversion analysis of the cyclogenesis presented in Chapter 2 offered no analysis of the development of the ULJF nor any account of its role in the remarkable surface cyclogenesis that characterized this event. In this analysis we have utilized the geostrophic wind and thermal fields associated with discrete portions of the total PV field as defined in the inversion process from Chapter 2 to investigate the development of a vigorous ULJF during a case of rapid cyclogenesis in late November 2019. The geostrophic wind and thermal fields recovered from the PV inversion process were used to calculate 16 discrete portions of the total QG-omega with the goal of delineating the separate influences of discrete portions of the total PV field on the subsidence responsible for the development of the ULJF. The differential subsidence forced tilting frontogenesis and geostrophic vorticity production via tilting in the upper-troposphere, which then encouraged intensification of the ULJF and its subsequent direct influence on the surface cyclogenesis that characterized this event.

Differential subsidence through the ULJF core, which led to an increase in horizontal baroclinicity and geostrophic relative vorticity within the ULJF region itself, primarily resulted from two different species of QG-omega acting on the background wind and thermal field. During the genesis period of the ULJF from 0600 UTC through 1200 UTC 26 November, QG-omega forced by the UPTROP winds acting on both the mean and UPTROP temperature fields was the primary driver of differential subsidence through the ULJF core and ULJF intensification. QG-omega arising from the sum of the mean and INT winds acting on the mean temperature was the second-largest driver of differential subsidence during this early period. During the later intensification period of the ULJF (from 1800 UTC 26 November through 0000 UTC 27 November), QG-omega arising from the UPTROP winds acting on the mean and UPTROP temperatures remained the primary driver of differential subsidence through the ULJF core and ULJF intensification. QG-omega forced by the mean and INT winds acting on the mean temperature field remained as the second-largest driver of differential subsidence during this later period. Nearly every combination of QG-omega forced by the INT or SFC winds resulted in negligible differential subsidence and ULJF intensification during the entire period of analysis, from 0600 UTC 26 November through 0000 UTC 27 November 2019.

The dominance of the QG-omega forced by the UPTROP winds suggests that the ULJF developed entirely without influence from the lower-tropospheric DRW during this rapid cyclogenesis event. This is notable as previous analyses of DRW rapid cyclogenesis events which followed bottom-up developments emphasized how the DRW played some role in fashioning a cyclogenetically-potent upper-tropospheric precursor disturbance which contributed to the subsequent surface cyclogenesis (Wernli et al. 2002; Boettcher and Wernli 2013; Tamarin and Kaspi 2016; Kohl and O'Gorman 2022). The fact that, in this case, the lower tropospheric DRW and its associated circulation and thermal anomalies appeared to play no substantial role in shaping the ULJF points to a serendipity at the heart of this remarkable development. It appears that this unusual surface cyclone was the product of two features, exerting no substantial developmental influence on one another, that eventually become vertically superposed and that superposition led to the period of rapid surface cyclogenesis.

With this paradigm and the analytical tools of piecewise PV inversion and partitioned QG-omega analysis in mind, it was of interest to investigate any factors which may have impacted the success of ensemble member forecasts during this rapid cyclogenesis event. In particular, we were interested in relating the strength of an ensemble member depiction of the November 2019 storm at peak intensity to different processes previously identified as crucial during this cyclogenesis event. For example, we compared the sensitivity of mean sea level pressure of the November 2019 storm at peak intensity to different ensemble member forecasts of lower-tropospheric PV, which told us how well that ensemble member captured the evolution of the DRW. Therefore, in the next Chapter, we investigated physical influences on ensemble member forecasts using a technique known as ensemble-based sensitivity analysis.

4. Ensemble-Based Forecast Sensitivity Analysis

4.1. Introduction

This Chapter represents the third part of the study of an explosively-deepening diabatic Rossby wave (DRW) in late November 2019 which set all-time minimum mean sea level pressure (MSLP) records in the states of Oregon and California, USA. The goal of the current Chapter is to investigate the sensitivities of ensemble member forecasts to processes which previous analyses suggested were crucial to this development using ensemble-based sensitivity analysis (ESA; Ancell and Hakim 2007; Hakim and and Torn 2008; Torn and Hakim 2008). Through the use of ESA, one can isolate the ensemble member forecasts which produced the strongest and the weakest NV19 storm depictions and compare variables of interest between these ensemble member forecasts to gain additional insight into controls on the NV19 storm intensity. The results of the ESA provide a complimentary analysis to the analyses offered in previous Chapters of this development with specific emphasis on the relationship between ensemble member anomalies of these certain variables of interest and cyclone intensity.

ESA is a technique which establishes linear relationships between a forecast metric and perturbed initial conditions across ensemble members using ensemble statistics. These relationships, or sensitivities, derived from ESA are equivalent to the adjoint-derived sensitivity but projected through the analysis covariance matrix (Ancell and Hakim 2007). Therefore, ESA-derived sensitivities include both the linear relationship between a forecast metric and perturbed initial conditions, as well as the relationship between any state-vector which covaries with the perturbed initial conditions. The additional relationship involving the covarying state-vector must be accounted for in order to provide meaningful results, depending on the desired outcome of the ESA. However, the utility of ESA versus a technique like adjoint-derived sensitivity analysis is that the computations are straightforward after running the perturbed ensemble member forecasts (Ancell and Hakim 2007). A plethora of synoptic-scale features have been investigated using ESA: extratropical cyclones (Ancell and Hakim 2007; Torn and Hakim

2008; Garcies and Homar 2009, 2010; Chang et al. 2013; Zheng et al. 2013; McMurdie and Ancell 2014), anticyclones (Quandt et al. 2019), tropical cyclones (Torn 2010; Ito and Wu 2013; Torn and Cook 2013; Xie et al. 2013; Torn 2014; Ren et al. 2019; Hu and Wu 2020; Liu et al. 2024), and the Mei-Yu front (Wang et al. 2021). ESA has also been applied on the mesoscale to investigate convective features (Torn and Romine 2015; Bednarczyk and Ancell 2015; Hill et al. 2016; Limpert and Houston 2018) and wind power forecasting (Smith and Ancell 2017). In the current analysis, we expand the application of ESA to the interrogation of an explosively-deepening DRW development.

A DRW is a diabatically-generated lower-tropospheric positive potential vorticity (PV) anomaly which develops underneath a region of maximum cloud production along a pre-existing baroclinic zone (Raymond and Jiang 1990; Snyder and Lindzen 1991; Parker and Thorpe 1995; Moore and Montgomery 2004, 2005). Both Rossby waves and DRWs self-propagate due to the meridional advection of planetary vorticity for Rossby waves (Rossby 1939) and θ_e for DRWs (Parker and Thorpe 1995), respectively. However, as opposed to Rossby waves, DRWs are smaller-scale waves with origins in the lower-troposphere and are dependent on latent heat release to modify the downstream PV tendency. The cyclonic vortex corresponding to the lower-tropospheric positive PV anomaly forces a region of differential positive moisture and temperature advection downstream of the vortex and along the baroclinic zone, leading to the production of clouds and precipitation over that region. These advections then regenerate the lower-tropospheric positive PV anomaly downstream of the original vortex, appearing to propagate it downstream (Parker and Thorpe 1995; Moore and Montgomery 2004, 2005; Terpstra et al. 2015; Tamarin and Kaspi 2016; Kohl and O'Gorman 2022).

DRWs are highly dependent on differential lower-tropospheric frontogenesis by virtue of the fact that the meridional moisture advection might not otherwise be converted to latent heat release along the pre-existing baroclinic zone. The differential lower-tropospheric frontogenesis mobilizes ascent, latent heat release, and the diabatic generation of PV in the lower-troposphere. If this diabatic generation of PV occurs primarily ahead of the isolated existing cyclonic vortex and the amount of latent heating remains unchanged, the vortex will only propagate downstream – no intensification of the vortex can occur.

However, if additional forcing for ascent such as an upper-tropospheric shortwave moves into the vicinity of the lower-tropospheric vortex, intensification into a substantial cyclone through mutual amplification can occur. Such developments are well-documented (Wernli et al. 2002; Moore et al. 2008; Rivière et al. 2010; Boettcher and Wernli 2011, 2013; McKenzie 2014; Tamarin and Kaspi 2016; Zhang and Wang 2018; Beaty et al. 2025). These types of developments are dependent on specific lower- and upper-tropospheric processes, some of which have been investigated in previous chapters, and all of which can be explored using ESA.

In late November 2019, a DRW rapid cyclogenesis event (hereafter known as the NV19 storm) occurred over the northeast Pacific Ocean wherein a lower-tropospheric diabatically-generated PV anomaly associated with a DRW vortex became vertically collocated with an upper-tropospheric PV anomaly associated with an intensifying upper-level jet/front system over a 24-hour period from 0000 UTC 26 November to 0000 UTC 27 November 2019. The superposition between these two PV anomalies resulted in the rapid development and intensification of a cyclone which accomplished a maximum central MSLP fall of 49 hPa in 24 hours and set all-time pressure records along the West Coast of the United States (Beaty et al. 2025). The location of most rapid intensification occurred the furthest east of all northeast Pacific Ocean explosively-deepening cyclones over 30 nonconsecutive years based on the climatologies presented in Roebber (1984), Wang and Rogers (2001), and Zhang et al. (2017). As shown in Chapter 2, this storm intensification followed a bottom-up development wherein forcing for development was initially focused in the lower-troposphere and shifted to the mid- and upper-troposphere as the storm intensified. Bottom-up development of explosive DRWs with no pre-existing upper-tropospheric forcing is rare (Boettcher and Wernli 2013).

The sequence of processes resulting in the record-breaking NV19 DRW development revealed in Chapter 2 is analyzed within ensemble member forecasts to correlate the intensity of forecasted MSLP off the California-Oregon coast near peak storm intensity to ensemble member anomalies of predetermined variables. Forecasted MSLP is a metric of particular interest as forecasts of MSLP made by the Ocean Prediction Center during the NV19 DRW development were consistently 2-3 hPa too high for the cyclone of interest when compared to the ERA5 MSLP data. This chapter is organized as follows. The method of ESA and an extension of its utility is presented in Section 4.2. A brief, reminder synoptic overview of two times of interest is offered in Section 4.3. Section 4.4 details the results of the ESA in terms of the NV19 storm evolution. Conclusions and suggestions for further analysis are offered in Section 4.5.

4.2. Ensemble-Based Sensitivity Analysis

ESA establishes a linear relationship between a forecast metric and perturbed initial conditions per ensemble member using forecast ensemble statistics, as first outlined in Hakim and Torn (2008) and explored in Ancell and Hakim (2007). For a given ensemble with *M* members, the sensitivity of an ensemble-mean value of a forecast metric $\boldsymbol{J}$ to a perturbed state variable $\boldsymbol{x}$ is given as

$$\frac{\partial J}{\partial x} = \frac{cov(\boldsymbol{J}, \boldsymbol{x})}{var(\boldsymbol{x})} \tag{13}$$

where $\boldsymbol{J}$ and $\boldsymbol{x}$ are $1 \times M$ ensemble member forecasts of the forecast metric and state variable with the ensemble mean removed, respectively; cov is the covariance between two arguments and var is the variance of an argument. The left-hand side of (13) represents a linear regression between $\boldsymbol{J}$ and $\boldsymbol{x}$, or the change in a forecast metric $\boldsymbol{J}$ for a given change in a state variable $\boldsymbol{x}$. The utility of (13) can be expanded to become a *lagged* linear regression if one substitutes a *lagged* state variable $\boldsymbol{x}$, such that the calculation becomes

$$\frac{\partial J}{\partial \boldsymbol{x_t}} = \frac{cov(\boldsymbol{J}, \boldsymbol{x_t})}{var(\boldsymbol{x_t})} \tag{14}$$

where $\boldsymbol{x_t}$ is a state variable, with the ensemble mean removed, at an earlier time t. Thus, ESA can be used to determine how a change in a lagged state variable $\boldsymbol{x_t}$ can produce a change in a forecast metric $\boldsymbol{J}$ at a specified lag time t. This change in forecast metric is statistically significant if

$$\left|\frac{\partial J}{\partial \boldsymbol{x_t}}\right| > \delta_s \tag{15}$$

where δ_s is the confidence interval of the linear regression coefficient and $\left|\frac{\partial J}{\partial \boldsymbol{x_t}}\right|$ is the absolute value of the left-hand side (14). The confidence interval for this study is chosen to be 95% following Torn and Hakim (2008). Therefore, if (15) is satisfied, we may reject the null hypothesis that changes in the lagged state variable $\boldsymbol{x_t}$ do not result in changes to the forecast metric $\boldsymbol{J}$ with 95% confidence.

ESA is performed using perturbed forecasts from the ECMWF integrated forecast system (IFS; ECMWF 2024) obtained from the Copernicus Climate Data Store. The ECMWF IFS ensemble suite has 50 ensemble members providing unique forecasts initialized at three day intervals with forecasts valid at 0000 UTC at 24-hour timesteps. This specific ensemble suite was chosen due to having a myriad of ensemble member forecasts with long maximum forecast lead time (3 days), allowing ample time for variability to grow between ensemble member forecasts. Each of the 50 ensemble members provides forecasts of geopotential height, specific humidity, temperature, zonal winds, meridional winds, and vertical velocity on the isobaric levels of 1000 hPa, 925 hPa, 850 hPa, 700 hPa, 500 hPa, 300 hPa, 200 hPa, 100 hPa, 50 hPa, and 10 hPa with a horizontal resolution of 1° × 1°. For the current application of ESA, we used ensemble member forecasts initialized at 0000 UTC 25 November 2019 and compared forecasts valid at both 0000 UTC 26 November and 0000 UTC 27 November 2019.

The forecast metric for this study was chosen as MSLP averaged across all ECMWF IFS ensemble member forecasts and over a 6° × 4.5° box from 129°W to 123°W and from 40.5°N to 45°N valid at 0000 UTC 27 November 2019 (Fig. 4.1). This location and time was chosen to correspond to the NV19 storm near peak intensity, as well as being centered on the 850 hPa positive PV anomaly representative of the DRW nature of this development. There was a distribution both in geographic location and 2-day NV19 storm MSLP forecasts off the California-Oregon coast near peak intensity (Fig. 4.1). Note that the strongest NV19 storm forecasts were located to the west and north of the entire distribution of NV19 storm forecasts. The minimum MSLP per each ECMWF IFS ensemble member 2-day forecast within the 6° × 4.5° box was recorded and the distribution of minimum MSLP is visualized in Fig. 4.2. Intensity forecasts for the NV19 storm ranged more than 20 hPa from 965 hPa to 988 hPa, with ensemble members **0**, **17**, **27**, **29**, and **45** depicting the five strongest (lowest MSLP) forecasts and ensemble members **14**, **15**, **36**, **42**, and **49** depicting the five weakest (highest MSLP) forecasts (Fig. 4.2). Note that the 2-day NV19 storm MSLP forecasts plotted in Fig. 4.1 are representative values and do not necessarily represent the full range of MSLP forecasts shown in Fig. 4.2. State variables were averaged across these five strongest and five weakest ensemble member forecasts to compare changes in MSLP off the California-Oregon coast due to changes in state variables in terms of the group of most intense and the group of least intense NV19 storm forecasts.

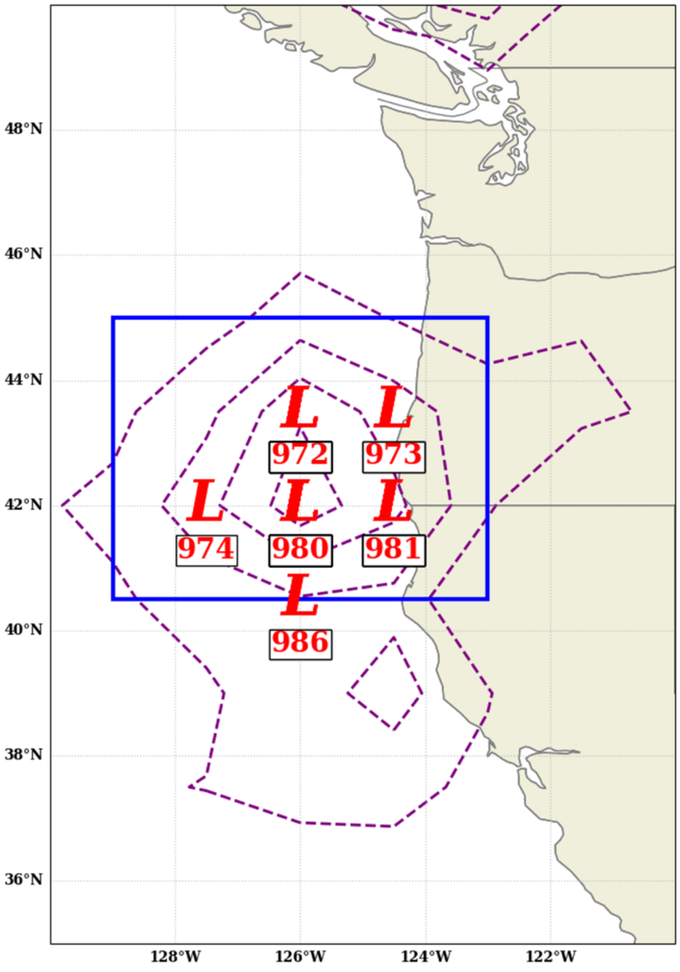

Fig. 4.1. Distribution of location and magnitude (hPa) of 2-day minimum mean sea level pressure (MSLP) forecasts across 50 ECMWF IFS ensemble members, represented as a red “L”,

within the $6^\circ \times 4.5^\circ$ blue box from 129°W to 123°W and from 40.5°N to 45°N at 0000 UTC 27 November 2019. Purple, dashed contours represent the ECMWF IFS 850 hPa potential vorticity at 0000 UTC 27 November 2019 contoured every 0.5 PVU ($1\,\mathrm{PVU} = 1 \times 10^{-6}\ \mathrm{m}^2\ \mathrm{s}^{-1}\ \mathrm{K}\ \mathrm{kg}^{-1}$) every 0.5 PVU. Note that the locations of minimum MSLP overlap between the 50 ECMWF IFS ensemble member forecasts and that the exact location of minimum MSLP is plotted halfway down the tall part of the red “L”, so the southernmost ensemble member forecast (MSLP = 986 hPa) was within the $6^\circ \times 4.5^\circ$ blue box.

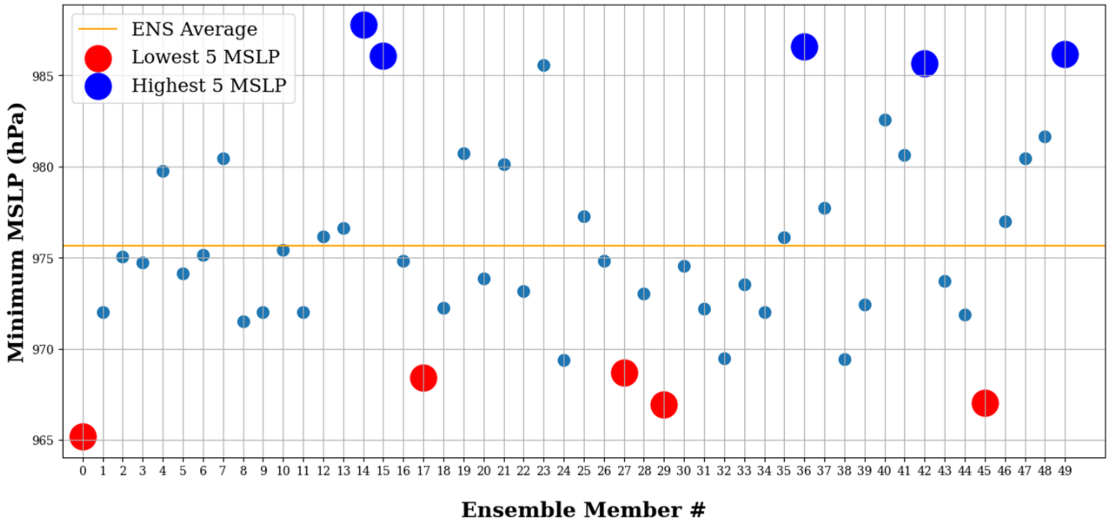

Fig. 4.2. Minimum mean sea level pressure (MSLP) per 50 ECMWF IFS ensemble member 2-day forecasts within a $6^\circ \times 4.5^\circ$ box from 129°W to 123°W and from 40.5°N to 45°N at 0000 UTC 27 November 2019. ECMWF IFS ensemble member forecasts of MSLP at 0000 UTC 27 November 2019 were initialized at 0000 UTC 25 November 2019. Average MSLP across all ensemble member forecasts is denoted by the orange line. The top five highest ensemble member MSLP forecasts are denoted by the blue circles and the top five lowest ensemble member MSLP forecasts are denoted by the red circles.

Calculating the lagged linear regression as given by (14) results in a spatial distribution of the correlation between changes in a chosen lagged state variable at time t to changes in MSLP across all ECMWF IFS ensemble members off the California-Oregon coast at 0000 UTC 27 November 2019. The calculation in (14) can be expanded to determine the actual quantitative change in MSLP across all ECMWF IFS ensemble member forecasts, rather than only the magnitude of the correlation, as was first performed in Torn and Hakim (2008). This is done by multiplying the left hand side of (14) by the standard deviation of the chosen lagged state variable at time t and averaging across all 50 ECMWF IFS ensemble members,

$$\overline{\Delta J} = \frac{1}{N_t}\sum_{t=1}^{N_t}\left(\left|\frac{\partial \boldsymbol{J}}{\partial \boldsymbol{x}}\right|_t \sigma_{x_t}\right), \tag{16}$$

where σ_{x_t} is the standard deviation of $\boldsymbol{x}$ at each individual point at time t and N_t is the number of ensemble member forecasts used in the analysis. The left hand side of (16) is hereafter referred to as the sensitivity pattern and allows for a more insightful comparison between changes in MSLP off the California-Oregon coast and a given lagged state variable. Fig. 4.3 provides an example of this idea. Consider the statistically significant region of positive correlation between 500 hPa geopotential heights to the south of Alaska at 0000 UTC 26 November and MSLP within the blue box off the California-Oregon coast 24 hours later at 0000 UTC 27 November 2019 (Fig. 4.3a). In this region, if the 500 hPa geopotential height at 0000 UTC 26 November (the lagged state variable $\boldsymbol{x_t}$) were to increase, MSLP off the California-Oregon coast 24 hours later (the forecast metric $\boldsymbol{J}$) would also increase because the correlation between the two variables is positive. This result is coherent, as the region of statistically significant positive correlation lies directly along the axis of an upstream shortwave, meaning that if 500 hPa geopotential heights increase in this region, the shortwave would weaken, and the NV19 storm would have weaker upper-tropospheric forcing for column mass evacuation and surface development.

Consider the same region of statistically significant positive correlation between 500 hPa geopotential heights and MSLP off the California-Oregon coast, now focusing on the highlighted region of positive correlation greater than 0.6 directly along the shortwave axis (Fig. 4.3a). This region has a uniform magnitude of correlation. However, the sensitivity pattern calculated in the same region using (16) reveals a varying distribution in MSLP change (Fig. 4.3b). The same 1 standard deviation (251 meters) increase in 500 hPa geopotential height within the highlighted region to the south of Alaska reveals different increases in MSLP off the California-Oregon coast 24 hours later. If 500 hPa geopotential height increases by 1 standard deviation on the poleward side of the shortwave, the MSLP increase of the NV19 storm ranges from 0.4 hPa to 1.2 hPa (Fig. 4.3b). If 500 hPa geopotential height increases by 1 standard deviation on the equatorward side of the shortwave, the MSLP increase of the NV19 storm ranges from 1.6 hPa to 2.4 hPa (Fig. 4.3b). The equatorward side of the shortwave is thus *more* sensitive to the *same* increase in 500 hPa geopotential height compared to the poleward side of the shortwave. These sensitivity pattern calculations reveal a nonuniform increase in MSLP off the California-Oregon coast at 0000 UTC 27 November 2019 with a uniform increase in 500 hPa geopotential height 24-hours earlier within the highlighted region of statistically significant positive correlation, an insight illuminated only after performing the sensitivity pattern calculation (Fig. 4.3a,b). Therefore, the sensitivity pattern after Torn and Hakim (2008) was utilized in this study due to the additional, quantifiable insight into the change in MSLP given a change in a specified state variable.

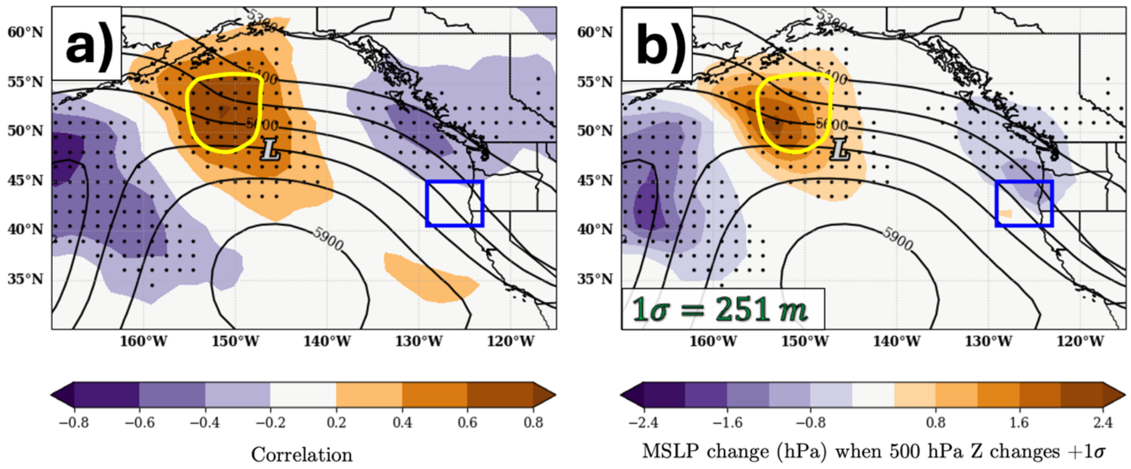

Fig. 4.3. (a) Correlation (colorfill) between ensemble member 500 hPa geopotential height forecasts at 0000 UTC 26 November 2019 and ensemble mean sea level pressure (MSLP) within the blue box 24 hours later at 0000 UTC 27 November 2019. Ensemble member mean 500 hPa geopotential height contoured in black every 100 m starting at 5400 m. Stippling represents statistical significance at the 95% confidence interval. Gray "L" denotes location of NV19 storm MSLP minimum at 0000 UTC 26 November 2019. Yellow-highlighted region denotes correlations greater than 0.6. (b) Sensitivity pattern between ensemble member 500 hPa geopotential height forecasts at 0000 UTC 26 November 2019 and ensemble MSLP within the blue box 24 hours later at 0000 UTC 27 November 2019. Colorfill represents the numerical change in MSLP in hPa at 0000 UTC 27 November 2019 in the blue box when 500 hPa geopotential height 24 hours earlier at 0000 UTC 26 November 2019 is increased by 1 standard deviation. Ensemble member mean 500 hPa geopotential height contoured in black every 100 m

starting at 5400 m. Magnitude of 1 standard deviation of 500 hPa geopotential height across all ensemble member forecasts in bottom left corner. Stippling represents statistical significance at the 95% confidence interval. Gray "L" denotes location of NV19 storm MSLP minimum at 0000 UTC 26 November 2019. Yellow-highlighted region as in (a).

Using ESA, one can relate the sensitivity of a forecast metric like MSLP in a box off the California-Oregon coast across ensemble member forecasts to *any* state variable. As noted in Section 4.1, sensitivities derived from ESA include both linear relationships between perturbed initial conditions and a forecast metric, as well as relationships between any other state-vector which covaries with the perturbed initial conditions. We would like to minimize any potential influence from the relationships between perturbed initial conditions and the covarying state variables because we are only interested in the connection between changes in perturbed initial conditions and changes in a forecast metric. Therefore, it is necessary to carefully construct the ESA such that the state variables analyzed are dynamically-appropriate for the development of interest and are reflective of a direct connection between the perturbed initial conditions and a forecast metric. Chapter 2 determined that the evolution of the NV19 storm followed a 'bottom-up' development wherein no pre-existing upper-tropospheric wave was present during initial cyclogenesis, reminiscent of Storm *Lothar* (Wernli et al. 2002). The NV19 storm development resembled a Type-C cyclogenesis event, where latent heat release in the lower- to mid-troposphere associated with vigorous differential lower-tropospheric frontogenesis was the primary forcing for surface cyclogenesis (Plant et al. 2003). After being dominated by latent heat release, the period of surface cyclogenesis prior to landfall was attributed to an intense upper-level jet/front system which first encroached upon and then became vertically-collocated with the surface cyclone. The upper-level jet/front system provided a steadily increasing, dominant forcing for mass evacuation throughout the column, cyclonic vorticity advection by the thermal wind (Sutcliffe 1947), which aided in subsequent intensification. Due to this specific evolution, the perturbed initial conditions of interest chosen during the ESA were: 850 hPa 2-D frontogenesis, 925 hPa PV, 500 hPa relative vorticity, and 500 hPa relative vorticity advection by the 300-700 hPa thermal wind. Two analysis times were investigated to determine how changes in MSLP off the California-Oregon coast at 0000 UTC 27 November 2019 were associated with the perturbed initial conditions of interest near the beginning of the NV19 storm lifecycle (0000 UTC 26 November 2019) and near the end of the NV19 storm lifecycle (0000 UTC 27 November 2019).

4.3. Synoptic Overview

The following synoptic overview of the two times of interest represents a short review of similar elements from Chapter 2. Hourly ERA5 data were extracted on a limited area domain extending from 10°N to 75°N and 180° to 90°W. Wind speed and direction, temperature, geopotential height, relative humidity, and MSLP data for the NV19 storm were collected from 0000 UTC 01 November to 2300 UTC 31 December 2019 with a horizontal grid spacing of 0.25° × 0.25° on 19 vertical levels from 1000 hPa to 100 hPa at a vertical grid spacing of 50 hPa. ERA5 data were then regridded to a grid spacing of 1.0° × 1.0°. ERA5 hourly MSLP and wind data were compared with the 3-hourly Weather Prediction Center and the 6-hourly Ocean Prediction Center Pacific surface observations to confirm their accuracy. The two timesteps of interest were selected due to their coincidence between the ERA5 hourly data and the ECMWF IFS ensemble member forecast valid times: 0000 UTC 26 November and 0000 UTC 27 November 2019. The reader is referred to Chapter 2 for the complete synoptic description of the NV19 storm.

4.3.1. 0000 UTC 26 November 2019

At 0000 UTC 26 November 2019, a weak surface cyclone was discernable along a baroclinic zone as represented in the 950 hPa θ_e which stretched zonally through an extensive anticyclone across much of the northeast Pacific basin (Fig. 4.4a). This disturbance had begun to develop its own separate cloud feature by this time (Fig. 4.4b). Positive frontogenesis along the 850 hPa baroclinic zone was primarily located to the east and northeast of the surface cyclone along the developing warm front (Fig. 4.4c). This positive frontogenesis was maximized at 800 hPa along a steep frontal zone with ascent associated with the lower-tropospheric frontogenesis extending through the mid- and lower-troposphere (Fig. 4.4d). A shortwave feature at 500 hPa was positioned to the northwest of the surface cyclone, with a maximum in positive relative vorticity located along the shortwave axis (Fig. 4.4e). The proximity of this shortwave to the surface cyclone resulted in a region of cyclonic vorticity advection (CVA) by the thermal wind just to the northwest of the position of the surface cyclone, indicative of column mean divergence and ascent (Sutcliffe 1947). The surface cyclone was situated in the right entrance region of a downstream, anticyclonically-curved jet streak at 300 hPa with decent along-flow speed change characterizing the entrance region (Fig. 4.4f).

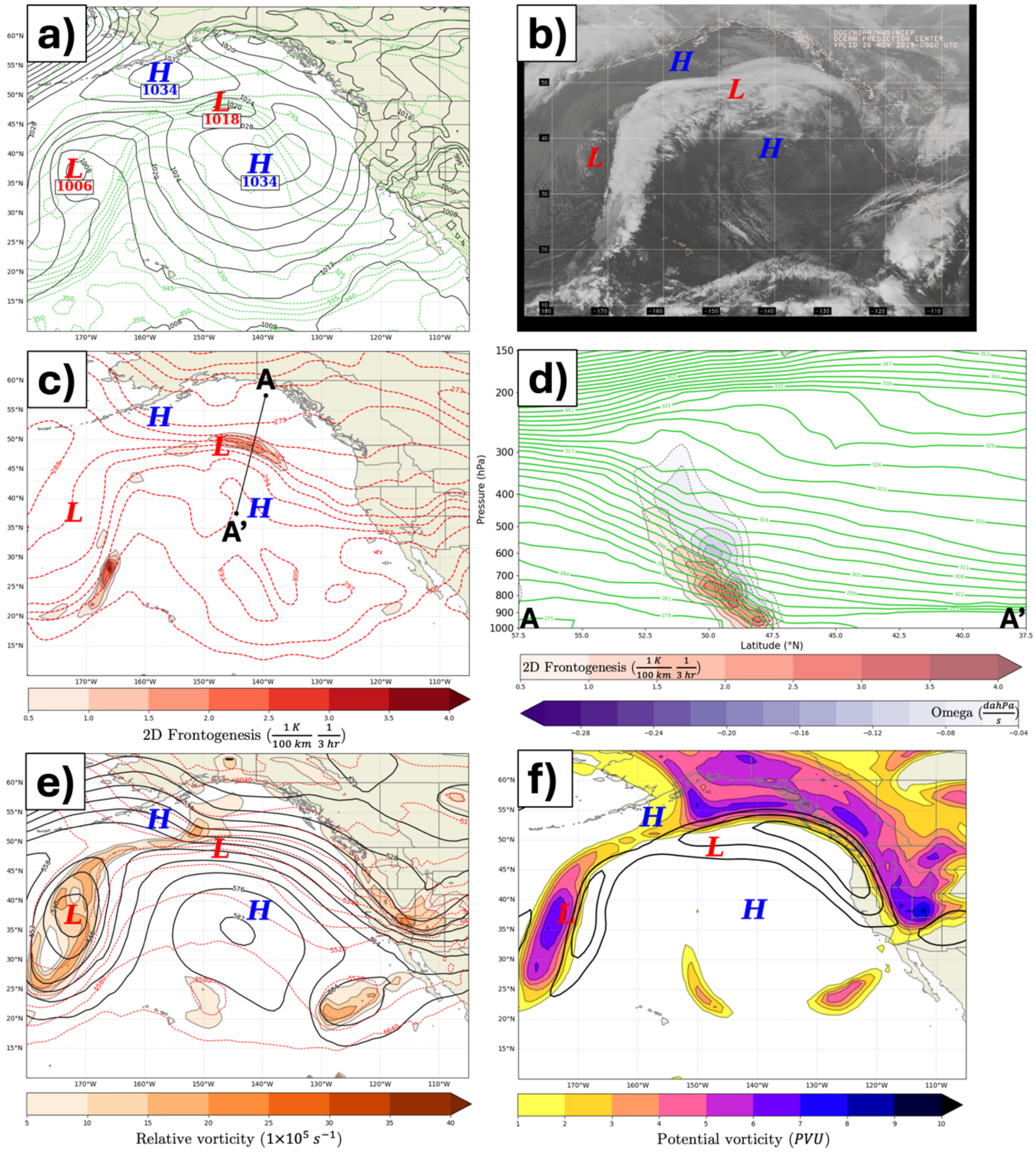

Fig. 4.4. (a) Sea-level pressure and 950 hPa equivalent potential temperature (θ_e) from the ERA5 reanalysis valid at 0000 UTC 26 November 2019. Solid, black lines are isobars contoured every 4 hPa. Dashed, green lines are 950 hPa moist isentropes contoured every 5 K. “H” denotes the centers of high pressure systems whereas “L” denotes centers of low pressure systems. “X” denotes the development region of NV19 storm. (b) GOES-17 infrared imagery of the northeast Pacific basin valid at 0000 UTC 26 November 2019. “H”, “L”, and “X” as in panel (a). (c) Potential temperature and positive horizontal frontogenesis at 850 hPa from the ERA5 reanalysis valid at 0000 UTC 26 November 2019. Dashed, red contours are isentropes contoured every 3 K. Shading indicates positive frontogenesis function values shaded every 0.5 K $(100\text{km})^{-1}$ $(3\text{hr})^{-1}$ starting at 0.5 K $(100\text{km})^{-1}$ $(3\text{hr})^{-1}$. “H”, “L”, and “X” as in panel (a). Black line indicates the cross section shown in panel (d). (d) Cross section along A-A’ in panel (c) of potential temperature, frontogenesis, and negative omega valid at 0000 UTC 26 November 2019. Potential temperature (green) contoured every 3 K starting at 300 K. Positive frontogenesis function (red shading) shaded every 0.5 K $(100\text{km})^{-1}$ $(3\text{hr})^{-1}$. Negative omega (purple dashed shading) shaded every -0.04 daPa s^{-1} starting at -0.04 daPa s^{-1}. (e) 1000 hPa – 500 hPa thickness and relative vorticity at 500 hPa from the ERA5 reanalysis valid at 0000 UTC 26 November 2019. Red dashed contours are lines of constant thickness contoured every 60 meters. Shading indicates positive relative vorticity shaded every 5×10^{-5} s^{-1} starting at 5×10^{-5} s^{-1}. “H”, “L”, and “X” as in panel (a). (f) Potential vorticity and wind speed at 300 hPa from the ERA5 reanalysis valid at 0000 UTC 26 November 2019. Solid, black contours are wind speeds contoured every 10 m s^{-1} starting at 50 m s^{-1}. Shading indicates potential vorticity at 300 hPa shaded every 0.5 PVU ($1\ \text{PVU} = 1 \times 10^{-6}$ $\text{m}^2\ \text{s}^{-1}\ \text{K}\ \text{kg}^{-1}$) starting at 0.5 PVU. “H”, “L”, and “X” as in panel (a). “L” denoting the low pressure system changed to light blue for visibility. Adapted from Beaty et al. (2025)

4.3.2. 0000 UTC 27 November 2019

At 0000 UTC 27 November, the NV19 storm was just a few hours from making landfall on the west coast of the United States near Crescent City, California (Fig. 4.5a,b). Surface winds greater than 45 m s^{-1} near the California-Oregon border and waves as high as 24 m off the California coast were a result of the intense pressure gradient to the south of the cyclone center. The positive frontogenesis at 850 hPa associated with the warm front was undoubtedly being influenced by the steep topography adjacent to the United States West Coast (Fig. 4.5c,d) which weakened the frontal structure (Fig. 4.5d). Lower-tropospheric ascent at this time reached its largest values of the cyclone lifecycle, also undoubtedly influenced by the steep topography. At 500 hPa, a well-developed trough with substantial CVA by the thermal wind and an elongated streamer of relative vorticity were still both forcing ascent in and around the surface cyclone (Fig. 4.5e). The intensified vortex strip was a manifestation of the intensification of the associated upper-level jet/front system (Fig. 4.5e,f). The jet streak to the west of the surface cyclone increased in intensity and the surface cyclone was now located in the left exit region (Fig. 4.5f). The 300 hPa PV and 500 hPa vorticity were all maximized at the same location directly above the surface cyclone signifying a vertically stacked NV19 storm (Fig. 4.5e,f).

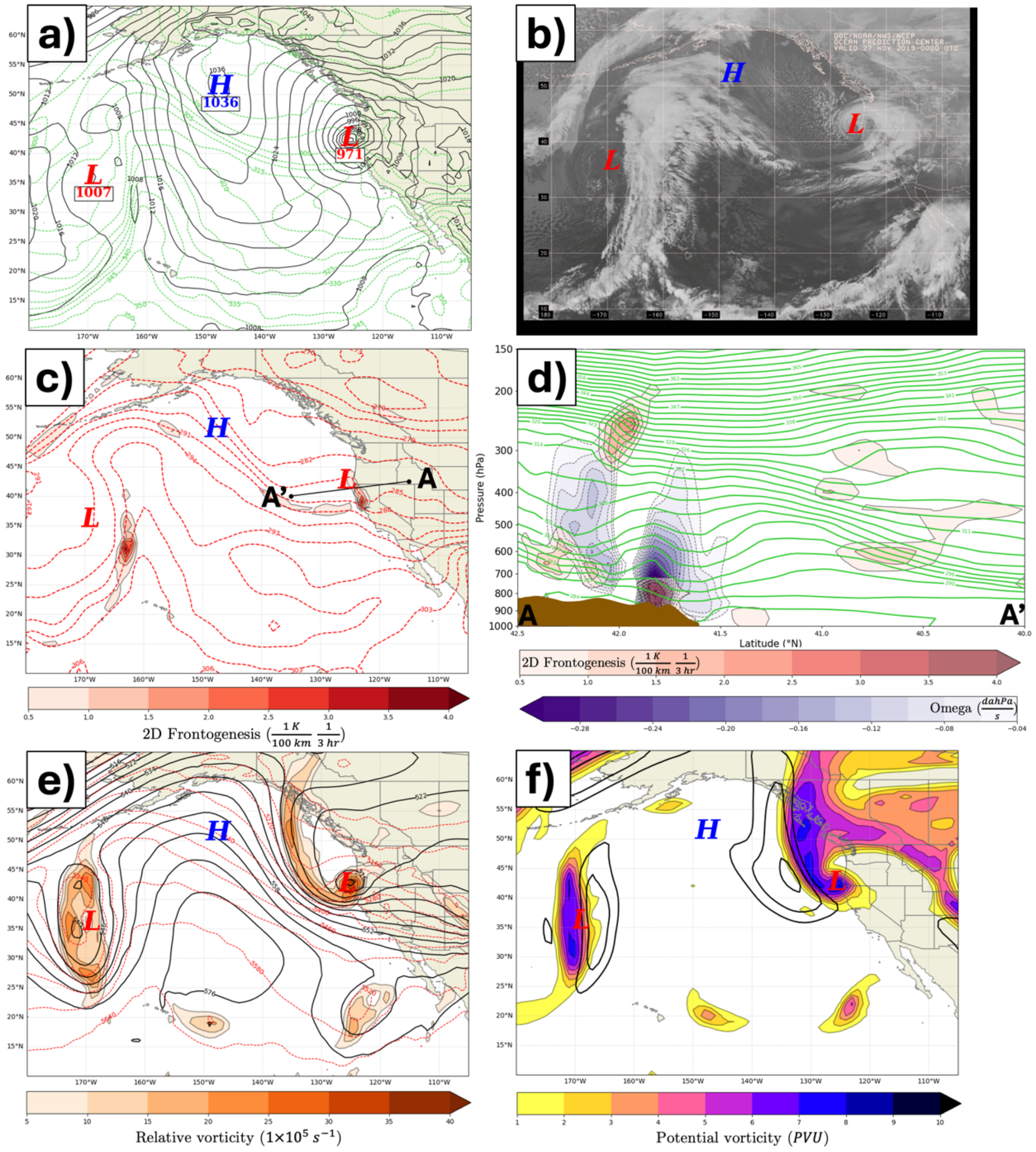

Fig. 4.5. (a) As in Fig. 4.4a except for 0000 UTC 27 November 2019. (b) As in Fig. 4.4b except for 0000 UTC 27 November 2019. (c) As in Fig. 4.4c except for 0000 UTC 27 November 2019. (d) As in Fig. 4.4d except for 0000 UTC 27 November 2019. (e) As in Fig. 4.4e except for 0000 UTC 27 November 2019. (f) As in Fig. 4.4f except for 0000 UTC 27 November 2019.

4.4. Results

In the following section, calculations of the sensitivity pattern and ensemble member anomalies relative to the ensemble mean for a 24-hour lead time (forecasts initialized at 0000 UTC 25 November 2019 and valid at 0000 UTC 26 November 2019) are shown in panels (a)-(c) and the sensitivity pattern and ensemble member anomalies relative to the ensemble mean for a 48-hour lead time (forecasts initialized at 0000 UTC 25 November 2019 and valid at 0000 UTC 27 November 2019) are shown in panels (d)-(f). Ensemble member anomalies relative to the ensemble mean averaged over the five ensemble members with the strongest NV19 storm (lowest MSLP) forecasts at 0000 UTC 27 November 2019 off the California-Oregon coast are shown in panels (b) and (e) and ensemble member anomalies relative to the ensemble mean averaged over the five ensemble members with the weakest NV19 storm (highest MSLP) forecasts at 0000 UTC 27 November 2019 off the California-Oregon coast are shown in panels (c) and (f). The sensitivity pattern of MSLP change off the California-Oregon coast at 0000 UTC 27 November 2019 for a given state variable was compared relative to itself at two different forecast lead times. The combination of the sensitivity pattern of MSLP change and the ensemble member anomalies for a given state variable were then compared to the evolution of the NV19 storm provided in Chapter 2 to offer physical support for these ESA results.

4.4.1. 850 hPa 2-D Frontogenesis

The sensitivity pattern of MSLP at 0000 UTC 27 November 2019 to 850 hPa 2-D frontogenesis ($\mathfrak{I}$) was first analyzed as differential frontogenesis at the intersection of a zonally-oriented baroclinic zone across the northeast Pacific and a meridionally-oriented high θ_e plume from the subtropics initially spawned the DRW vortex, which then became the NV19 bomb cyclone. A band of positive ensemble mean 850 hPa $\mathfrak{I}$ was situated to the north and east of the NV19 storm at 0000 UTC 26 November 2019, with a maximum immediately northeast of the cyclone center (Fig. 4.6a). Ensemble average MSLP within the blue box off the California-Oregon coast at 0000 UTC 27 November decreased up to 0.8 hPa with a $+1$ standard deviation increase in 850 hPa $\Im$ to the north and east of the cyclone (Fig. 4.6a). The top five strongest ensemble members shifted the band of maximum 850 hPa $\Im$ to the east whereas the top five weakest ensemble members shifted the band of maximum 850 hPa $\Im$ to the southwest and diminished its strength (Fig. 4.6b,c). A possible physical interpretation for this notable difference is that increasing 850 hPa $\Im$ to the east of the cyclone at 0000 UTC 26 November would strengthen diabatic production of lower-tropospheric PV in the direction of the DRW propagation, which would enhance the lower-tropospheric vortex and would result in a stronger NV19 storm.

Twenty-four hours later, at 0000 UTC 27 November 2019, a maximum in ensemble mean 850 hPa $\Im$ was located to the southeast of the cyclone center, with an extension of the ensemble mean 850 hPa $\Im$ along the now-developed cold front (Fig. 4.6d). Ensemble average MSLP off the California-Oregon coast decreased more than 2.4 hPa with a $+1$ standard deviation increase in 850 hPa $\Im$ immediately north of the cyclone center (Fig. 4.6d). The top five strongest ensemble members shifted the coastal maximum in 850 hPa $\Im$ to the north and expanded its spatial extent while the top five weakest ensemble members shifted the coastal maximum in 850 hPa $\Im$ to the south and decreased its spatial extent (Fig. 4.6e,f). The northward shift in ensemble mean 850 hPa $\Im$ would position the maximum $\Im$ directly to east of the surface cyclone, which would aid in diabatic production of lower-tropospheric PV and an enhancement of the lower-tropospheric cyclonic vortex over the region where the NV19 storm made landfall 3 hours later.

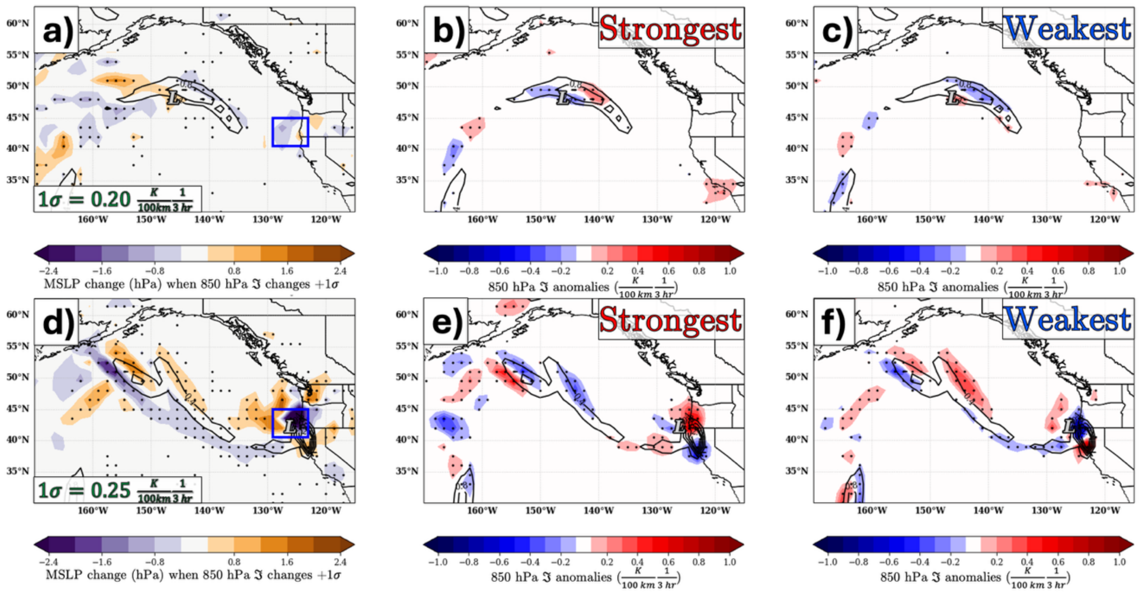

Fig. 4.6. (a) Sensitivity pattern between ensemble member 850 hPa 2-D frontogenesis ($\mathfrak{I}$) forecasts at 0000 UTC 26 November 2019 and ensemble MSLP within the blue box 24 hours later at 0000 UTC 27 November 2019. Colorfill represents the numerical change in MSLP in hPa at 0000 UTC 27 November 2019 in the blue box when 850 hPa $\mathfrak{I}$ is increased by 1 standard deviation 24 hours earlier at 0000 UTC 26 November 2019 across all ensemble member forecasts. Ensemble member mean 850 hPa $\mathfrak{I}$ contoured in black every 0.4 $\frac{K}{100\ km}\frac{1}{3\ hr}$ starting at 0.4 $\frac{K}{100\ km}\frac{1}{3\ hr}$. Magnitude of 1 standard deviation of 850 hPa $\mathfrak{I}$ in bottom left corner. Stippling represents statistical significance at the 95% confidence interval using a Student's t-test. Gray "L" denotes location of NV19 storm MSLP minimum at 0000 UTC 26 November 2019. (b) Ensemble member mean and anomalies relative to the ensemble member mean of 850 hPa $\mathfrak{I}$ at 0000 UTC 26 November 2019 averaged across the top five lowest ensemble member MSLP forecasts as in Fig. 4.2. 850 hPa $\mathfrak{I}$ anomalies shaded every 0.1 $\frac{K}{100\ km}\frac{1}{3\ hr}$ with positive anomalies shaded in red and negative anomalies shaded in blue. Ensemble member mean 850 hPa $\mathfrak{I}$ as in (a). Stippling represents statistical significance at the 95% confidence interval. Gray "L" denotes location of NV19 storm MSLP minimum at 0000 UTC 26 November 2019. (c) Ensemble member mean and anomalies of 850 hPa $\mathfrak{I}$ at 0000 UTC 26 November 2019 averaged across the top five highest ensemble member MSLP forecasts as in Fig. 4.2. Ensemble member 850 hPa $\mathfrak{I}$ mean and anomalies shaded as in (b). Stippling as in (b). Gray "L" as in (b). (d) Sensitivity pattern between ensemble member 850 hPa 2-D frontogenesis ($\mathfrak{I}$) forecasts at 0000 UTC 27 November 2019 and ensemble MSLP within the blue box at 0000 UTC 27 November 2019. Colorfill as in (a). Ensemble member mean 850 hPa $\mathfrak{I}$ contoured as in (a). Stippling as in (a). (e) As in (b) but for 0000 UTC 27 November 2019. (f) As in (c) but for 0000 UTC 27 November 2019.

4.4.2. 925 hPa Potential Vorticity

Then, the sensitivity pattern of MSLP at 0000 UTC 27 November 2019 to 925 hPa PV was investigated as DRW intensification tied to the diabatically-generated lower-tropospheric PV continued propagating the NV19 storm to the east after initial vortex generation. At 0000 UTC 26 November 2019, one maxima in ensemble mean 925 hPa PV was situated due west of the cyclone and a band of ensemble mean 925 hPa PV greater than 0.6 PVU was located underneath the high θ_e and cloud plume which extended meridionally from the subtropics (Fig. 4.4a,b, and Fig. 4.7a). Ensemble member average MSLP off the California-Oregon coast at 0000 UTC 27 November decreased up to 0.8 hPa with a $+1$ standard deviation increase in 925 hPa PV to the west, north, and east of the cyclone center (Fig. 4.7a). Additionally, the sensitivity pattern of alternating positive and negative sensitivities surrounding the ensemble mean maximum 925 hPa PV suggests the existence of a barotropic growth structure tilting upshear on either side of the low-level jet maximum. Assuming that this structure exists and is located along the axis of the low-level jet, this structure would be capable of growing at the expense of the shear as previously identified in sensitivity studies of east Pacific tropical cyclogenesis (Hoover 2015) and idealized midlatitude cyclogenesis (Langland et al. 1995).

The top five strongest ensemble members forecasted 925 hPa PV in similar locations as the ensemble mean 925 hPa PV with PV anomalies less than ±1 standard deviation to the southwest of the cyclone (Fig. 4.7b). The top five weakest ensemble members also forecasted 925 hPa PV similar to the ensemble mean 925 hPa PV with a confined PV anomaly less than -1 standard deviation to the east of the cyclone (Fig. 4.7c). It is noteworthy that both the five strongest and five weakest ensemble member 925 hPa PV forecasts agreed in terms of spatial orientation and magnitude (Fig. 4.7b,c). This was similarly true for the five strongest and five weakest ensemble member forecasts of 850 hPa and 700 hPa PV valid at the same time (not shown). This independence between 925 hPa PV and MSLP off the California-Oregon coast suggests that forecasts of NV19 storm strength at 0000 UTC 27 November 2019 were not substantially dictated by PV in the lower-troposphere 24 hours earlier.

An increase in 925 hPa PV directly over the cyclone center was noted in the ensemble mean PV as the NV19 storm intensified over the following twenty-four hours (Fig. 4.7d). The sensitivity pattern of MSLP off the California-Oregon coast now featured a more than 2.4 hPa decrease in MSLP with a $+1$ standard deviation increase in 925 hPa PV to the west and north of the cyclone center (Fig. 4.7d). The top five strongest ensemble members strengthened the 925 hPa PV maximum by nearly $+1$ standard deviation over the cyclone center and shifted the maximum slightly to the northwest while the top five weakest ensemble members decreased the 925 hPa PV maximum by -1 standard deviation and shifted it to the south (Fig. 4.7e,f). Lower-tropospheric PV increasing to the northwest of the NV19 storm suggests a slower propagation speed in the ensemble member forecasts, which would allow for a longer duration interaction between the lower-tropospheric vortex and the upper-level jet/front system as well as limit the interaction of the cyclone with steep orography along the United States West Coast.

Note that in both the 850 hPa $\mathfrak{I}$ and the 925 hPa PV there was still substantial sensitivity of MSLP off the California-Oregon coast at 0000 UTC 27 November 2019 to the meridionally-oriented high θ_e plume from the subtropics which remained stationary between 160°W and 150°W (Fig. 4.6d,Fig. 4.7d). While the sensitivity extending well to the west of the NV19 storm even at this late stage in storm lifecycle might be caused by spurious correlations, it is also justifiable due to the connection between the NV19 storm and lower-tropospheric baroclinicity along the poleward side of the expansive thermal ridge to the south of the Aleutian Islands (Fig. 4.5a,c). This connection across the northeast Pacific basin severed several hours after the NV19 storm made landfall (not shown).

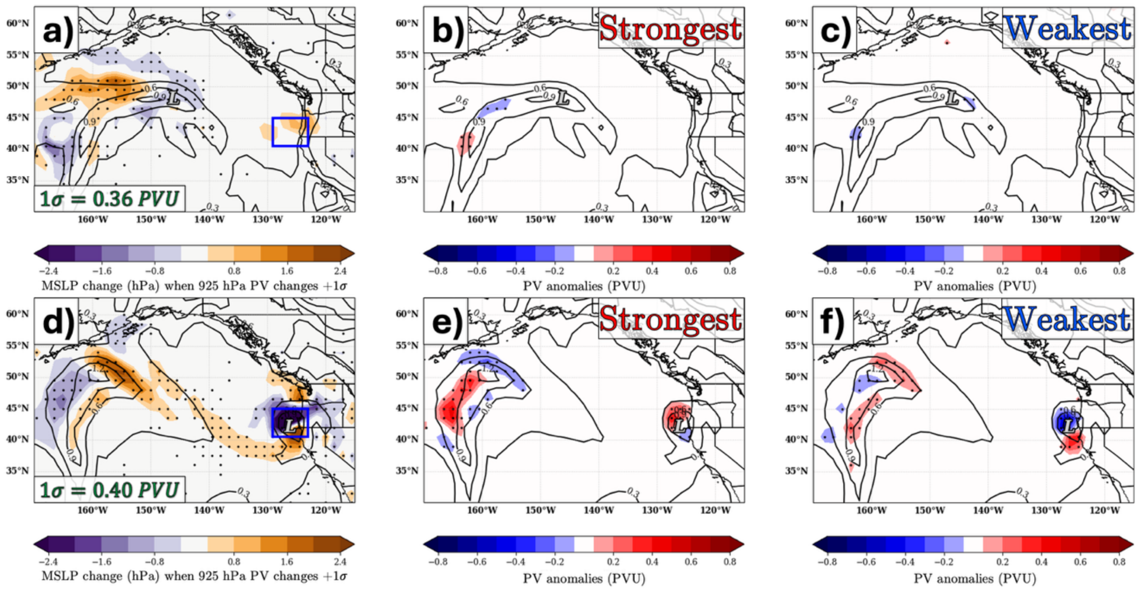

Fig. 4.7. (a) Sensitivity pattern between ensemble member 925 hPa potential vorticity (PV) forecasts at 0000 UTC 26 November 2019 and ensemble MSLP within the blue box 24 hours later at 0000 UTC 27 November 2019. Colorfill as in Fig. 4.6a but for a 1 standard deviation increase in 925 hPa PV. Ensemble member mean 925 hPa PV contoured in black every 0.3 PVU starting at 0.3 PVU where ($1\,\text{PVU} = 1 \times 10^{-6}$ m^2 s^{-1} K kg^{-1}). Magnitude of 1 standard deviation of 925 hPa PV in bottom left corner. Stippling represents statistical significance at the 95% confidence interval. Gray "L" denotes location of NV19 storm MSLP minimum at 0000 UTC 26 November 2019. (b) Ensemble member mean and anomalies of 925 hPa PV at 0000 UTC 26 November 2019 averaged across the top five lowest ensemble member MSLP forecasts as in Fig. 4.2. 925 hPa PV anomalies shaded every 0.1 PVU with positive anomalies shaded in red and negative anomalies shaded in blue. Ensemble member mean 925 hPa PV as in (a). Stippling as in (a). Gray "L" as in (a). (c) Ensemble member mean and anomalies of 925 hPa PV at 0000 UTC 26 November 2019 averaged across the top five highest ensemble member MSLP forecasts as in Fig. 4.2. Ensemble member 925 hPa PV mean and anomalies shaded as in (b). Stippling as in (b). Gray "L" as in (b). (d) Sensitivity pattern between ensemble member 925 hPa PV forecasts at 0000 UTC 27 November 2019 and ensemble MSLP within the blue box at 0000 UTC 27 November 2019. Colorfill as in (a). Ensemble member mean 925 hPa PV contoured as in (a). Stippling as in (a). (e) As in (b) but for 0000 UTC 27 November 2019. (f) As in (c) but for 0000 UTC 27 November 2019.

4.4.3. 500 hPa Relative Vorticity

Next, the sensitivity pattern between MSLP in the area of interest at 0000 UTC 27 November 2019 and 500 hPa relative vorticity (ζ) was analyzed as the upper-tropospheric shortwave which originated over mainland Alaska enhanced the intensification of the lower-tropospheric DRW and NV19 storm through mutual amplification in the latter half of its lifecycle. A region of ensemble mean maximum 500 hPa ζ was positioned to the northwest of the cyclone center at 0000 UTC 26 November 2019, at the base of a 500 hPa shortwave trough (Fig. 4.4e, Fig. 4.8a). Ensemble average MSLP off the California-Oregon coast twenty-four hours later decreased up to 2.0 hPa with a $+1$ standard deviation increase in 500 hPa ζ to the southwest of the shortwave (Fig. 4.8a). The top five strongest ensemble members exhibited a westward shift in the maximum 500 hPa ζ at the base of the shortwave with an indication of a subtle southward shift as well due to the statistically significant positive 500 hPa ζ anomaly around 159°W (Fig. 4.8b). The top five weakest ensemble members exhibited an eastward shift of the maximum 500 hPa ζ (Fig. 4.8c).

A westward shift in the 500 hPa ζ implies a delayed interaction between the upper-tropospheric shortwave and the lower-tropospheric DRW, which would also delay the upper-tropospheric forcing for column mass evacuation and surface cyclogenesis. However, a westward shifted upper-tropospheric shortwave might have more potential to independently intensify, as supported by the results in Chapter 3, which would mean more intense column mass evacuation and surface cyclogenesis when it moved in proximity to the surface cyclone. This westward shift and delayed interaction still resulted in an increase in strength of the NV19 storm twenty-four hours later as was reflected in the five strongest ensemble member forecasts. This curious result is further explored in the conclusions section.

The 500 hPa shortwave developed into a substantial large-scale trough as the NV19 storm strengthened, which is reflected in the escalation of the ensemble mean 500 hPa ζ through the core of the trough (Fig. 4.5e, Fig. 4.8d). Ensemble average MSLP off the California-Oregon coast decreased more than 2.4 hPa with a $+1$ standard deviation increase in 500 hPa ζ directly over and to the north and east of the cyclone center at 0000 UTC 27 November 2019 (Fig. 4.8d). The top five strongest ensemble members forecasted a westward displacement in the tail of 500 hPa ζ centered on 135°W as well as a northward expansion in the 500 hPa ζ maximum over the cyclone center (Fig. 4.8e). The top five weakest ensemble members forecasted the large-scale trough to the north of the ensemble mean 500 hPa ζ due to the orientation of the positive 500 hPa ζ anomalies to the north of the ensemble mean 500 hPa ζ (Fig. 4.8f). Displacing the large-scale trough to the west at 0000 UTC 27 November 2019 would increase the potential for cyclogenetic processes such as cyclonic vorticity advection by the thermal wind over the cyclone center just before landfall, providing the NV19 storm with additional column mass evacuation and intensification (Fig. 4.8d,e; Sutcliffe 1947).

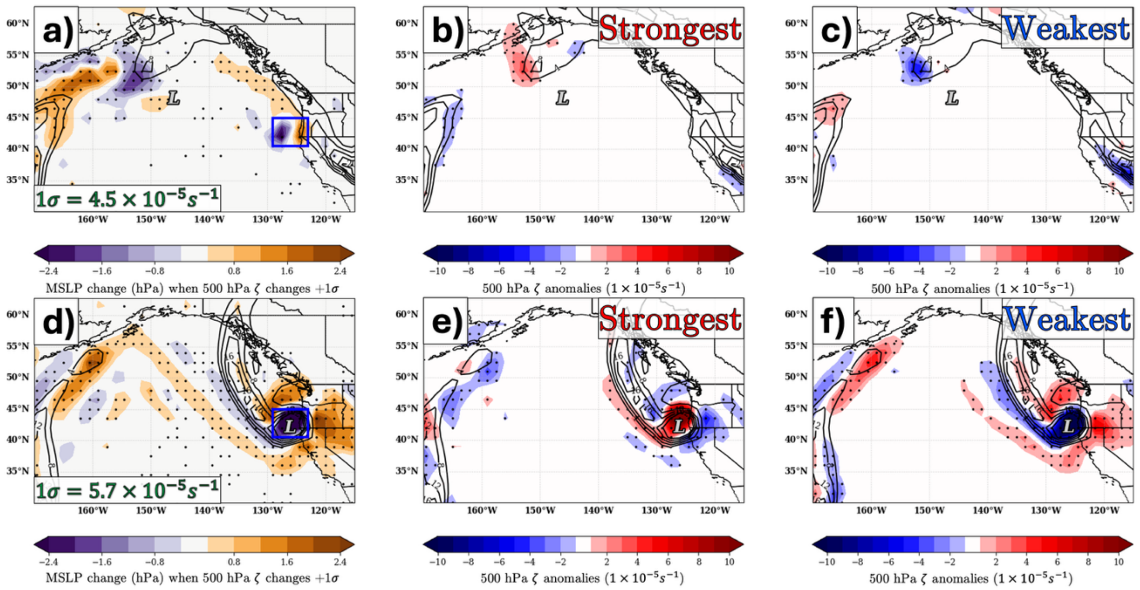

Fig. 4.8. (a) Sensitivity pattern between ensemble member 500 hPa relative vorticity forecasts at 0000 UTC 26 November 2019 and ensemble MSLP within the blue box 24 hours later at 0000 UTC 27 November 2019. Colorfill as in Fig. 4.7a but for a 1 standard deviation increase in 500 hPa relative vorticity. Ensemble member mean 500 hPa relative vorticity contoured in black every $4 \times 10^{-5}\ \frac{1}{s}$ starting at $4\ \times 10^{-5}\ \frac{1}{s}$. Magnitude of 1 standard deviation of 500 hPa relative vorticity in bottom left corner. Stippling represents statistical significance at the 95% confidence interval. Gray "L" denotes location of NV19 storm MSLP minimum at 0000 UTC 26 November 2019. (b) Ensemble member mean and anomalies of 500 hPa relative vorticity at 0000 UTC 26 November 2019 averaged across the top five lowest ensemble member MSLP forecasts as in Fig. 4.2. 500 hPa relative vorticity anomalies shaded every $1 \times 10^{-5}\ \frac{1}{s}$ with positive anomalies shaded in red and negative anomalies shaded in blue. Ensemble member mean 500 hPa relative vorticity as in (a). Stippling as in (a). Gray "L" as in (a). (c) Ensemble member mean and anomalies of 500 hPa relative vorticity at 0000 UTC 26 November 2019 averaged across the top five highest ensemble member MSLP forecasts as in Fig. 4.2. Ensemble member 500 hPa relative vorticity mean and anomalies shaded as in (b). Stippling as in (b). Gray "L" as in (b). (d) Sensitivity pattern between ensemble member 500 hPa relative vorticity forecasts at 0000 UTC

27 November 2019 and ensemble MSLP within the blue box at 0000 UTC 27 November 2019. Colorfill as in (a). Ensemble member mean 500 hPa relative vorticity contoured as in (a). Stippling as in (a). (e) As in (b) but for 0000 UTC 27 November 2019. (f) As in (c) but for 0000 UTC 27 November 2019.

4.4.3.1. 500 hPa Shear and Curvature Vorticity

The geostrophic relative vorticity, ζ_g, can be partitioned into its shear and curvature components starting from the natural coordinate expression for ζ_g (Holton and Hakim 2013);

$$\zeta_g = -\frac{\partial V}{\partial n} + \frac{V}{R_s}, \tag{17}$$

where V is the magnitude of the geostrophic wind, R_s is the radius of curvature of the streamlines, and $\hat{n}$ is the natural coordinate direction pointing into the cold air (i.e. $\hat{n} = -\frac{\nabla\theta}{|\nabla\theta|}$). A transformation of (17) from the natural coordinate version into Cartesian coordinates more amenable for calculation with gridded datasets is provided in Bell and Keyser (1993). Specifically, the shear vorticity is given by

$$-\frac{\partial V}{\partial n} = -\frac{1}{V^2}\left\{u_g^2\left(\frac{\partial u_g}{\partial y}\right) - v_g^2\left(\frac{\partial v_g}{\partial x}\right) - (u_g v_g)\left(\frac{\partial u_g}{\partial x} - \frac{\partial v_g}{\partial y}\right)\right\}, \tag{18}$$

while the curvature vorticity is given by

$$\frac{V}{R_s} = \frac{1}{V^2}\left\{u_g^2\left(\frac{\partial v_g}{\partial x}\right) - v_g^2\left(\frac{\partial u_g}{\partial y}\right) - (u_g v_g)\left(\frac{\partial u_g}{\partial x} - \frac{\partial v_g}{\partial y}\right)\right\}. \tag{19}$$

Equations (18) and (19) were also included in the ESA due to the additional insight provided by the sensitivities to the 500 hPa shear vorticity, ζ_s, and the 500 hPa curvature vorticity, ζ_c.

The region of ensemble mean 500 hPa ζ to the northwest of the cyclone center at 0000 UTC 26 November 2019 (Fig. 4.8a) was primarily a region of ζ_c as the shortwave trough featured modest cyclonic curvature with largely uniform shear (Fig. 4.4, Fig. 4.9a, and Fig. 4.10a). Ensemble average MSLP off the California-Oregon coast at 0000 UTC 27 November 2019 decreased up to 1.6 hPa with a +1 standard deviation increase in 500 hPa ζ_s to the northwest of the shortwave (Fig. 4.9a) and up to 2.4 hPa with a +1 standard deviation increase in 500 hPa ζ_c to the west of the shortwave (Fig. 4.10a). The top five strongest ensemble members showed an increase in 500 hPa ζ_s to the northwest of the cyclone (Fig. 4.9b) and a southwestward shift in the 500 hPa ζ_c maximum (Fig. 4.10b). The top five weakest ensemble members forecasted a decrease in 500 hPa ζ_s to the northwest of the cyclone (Fig. 4.9c) and an eastward shift in the 500 hPa ζ_c maximum (Fig. 4.10c). Therefore, the westward shift and delayed interaction between the upper-tropospheric shortwave and the lower-tropospheric DRW seen in the strongest ensemble member forecasts was due to 500 hPa ζ_c at this time.

Twenty-four hours later, at 0000 UTC 27 November 2019, the ensemble mean 500 hPa ζ_s and ζ_c became prominent features in and around the development region (Fig. 4.9d,Fig. 4.10d). Both components of vorticity featured MSLP decreases more than 2.4 hPa with a $+1$ standard deviation increase in either 500 hPa ζ_s or 500 hPa ζ_c directly over the development region. Now, however, the westward displacement of the trough, and increase in cyclogenetic potential at this late stage of development, implied by the top five strongest ensemble members is a function of ζ_s (Fig. 4.8e, Fig. 4.9e). The northward shift forecasted by the top five weakest ensemble members was seen in the anomaly field of both ζ_s and ζ_c (Fig. 4.9f,Fig. 4.10f). There was a switch in the dominant control on the westward shift of the upper-tropospheric shortwave implied by the top five strongest ensemble member forecasts of vorticity. This westward shift was highlighted in the ζ_c at 0000 UTC 26 November (Fig. 4.10b) and in the ζ_s at 0000 UTC 27 November (Fig. 4.9e) over the 24 period when the cyclone was undergoing rapid development. This is particularly curious as the evolution of the dominant component of vorticity typically begins with ζ_s and ends with ζ_c during cyclogenesis events (e.g. Bell and Keyser 1993).

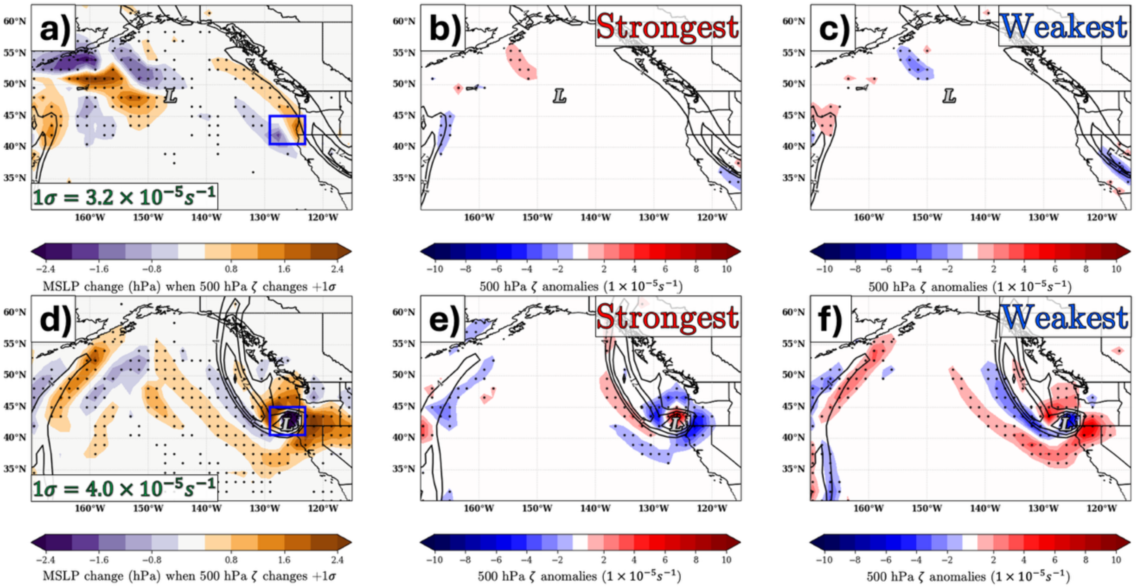

Fig. 4.9. (a) As in Fig. 4.8a but for 500 hPa shear vorticity. (b) As in Fig. 4.8b but for 500 hPa shear vorticity. (c) As in Fig. 4.8c but for 500 hPa shear vorticity. (d) As in Fig. 4.8d but for 500 hPa shear vorticity. (e) As in Fig. 4.8e but for 500 hPa shear vorticity. (f) As in Fig. 4.8f but for 500 hPa shear vorticity.

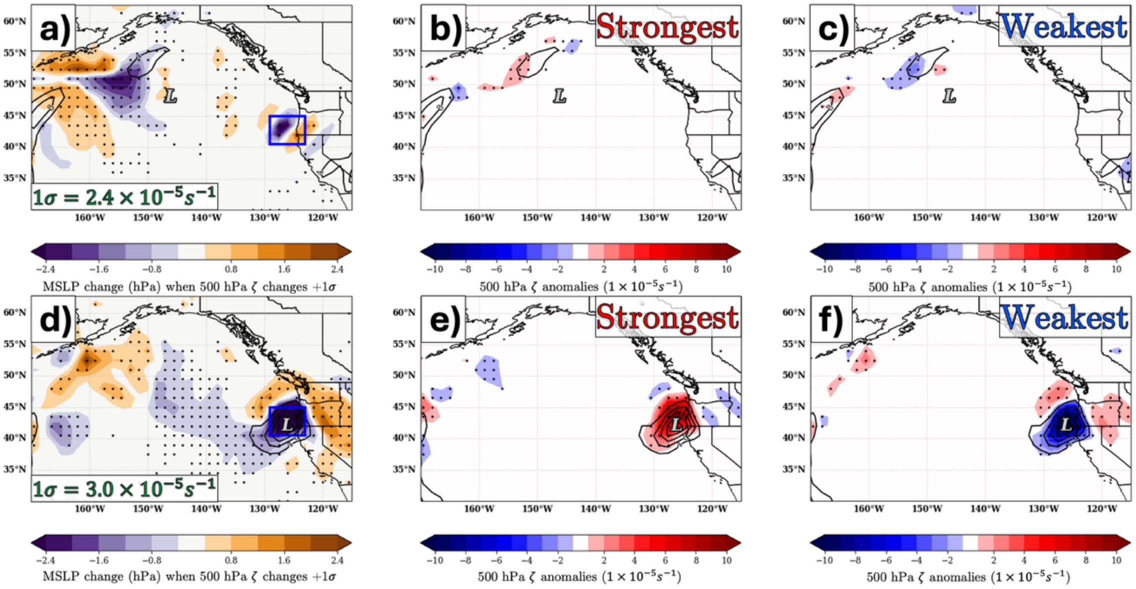

Fig. 4.10. (a) As in Fig. 4.9a but for 500 hPa curvature vorticity. (b) As in Fig. 4.9b but for 500 hPa curvature vorticity. (c) As in Fig. 4.9c but for 500 hPa curvature vorticity. (d) As in Fig.

4.9d but for 500 hPa curvature vorticity. (e) As in Fig. 4.9e but for 500 hPa curvature vorticity. (f) As in Fig. 4.9f but for 500 hPa curvature vorticity.

4.4.4. 500 hPa Cyclonic Vorticity Advection by the 300-700 hPa Thermal Wind

Finally, as noted in Section 4.4.3 and in Chapters 2 and 3, cyclonic vorticity advection of 500 hPa ζ by the 300-700 hPa thermal wind (CVA by $\vec{V}_T$; Sutcliffe 1947) was a crucial component for cyclogenesis in the later stage of the NV19 storm lifecycle. From the ECMWF IFS ensemble suite, there was a maximum in ensemble mean CVA by $\vec{V}_T$ to the northwest of the cyclone center at 0000 UTC 26 November 2019 (Fig. 4.11a). The sensitivity pattern between MSLP off the California-Oregon coast at 0000 UTC 27 November and CVA by $\vec{V}_T$ twenty-four hours earlier showed a decrease in MSLP up to 1.2 hPa with a $+1$ standard deviation increase in CVA by $\vec{V}_T$ to the west of the ensemble mean CVA by $\vec{V}_T$ maximum (Fig. 4.11a). The top five strongest ensemble members forecasted a similar increase in CVA by $\vec{V}_T$ to the west of the ensemble mean maximum with CVA by $\vec{V}_T$ anomalies greater than $+2$ standard deviations (Fig. 4.11b). The top five weakest ensemble members forecasted the ensemble mean CVA by $\vec{V}_T$ maximum to be zonally elongated due to the tri-pole in CVA by $\vec{V}_T$ anomalies up to ± 3 standard deviations straddling 150°W (Fig. 4.11c). Increasing CVA by $\vec{V}_T$ to the west of the ensemble mean CVA by $\vec{V}_T$ maximum at 0000 UTC 26 November 2019 suggests a westward shift in the 500 hPa shortwave like that reflected in the sensitivity to 500 hPa ζ, which would delay the start of the interaction between the lower-tropospheric DRW and the upper-tropospheric shortwave, and yet still result in a stronger NV19 storm (Fig. 4.8b,Fig. 4.11b).

Twenty-four hours later, at 0000 UTC 27 November 2019, the maximum ensemble mean CVA by $\vec{V}_T$ was located where the NV19 storm made landfall near Crescent City, CA (Fig. 4.11d). Ensemble mean MSLP in the region of interest decreased more than 2.4 hPa with a $+1$ standard deviation increase in CVA by $\vec{V}_T$ to the north of the cyclone center (Fig. 4.11d). The top five strongest ensemble members forecasted increased CVA by $\vec{V}_T$ nearly +1 standard deviation to the northwest and over the cyclone whereas the top five weakest ensemble members forecasted decreased CVA by $\vec{V}_T$ greater than −1 standard deviation to the north of the cyclone (Fig. 4.11e,f). The sensitivity pattern highlighting a decrease in MSLP with an increase in CVA by $\vec{V}_T$ to the north and over the cyclone (Fig. 4.11d) is potentially a reflection of the strongest ensemble member forecasts portraying a westward shifted 500 hPa shortwave (Fig. 4.8d), which would focus CVA by $\vec{V}_T$ directly over the surface cyclone at this time, and imply a slower propagation speed as the forecasted NV19 storm at 0000 UTC 27 November 2019 would be shifted to the north and west (Fig. 4.1,Fig. 4.11d).

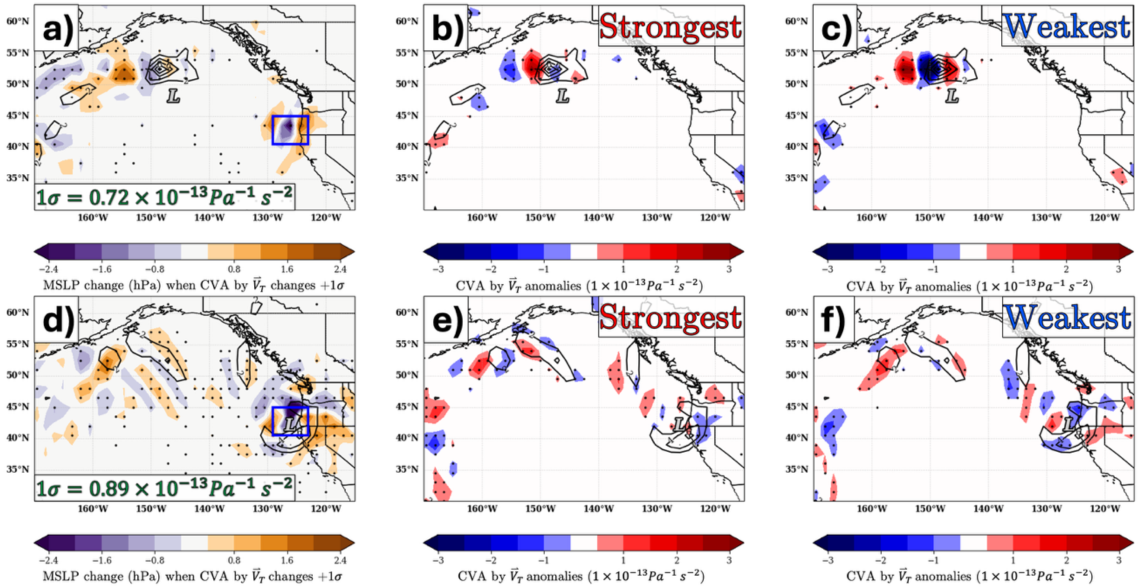

Fig. 4.11. (a) Sensitivity pattern between ensemble member 500 hPa cyclonic vorticity advection by the 300-700 hPa thermal wind (hereafter referred to as CVA by $\vec{V}_T$) forecasts at 0000 UTC 26 November 2019 and ensemble MSLP within the blue box 24 hours later at 0000 UTC 27 November 2019. Colorfill as in Fig. 4.8a but for a 1 standard deviation increase in CVA by $\vec{V}_T$. Ensemble member mean CVA by $\vec{V}_T$ contoured in black every $2 \times 10^{-13}\ \frac{1}{s^2}$ starting at $2\ \times 10^{-13}\ \frac{1}{s^2}$. Magnitude of 1 standard deviation of CVA by $\vec{V}_T$ in bottom left corner. Stippling represents statistical significance at the 95% confidence interval. Gray "L" denotes location of NV19 storm MSLP minimum at 0000 UTC 26 November 2019. (b) Ensemble member mean and anomalies of CVA by $\vec{V}_T$ at 0000 UTC 26 November 2019 averaged across the top five lowest

ensemble member MSLP forecasts as in Fig. 4.2. CVA by $\vec{V}_T$ anomalies shaded every $0.5 \times 10^{-13} \frac{1}{s^2}$ with positive anomalies shaded in red and negative anomalies shaded in blue. Ensemble member mean CVA by $\vec{V}_T$ as in (a). Stippling as in (a). Gray “L” as in (a). (c) Ensemble member mean and anomalies of CVA by $\vec{V}_T$ at 0000 UTC 26 November 2019 averaged across the top five highest ensemble member MSLP forecasts as in Fig. 4.2. Ensemble member CVA by $\vec{V}_T$ mean and anomalies shaded as in (b). Stippling as in (b). Gray “L” as in (b). (d) Sensitivity pattern between ensemble member CVA by $\vec{V}_T$ forecasts at 0000 UTC 27 November 2019 and ensemble MSLP within the blue box at 0000 UTC 27 November 2019. Colorfill as in (a). Ensemble member mean CVA by $\vec{V}_T$ contoured as in (a). Stippling as in (a). (e) As in (b) but for 0000 UTC 27 November 2019. (f) As in (c) but for 0000 UTC 27 November 2019.

4.5. Conclusions and Discussion

Ensemble-based sensitivity analysis (ESA) performed on the ECMWF IFS ensemble suite revealed variations in the sensitivity of MSLP forecasts off the California-Oregon coast at 0000 UTC 27 November 2019 to variables previously identified as integral in the development of the NV19 cyclone. ECMWF IFS ensemble member forecasts were quantified in terms of the top five strongest and weakest ensemble members based on their forecasts of MSLP of the NV19 storm at 0000 UTC 27 November 2019. Ensemble member anomalies of the different variables averaged across these top five strongest and top five weakest ensemble members were then compared and physical reasons for the differences in strength of NV19 MSLP forecasts were suggested.

During the initial stages of cyclogenesis, at 0000 UTC 26 November 2019, the top five strongest ensemble member forecasts featured: stronger 850 hPa $\mathfrak{I}$ to the east of the cyclone (Fig. 4.6b), a westward-displaced 500 hPa shortwave trough to the northwest of the cyclone (Fig. 4.8b), and a westward shifted region of CVA by $\vec{V}_T$ also to the northwest of the cyclone (Fig. 4.11b). PV anomalies at 925 hPa between the top five strongest and top five weakest ensemble member forecasts were remarkably similar (Fig. 4.7b,c). During the final stages of cyclogenesis, at 0000 UTC 27 November 2019, the top five strongest ensemble member forecasts featured: a northward-shifted and expanded region of 850 hPa $\mathfrak{I}$ to the east of the cyclone (Fig. 4.6e), a stronger 925 hPa PV anomaly to the northwest of the cyclone (Fig.

4.7e), a westward-displaced 500 hPa large-scale trough over the cyclone (Fig. 4.8e), and a northwestward shifted region of CVA by $\vec{V}_T$ also over the cyclone (Fig. 4.11e).

The comparison between ensemble members in terms of their forecasted intensity of MSLP off the California-Oregon coast at 0000 UTC 27 November 2019 illuminated that the ensemble members portraying a stronger NV19 storm forecasted a lower-tropospheric DRW shifted further to the east and an upper-tropospheric trough shifted further to the west, thereby increasing their relative distance. Consequently, the stronger ensemble members forecasted a delay to the period of interaction between the lower-tropospheric DRW and the upper-tropospheric trough. Delaying this interaction would allow the lower-tropospheric DRW to continue lower-tropospheric PV generation through persistent latent heat release and development into a more substantial lower-tropospheric vortex. The westward-shifted upper-tropospheric trough would then move in proximity to the stronger lower-tropospheric DRW after its period of additional strengthening and would stretch the more vorticity-rich air through forcing column mass divergence and synoptic-scale ascent. Therefore, when these two features eventually vertically-collocate, the mutual amplification and forcing for surface cyclogenesis would be more robust than if this interaction had occurred earlier when the two features, particularly the lower-tropospheric DRW, were weaker. There was also an indication that the NV19 storm propagation speed was slower in the strongest ensemble member forecasts (Fig. 4.1), meaning that the delay in interaction between the lower-tropospheric DRW and the upper-tropospheric trough in the stronger forecasts was partially compensated by slower onshore movement and a lagged duration of lower-tropospheric and upper-tropospheric interaction. The importance of the timing of mutual amplification was also stressed in previous studies on explosive DRW cyclogenesis events (Wernli et al. 2002; Moore et al. 2008; Rivière et al. 2010; Boettcher and Wernli 2011, 2013; McKenzie 2014; Tamarin and Kaspi 2016; Zhang and Wang 2018).

In expanding the utility of ESA, one could also use the results of the ESA to anticipate potential forecast errors when considering rapid DRW cyclogenesis events. The sensitivity patterns to variables such as lower-tropospheric frontogenesis, lower-tropospheric PV, mid-tropospheric vorticity, and CVA by

$\vec{V}_T$ all showed between a 0.8 hPa and greater than 2.4 hPa change in MSLP depending on location and strength of ensemble member anomalies. Twenty-four hour surface forecasts of the NV19 storm from the Ocean Prediction Center were around 3 hPa higher than the central MSLP of the actual NV19 storm for two consecutive forecasts valid at 0000 UTC 27 November and 1200 UTC 27 November 2019. A forecaster could theoretically identify differences between ensemble member forecasts of rapid DRW cyclogenesis events with the knowledge of typical sensitivity patterns for these types of developments and identify the most accurate ensemble member forecasts, since the forecast error for the NV19 rapid DRW cyclogenesis event was around the same magnitude as the maximum MSLP change identified using ESA. The addition of sensitivity patterns identified through ESA when considering rapid DRW cyclogenesis events allows for the improvement of forecasts of these events at longer lead times greater than twelve hours and could be an avenue for future real-time correction of forecast biases.

5. Future Work

The comprehensive analysis of the November 2019 (NV19) rapid cyclogenesis event revealed intricacies of this specific development which were unusual both in terms of the environment in which the cyclone developed and in reference to previous investigations into diabatic Rossby wave and upper-level jet/front system mutual amplifications. An intriguing question remains after the investigation into this development: was the NV19 storm the strongest it could have possibly been? The storm is the strongest cyclone to make landfall on the California-Oregon coast since records began and the set of ingredients conspiring to result in its genesis and intensification were primed for explosive development.

In Section 4.5, it was noted that ensemble member forecasts which delayed the interaction between the lower-tropospheric diabatic Rossby wave and the upper-tropospheric trough tied to the upper-level jet/front system still produced a forecast of the NV19 storm up to 23 hPa stronger than weaker NV19 storm ensemble member forecasts. One avenue of investigation into the ceiling of NV19 storm strength could be the utilization of iterated, optimal perturbation analysis, whereby the adjoint model is used to estimate the sensitivity of a final forecast state to perturbations to the initial state (Brett Hoover, personal communication). These perturbations to the initialized model state associated with the most sensitivity at the final forecast state are then iteratively optimized for enhancing storm intensity at the final forecast state. The ceiling of the NV19 storm could be investigated using iterated, optimal perturbation analysis by seeding the initial model state with the most ideal conditions for rapid intensification and then running a simulation of the storm forward in time. This most optimal simulation of the NV19 storm could be compared to the actual NV19 storm to see how much stronger the NV19 storm could have been, assuming it was not already the strongest possible version of itself. Iterated, optimal perturbation analysis by Brett Hoover and collaborators is ongoing as of publishing of this dissertation.

In Section 2.4.4, it was suggested that the Blob 2.0 MHW (e.g. Amaya et al. 2020; Chen et al. 2021), which first reached peak intensity in November 2019, had indirect impacts on the NV19 storm development. Sensible sea surface heat fluxes were anomalously low following the storm track across the northeast Pacific basin during storm evolution. However, the prolonged and intense Blob 2.0 MHW, which was confined to the upper ocean, could have continuously fluxed heat into the lower troposphere during the summer and fall leading up to NV19 storm cyclogenesis event, which would have led to increased background lower-tropospheric baroclinicity. Simulations of the NV19 development could be run using the Weather Research and Forecasting (WRF) model (Skamarock et al. 2019) to test this potential influence on background baroclinicity. One simulation with control inputs from the hourly ERA5 data could be compared to simulations which feature increasingly reduced initial lower-tropospheric baroclinicity to evaluate any potential impacts of the Blob 2.0 MHW on the background thermal field. It is anticipated that a reduction in the initial lower-tropospheric baroclinicity would reduce the intensity of the differential lower-tropospheric frontogenesis and subsequent latent heat release, which spawned the DRW, thereby reducing the strength of the lower-tropospheric vortex and leading to a weakened NV19 storm.

Furthermore, to expand upon the applicability of the conclusions drawn from the analysis of the NV19 storm, a plethora of cases involving a similar type of cyclogenesis in unusual environments characterized by cold sea surface temperatures must be explored. One candidate for further investigation is a rapid cyclogenesis event which occurred in the latter-half of November 2024 also in the northeast Pacific basin much like the November 2019 rapid cyclogenesis event. The November 2024 event, which resulted in an impressive 945 hPa cyclone situated off the Washington, USA and British Columbia coastline, displayed striking dynamical similarities, including a similar structural evolution and extremely rapid rate of intensification. Both the November 2019 and the November 2024 storm originated as innocuous-looking warm frontal waves, perhaps both as DRWs. Intense and geographically restricted lower-tropospheric frontogenesis produced heavy precipitation which, in turn, generated lower-tropospheric positive potential vorticity anomalies along the front. These anomalies orchestrated a period of modest growth before both cyclones were overtaken by potent tropopause-level disturbances which facilitated ascent and the stretching of vorticity-rich air that drove the rapid cyclogenesis. Investigation into the November 2024 development is ongoing as of publishing of this dissertation, with the goal of investigating more of these types of development with tools refined within this dissertation.

As analyses of diabatic Rossby waves continue to become increasingly crucial, the 10-year climatology of Northern Hemispheric diabatic Rossby waves presented in Boettcher and Wernli (2013) can be extended to longer time periods such as 30 or 40 years. This longer climatology could be used to track changes in frequency, intensity, and geographic location of diabatic Rossby waves in consecutive 10- or 20-year periods of time across the Northen Hemisphere. Events such as the November 2019 and the November 2024 bomb cyclones would be included in the updated climatology as well. A more comprehensive climatology could then be constructed to complement the climatology in Boettcher and Wernli (2013), while potentially adding insight into the distribution of diabatic Rossby waves, and their changes over time, over the Northern Hemisphere. The climatology of diabatic Rossby waves over the Southern Hemisphere presented in Boettcher and Wernli (2015) could also be similarly expanded.

Finally, the ability to run simulations of weather systems under the influence of future climate scenarios provides the best guess as to the dynamics of diabatic Rossby waves in the future under a warming climate. A large-scale climate model like the Community Earth System Model (CESM; Kay et al. 2015) is a large ensemble model of Earth's climate under different scenarios of projected climate warming. The CESM could be used to explore future climates over regions of Earth where rapid diabatic Rossby wave developments are frequent as identified in Boettcher and Wernli (2013) and Boettcher and Wernli (2015). The effects of a warming climate on future diabatic Rossby wave frequency, intensity, and geographic location could then be considered using comparisons between catalogs of past diabatic Rossby waves and catalogs of future diabatic Rossby waves simulated using the CESM. Simulating diabatic Rossby wave evolutions utilizing output from the CESM would allow for the propagation of diabatic Rossby wave research into the future.

6. Data availability statement

The fifth generation ECMWF atmospheric reanalysis dataset (ERA5) is produced by the Copernicus Climate Change Service (C3S) at ECMWF and can be accessed via http://cds.climate.copernicus.eu/datasets/reanalysis-era5-pressure-levels?tab=overview. The ECMWF IFS ensemble suite is also produced by the C3S at ECMWF and can be accessed via the above link as well. Satellite imagery is produced by the National Centers for Environmental Information at NOAA and can be accessed via https://www.ncei.noaa.gov/access. Data used to make in Fig. 2.8 was adapted from Roebber (1984), Wang and Rogers (2001), and Zhang et al. (2017). All computer programs written to perform the data analysis are available from the author upon request.

7. References

Ahmadi-Givi, F., G. C. Graig, and R. S. Plant, 2004: The dynamics of a midlatitude cyclone with very strong latent-heat release. *Quart J Royal Meteoro Soc*, **130**, 295–323, https://doi.org/10.1256/qj.02.226.

Amaya, D. J., A. J. Miller, S.-P. Xie, and Y. Kosaka, 2020: Physical drivers of the summer 2019 North Pacific marine heatwave. *Nature communications*, **11**, 1903.

Ancell, B., and G. J. Hakim, 2007: Comparing adjoint-and ensemble-sensitivity analysis with applications to observation targeting. *Monthly Weather Review*, **135**, 4117–4134.

Barnes, S. L., F. Caracena, and A. Marroquin, 1996: Extracting synoptic-scale diagnostic information from mesoscale models: The Eta model, gravity waves, and quasigeostrophic diagnostics. *Bulletin of the American Meteorological Society*, **77**, 519–528.

Beaty, P. T., J. E. Martin, A. C. Winters, and G. M. Lackmann, 2025: An Unusual Case of Rapid Cyclogenesis in the northeast Pacific Basin. Overview and Piecewise PV Inversion. *Monthly Weather Review*, **154**, https://doi.org/10.1175/MWR-D-24-0198.1.

Bednarczyk, C. N., and B. C. Ancell, 2015: Ensemble sensitivity analysis applied to a southern plains convective event. *Monthly Weather Review*, **143**, 230–249.

Bell, G. D., and D. Keyser, 1993: Shear and Curvature vorticity and Potential-Vorticity Interchanges: Interpretation and Application to a Cutoff Cyclone Event. *Mon. Wea. Rev.*, **121**, 76–102, https://doi.org/10.1175/1520-0493(1993)121<0076:SACVAP>2.0.CO;2.

Bjerknes, J., and H. Solberg, 1922: Life cycle of cyclones and the polar front theory of atmospheric circulation. *Geofys. Publ.*, **3**, 1–18.

Boettcher, M., and H. Wernli, 2011: Life cycle study of a diabatic Rossby wave as a precursor to rapid cyclogenesis in the North Atlantic—Dynamics and forecast performance. *Monthly Weather Review*, **139**, 1861–1878.

——, and ——, 2013: A 10-yr climatology of diabatic Rossby waves in the Northern Hemisphere. *Monthly weather review*, **141**, 1139–1154.

——, and ——, 2015: Diabatic Rossby waves in the southern hemisphere. *Quarterly Journal of the Royal Meteorological Society*, **141**, 3106–3117.

Bosart, L. F., 1981: The Presidents' Day snowstorm of 18–19 February 1979: A subsynoptic-scale event. *Monthly Weather Review*, **109**, 1542–1566.

Bracegirdle, T. J., and S. L. Gray, 2009: The dynamics of a polar low assessed using potential vorticity inversion. *Quart J Royal Meteoro Soc*, **135**, 880–893, https://doi.org/10.1002/qj.411.

Bretherton, F. P., 1966: Critical layer instability in baroclinic flows. *Quarterly Journal of the Royal Meteorological Society*, **92**, 325–334.

Chang, E. K., M. Zheng, and K. Raeder, 2013: Medium-range ensemble sensitivity analysis of two extreme Pacific extratropical cyclones. *Monthly weather review*, **141**, 211–231.

Charney, J., 1955: The Use of the Primitive Equations of Motion in Numerical Prediction. *Tellus*, **7**, 22–26, https://doi.org/10.1111/j.2153-3490.1955.tb01138.x.

Chen, Z., J. Shi, Q. Liu, H. Chen, and C. Li, 2021: A persistent and intense marine heatwave in the Northeast Pacific during 2019–2020. *Geophysical Research Letters*, **48**, e2021GL093239.

Davis, C. A., 1992: Piecewise potential vorticity inversion. *Journal of the atmospheric sciences*, **49**, 1397–1411.

——, and K. A. Emanuel, 1988: Observational evidence for the influence of surface heat fluxes on rapid maritime cyclogenesis. *Monthly Weather Review*, **116**, 2649–2659.

——, and ——, 1991: Potential vorticity diagnostics of cyclogenesis. *Monthly weather review*, **119**, 1929–1953.

Davis, C. A., E. D. Grell, and M. A. Shapiro, 1996: The Balanced Dynamical Nature of a Rapidly Intensifying Oceanic Cyclone. *Mon. Wea. Rev.*, **124**, 3–26, https://doi.org/10.1175/1520-0493(1996)124<0003:TBDNOA>2.0.CO;2.

Dickinson, M. J., L. F. Bosart, W. E. Bracken, G. J. Hakim, D. M. Schultz, M. A. Bedrick, and K. R. Tyle, 1997: The March 1993 Superstorm cyclogenesis: Incipient phase synoptic-and convective-scale flow interaction and model performance. *Monthly weather review*, **125**, 3041–3072.

ECMWF, 2024: IFS Documentation CY49R1 - Part V: Ensemble Prediction System, https://doi.org/10.21957/956D60AD81.

Eliassen, A., 1962: On the vertical circulation in frontal zones. *Geofys. publ*, **24**, 147–160.

Ertel, H., 1942: Ein neuer hydrodynamischer wirbelsatz. *Meteorologische Zeitschrift*, **59**, 271–281.

Fu, S., J. Sun, and J. Sun, 2014: Accelerating two-stage explosive development of an extratropical cyclone over the northwestern Pacific Ocean: A piecewise potential vorticity diagnosis. *Tellus A: Dynamic Meteorology and Oceanography*, **66**, 23210.

Garcies, L., and V. Homar, 2009: Ensemble sensitivities of the real atmosphere: application to Mediterranean intense cyclones. *Tellus A: Dynamic Meteorology and Oceanography*, **61**, 394–406.

——, and ——, 2010: An optimized ensemble sensitivity climatology of Mediterranean intense cyclones. *Natural Hazards and Earth System Sciences*, **10**, 2441–2450.

Gyakum, J. R., 1983a: On the evolution of the QE II storm. I: Synoptic aspects. *Monthly weather review*, **111**, 1137–1155.

——, 1983b: On the evolution of the QE II storm. II: Dynamic and thermodynamic structure. *Monthly weather review*, **111**, 1156–1173.

——, and R. E. Danielson, 2000: Analysis of meteorological precursors to ordinary and explosive cyclogenesis in the western North Pacific. *Monthly Weather Review*, **128**, 851–863.

——, P. J. Roebber, and Timothy A Bullock, 1992: The role of antecedent surface vorticity development as a conditioning process in explosive cyclone intensification. *Monthly weather review*, **120**, 1465–1489.

Hakim, G. J., and R. D. Torn, 2008: Ensemble synoptic analysis. *Meteorological Monographs*, **33**, 147–162.

Heo, K.-Y., Y.-W. Seo, K.-J. Ha, K.-S. Park, J. Kim, J.-W. Choi, K. Jun, and J.-Y. Jeong, 2015: Development mechanisms of an explosive cyclone over East Sea on 3–4 April 2012. *Dynamics of Atmospheres and Oceans*, **70**, 30–46.

——, K.-J. Ha, and T. Ha, 2019: Explosive Cyclogenesis around the Korean Peninsula in May 2016 from a potential vorticity perspective: case study and numerical simulations. *Atmosphere*, **10**, 322.

Hersbach, H., and Coauthors, 2020: The ERA5 global reanalysis. *Quart J Royal Meteoro Soc*, **146**, 1999–2049, https://doi.org/10.1002/qj.3803.

Hill, A. J., C. C. Weiss, and B. C. Ancell, 2016: Ensemble sensitivity analysis for mesoscale forecasts of dryline convection initiation. *Monthly Weather Review*, **144**, 4161–4182.

Holton, J. R., and G. J. Hakim, 2013: *An introduction to dynamic meteorology.* Academic press.

Hoover, B. T., 2015: Identifying a barotropic growth mechanism in east Pacific tropical cyclogenesis using adjoint-derived sensitivity gradients. *Journal of the Atmospheric Sciences*, **72**, 1215–1234.

Hoskins, B. J., I. Draghici, and H. Davies, 1978: A new look at the ω-equation. *Quarterly Journal of the Royal Meteorological Society*, **104**, 31–38.

——, M. E. McIntyre, and A. W. Robertson, 1985: On the use and significance of isentropic potential vorticity maps. *Quarterly Journal of the Royal Meteorological Society*, **111**, 877–946.

Hu, C.-C., and C.-C. Wu, 2020: Ensemble sensitivity analysis of tropical cyclone intensification rate during the development stage. *Journal of the Atmospheric Sciences*, **77**, 3387–3405.

Hultquist, T. R., M. R. Dutter, and D. J. Schwab, 2006: Reexamination of the 9–10 November 1975 "Edmund Fitzgerald" storm using today's technology. *Bulletin of the American Meteorological Society*, **87**, 607–622.

Huo, Z., D.-L. Zhang, and J. R. Gyakum, 1999: Interaction of potential vorticity anomalies in extratropical cyclogenesis. Part I: Static piecewise inversion. *Monthly weather review*, **127**, 2546–2562.

Iizuka, S., M. Shiota, R. Kawamura, and H. Hatsushika, 2013: Influence of the monsoon variability and sea surface temperature front on the explosive cyclone activity in the vicinity of Japan during northern winter. *SOLA*, **9**, 1–4.

Ito, K., and C.-C. Wu, 2013: Typhoon-position-oriented sensitivity analysis. Part I: Theory and verification. *Journal of the atmospheric sciences*, **70**, 2525–2546.

Iwao, K., M. Inatsu, and M. Kimoto, 2012: Recent changes in explosively developing extratropical cyclones over the winter northwestern Pacific. *Journal of Climate*, **25**, 7282–7296.

Kay, J. E., and Coauthors, 2015: The Community Earth System Model (CESM) large ensemble project: A community resource for studying climate change in the presence of internal climate variability. *Bulletin of the American Meteorological Society*, **96**, 1333–1349.

Keyser, D., and M. A. Shapiro, 1986: A Review of the Structure and Dynamics of Upper-Level Frontal Zones. *Mon. Wea. Rev.*, **114**, 452–499, https://doi.org/10.1175/1520-0493(1986)114<0452:AROTSA>2.0.CO;2.

Kohl, M., and P. A. O'Gorman, 2022: The Diabatic Rossby Vortex: Growth Rate, Length Scale and the Wave-Vortex Transition. *Journal of the Atmospheric Sciences*.

Korner, S. O., and J. E. Martin, 2000: Piecewise frontogenesis from a potential vorticity perspective: Methodology and a case study. *Monthly Weather Review*, **128**, 1266–1288.

Kouroutzoglou, J., H. Flocas, M. Hatzaki, K. Keay, I. Simmonds, and A. Mavroudis, 2015: On the dynamics of a case study of explosive cyclogenesis in the Mediterranean. *Meteorology and Atmospheric Physics*, **127**, 49–73.

Kuo, Y.-H., S. Low-Nam, and R. J. Reed, 1991: Effects of surface energy fluxes during the early development and rapid intensification stages of seven explosive cyclones in the western Atlantic. *Monthly Weather Review*, **119**, 457–476.

Lackmann, G. M., D. Keyser, and L. F. Bosart, 1997: A Characteristic Life Cycle of Upper-Tropospheric Cyclogenetic Precursors during the Experiment on Rapidly Intensifying Cyclones over the Atlantic (ERICA). *Mon. Wea. Rev.*, **125**, 2729–2758, https://doi.org/10.1175/1520-0493(1997)125<2729:ACLCOU>2.0.CO;2.

Lagouvardos, K., V. Kotroni, and E. Defer, 2007: The 21–22 January 2004 explosive cyclogenesis over the Aegean Sea: Observations and model analysis. *Quarterly Journal of the Royal Meteorological Society: A journal of the atmospheric sciences, applied meteorology and physical oceanography*, **133**, 1519–1531.

Lang, A. A., and J. E. Martin, 2012: The structure and evolution of lower stratospheric frontal zones. Part 1: Examples in northwesterly and southwesterly flow. *Quarterly Journal of the Royal Meteorological Society*, **138**, 1350–1365.

Langland, R. H., R. L. Elsberry, and R. M. Errico, 1995: Evaluation of physical processes in an idealized extratropical cyclone using adjoint sensitivity. *Quarterly Journal of the Royal Meteorological Society*, **121**, 1349–1386.

Lim, E.-P., and I. Simmonds, 2002: Explosive cyclone development in the Southern Hemisphere and a comparison with Northern Hemisphere events. *Monthly Weather Review*, **130**, 2188–2209.

Limpert, G. L., and A. L. Houston, 2018: Ensemble sensitivity analysis for targeted observations of supercell thunderstorms. *Monthly Weather Review*, **146**, 1705–1721.

Liu, L., J. Feng, L. Ma, Y. Yang, X. Wu, and C. Wang, 2024: Ensemble-based sensitivity analysis of track forecasts of typhoon In-fa (2021) without and with model errors in the ECMWF, NCEP, and CMA ensemble prediction systems. *Atmospheric Research*, **309**, 107596.

Lynott, R. E., and O. P. Cramer, 1966: Detailed analysis of the 1962 Columbus Day windstorm in Oregon and Washington. *Monthly Weather Review*, **94**, 105–117.

Martin, J. E., 1998: The Structure and Evolution of a Continental Winter Cyclone. Part I: Frontal Structure and the Occlusion Process. *Mon. Wea. Rev.*, **126**, 303–328, https://doi.org/10.1175/1520-0493(1998)126<0303:TSAEOA>2.0.CO;2.

Martin, J. E., 1999: Quasigeostrophic forcing of ascent in the occluded sector of cyclones and the trowal airstream. *Monthly weather review*, **127**, 70–88.

——, 2006: *Mid-latitude atmospheric dynamics: a first course*. John Wiley & Sons.

——, 2014: Quasi-geostrophic diagnosis of the influence of vorticity advection on the development of upper level jet-front systems. *Quarterly Journal of the Royal Meteorological Society*, **140**, 2658–2671.

——, and J. A. Otkin, 2004: The rapid growth and decay of an extratropical cyclone over the central Pacific Ocean. *Weather and forecasting*, **19**, 358–376.

McKenzie, M. W., 2014: *An analysis of numerical weather prediction of the diabatic Rossby Vortex*. NAVAL POSTGRADUATE SCHOOL MONTEREY CA.

McMurdie, L. A., and B. Ancell, 2014: Predictability characteristics of landfalling cyclones along the North American west coast. *Monthly Weather Review*, **142**, 301–319.

Moore, R. W., and M. T. Montgomery, 2004: Reexamining the dynamics of short-scale, diabatic Rossby waves and their role in midlatitude moist cyclogenesis. *Journal of the atmospheric sciences*, **61**, 754–768.

——, and ——, 2005: Analysis of an idealized, three-dimensional diabatic Rossby vortex: A coherent structure of the moist baroclinic atmosphere. *Journal of the atmospheric sciences*, **62**, 2703–2725.

——, ——, and H. C. Davies, 2008: The integral role of a diabatic Rossby vortex in a heavy snowfall event. *Monthly weather review*, **136**, 1878–1897.

Morgan, M. C., and J. W. Nielsen-Gammon, 1998: Using tropopause maps to diagnose midlatitude weather systems. *Monthly weather review*, **126**, 2555–2579.

Newton, C. W., 1954: Frontogenesis and frontolysis as a three-dimensional process. *Journal of Atmospheric Sciences*, **11**, 449–461.

NOAA National Centers for Environmental Information, 2019: *Monthly National Climate Report for November 2019*, accessed 22 July 2025, https://www.ncei.noaa.gov/access/monitoring/monthly-report/national/201911.

Odell, L., P. Knippertz, S. Pickering, B. Parkes, and A. Roberts, 2013: The Braer storm revisited. *Weather*, **68**, 105–111.

Parker, D. J., and A. J. Thorpe, 1995: Conditional convective heating in a baroclinic atmosphere: A model of convective frontogenesis. *Journal of the atmospheric sciences*, **52**, 1699–1711.

Plant, R., G. C. Craig, and S. Gray, 2003: On a threefold classification of extratropical cyclogenesis. *Quarterly Journal of the Royal Meteorological Society: A journal of the atmospheric sciences, applied meteorology and physical oceanography*, **129**, 2989–3012.

Quandt, L.-A., J. H. Keller, O. Martius, J. G. Pinto, and S. C. Jones, 2019: Ensemble sensitivity analysis of the blocking system over Russia in summer 2010. *Monthly Weather Review*, **147**, 657–675.

R. B. Weldon, 1979: Cloud patterns and the upper air wind field, Part IV. National Weather Service Satellite training note.

Raymond, D., and H. Jiang, 1990: A theory for long-lived mesoscale convective systems. *Journal of Atmospheric Sciences*, **47**, 3067–3077.

Reed, R. J., 1955: A study of a characteristic tpye of upper-level frontogenesis. *Journal of Atmospheric Sciences*, **12**, 226–237.

——, and F. Sanders, 1953: An investigation of the development of a mid-tropospheric frontal zone and its associated vorticity field. *Journal of Atmospheric Sciences*, **10**, 338–349.

——, and E. F. Danielsen, 1958: Fronts in the vicinity of the tropopause. *Archiv für Meteorologie, Geophysik und Bioklimatologie, Ser. A, Meteorologie und Geophysik*, **11**, 1–17.

——, and M. D. Albright, 1986: A case study of explosive cyclogenesis in the eastern Pacific. *Monthly Weather Review*, **114**, 2297–2319.

Ren, S., L. Lei, Z.-M. Tan, and Y. Zhang, 2019: Multivariate ensemble sensitivity analysis for Super Typhoon Haiyan (2013). *Monthly Weather Review*, **147**, 3467–3480.

Revell, M. J., and R. M. Gorman, 2003: The "Wahine storm": Evaluation of a numerical forecast of a severe wind and wave event for the New Zealand coast. *New Zealand Journal of Marine and Freshwater Research*, **37**, 251–266.

Rivière, G., P. Arbogast, K. Maynard, and A. Joly, 2010: The essential ingredients leading to the explosive growth stage of the European wind storm Lothar of Christmas 1999. *Quarterly Journal of the Royal Meteorological Society: A journal of the atmospheric sciences, applied meteorology and physical oceanography*, **136**, 638–652.

Roebber, P. J., 1984: Statistical analysis and updated climatology of explosive cyclones. *Monthly Weather Review*, **112**, 1577–1589.

——, 1989: The role of surface heat and moisture fluxes associated with large-scale ocean current meanders in maritime cyclogenesis. *Monthly weather review*, **117**, 1676–1694.

——, 1993: A diagnostic case study of self-development as an antecedent conditioning process in explosive cyclogenesis. *Monthly weather review*, **121**, 976–1006.

Rossby, C.-G., 1939: Relation between variations in the intensity of the zonal circulation of the atmosphere and the displacements of the semi-permanent centers of action. *J. mar. Res.*, **2**, 38–55.

——, 1940a: Planetary flow pattern in the atmosphere. Quart. *J. Roy. Meteor. Soc.*, **66**, 68–87.

Rossby, C.-G., 1940b: Planetary flow patterns in the atmosphere. *Quarterly Journal of the Royal Meteorological Society*, **66**, 68–87.

Rotunno, R., W. C. Skamarock, and C. Snyder, 1994: An analysis of frontogenesis in numerical simulations of baroclinic waves. *Journal of Atmospheric Sciences*, **51**, 3373–3398.

Sanders, F., 1986: Explosive cyclogenesis in the west-central North Atlantic Ocean, 1981–84. Part I: Composite structure and mean behavior. *Monthly weather review*, **114**, 1781–1794.

——, and J. R. Gyakum, 1980: Synoptic-dynamic climatology of the "bomb". *Monthly Weather Review*, **108**, 1589–1606.

Shapiro, M. A., 1981: Frontogenesis and Geostrophically Forced Secondary Circulations in the Vicinity of Jet Stream-Frontal Zone Systems. *J. Atmos. Sci.*, **38**, 954–973, https://doi.org/10.1175/1520-0469(1981)038<0954:FAGFSC>2.0.CO;2.

——, 1983: Mesoscale weather systems of the central United States. The national STORM program: Scientific and technological bases and major objectives. UCAR Rep. *Cooperative Institute for Research in Environmental Sciences*, **78**.

Skamarock, W. C., and Coauthors, 2019: A description of the advanced research WRF model version 4. *National Center for Atmospheric Research: Boulder, CO, USA*, **145**, 145.

Smith, N. H., and B. C. Ancell, 2017: Ensemble sensitivity analysis of wind ramp events with applications to observation targeting. *Monthly Weather Review*, **145**, 2505–2522.

Snyder, C., and R. S. Lindzen, 1991: Quasi-geostrophic wave-CISK in an unbounded baroclinic shear. *Journal of Atmospheric Sciences*, **48**, 76–86.

Squires, M. F., J. H. Lawrimore, R. R. Heim Jr, D. A. Robinson, M. R. Gerbush, and T. W. Estilow, 2014: The regional snowfall index. *Bulletin of the American Meteorological Society*, **95**, 1835–1848.

Suri, D., S. Keates, and M. Sidaway, 2025: Storm Éowyn, 24 January 2025. *Weather*.

Sutcliffe, R., 1947: A contribution to the problem of development. *Quarterly Journal of the Royal Meteorological Society*, **73**, 370–383.

Tamarin, T., and Y. Kaspi, 2016: The poleward motion of extratropical cyclones from a potential vorticity tendency analysis. *Journal of the Atmospheric Sciences*, **73**, 1687–1707.

Terpstra, A., T. Spengler, and R. W. Moore, 2015: Idealised simulations of polar low development in an Arctic moist-baroclinic environment. *Quarterly Journal of the Royal Meteorological Society*, **141**, 1987–1996.

Torn, R. D., 2010: Ensemble-based sensitivity analysis applied to African easterly waves. *Weather and forecasting*, **25**, 61–78.

——, 2014: The impact of targeted dropwindsonde observations on tropical cyclone intensity forecasts of four weak systems during PREDICT. *Monthly Weather Review*, **142**, 2860–2878.

——, and G. J. Hakim, 2008: Ensemble-based sensitivity analysis. *Monthly Weather Review*, **136**, 663–677.

——, and D. Cook, 2013: The role of vortex and environment errors in genesis forecasts of Hurricanes Danielle and Karl (2010). *Monthly weather review*, **141**, 232–251.

——, and G. S. Romine, 2015: Sensitivity of central Oklahoma convection forecasts to upstream potential vorticity anomalies during two strongly forced cases during MPEX. *Monthly Weather Review*, **143**, 4064–4087.

Trenberth, K. E., 1978: On the interpretation of the diagnostic quasi-geostrophic omega equation. *Monthly Weather Review*, **106**, 131.

Uccellini, L. W., 1986: The possible influence of upstream upper-level baroclinic processes on the development of the QE II storm. *Monthly weather review*, **114**, 1019–1027.

——, D. Keyser, K. F. Brill, and C. H. Wash, 1985: The Presidents' Day cyclone of 18–19 February 1979: Influence of upstream trough amplification and associated tropopause folding on rapid cyclogenesis. *Monthly Weather Review*, **113**, 962–988.

Wang, C.-C., and J. C. Rogers, 2001: A composite study of explosive cyclogenesis in different sectors of the North Atlantic. Part I: Cyclone structure and evolution. *Monthly Weather Review*, **129**, 1481–1499.

——, M.-S. Li, C.-S. Chang, P.-Y. Chuang, S.-H. Chen, and K. Tsuboki, 2021: Ensemble-based sensitivity analysis and predictability of an extreme rainfall event over northern Taiwan in the Mei-Yu season: The 2 June 2017 case. *Atmospheric Research*, **259**, 105684.

Wernli, H., S. Dirren, M. A. Liniger, and M. Zillig, 2002: Dynamical aspects of the life cycle of the winter storm 'Lothar'(24–26 December 1999). *Quarterly Journal of the Royal Meteorological Society: A journal of the atmospheric sciences, applied meteorology and physical oceanography*, **128**, 405–429.

Whitaker, J. S., L. W. Uccellini, and K. F. Brill, 1988: A model-based diagnostic study of the rapid development phase of the Presidents's Day cyclone. *Monthly weather review*, **116**, 2337–2365.

Winters, A. C., and J. E. Martin, 2017a: Diagnosis of a North American polar–subtropical jet superposition employing piecewise potential vorticity inversion. *Monthly Weather Review*, **145**, 1853–1873.

——, and ——, 2017b: Diagnosis of a North American polar–subtropical jet superposition employing piecewise potential vorticity inversion. *Monthly Weather Review*, **145**, 1853–1873.

——, D. Keyser, and L. F. Bosart, 2020: Composite vertical-motion patterns near North American polar–subtropical jet superposition events. *Monthly Weather Review*, **148**, 4565–4585.

Xie, B., F. Zhang, Q. Zhang, J. Poterjoy, and Y. Weng, 2013: Observing strategy and observation targeting for tropical cyclones using ensemble-based sensitivity analysis and data assimilation. *Monthly weather review*, **141**, 1437–1453.

Yoshiike, S., and R. Kawamura, 2009: Influence of wintertime large-scale circulation on the explosively developing cyclones over the western North Pacific and their downstream effects. *Journal of Geophysical Research: Atmospheres*, **114**.

Zhang, F., C. Snyder, and R. Rotunno, 2002: Mesoscale predictability of the "surprise" snowstorm of 24–25 January 2000. *Monthly Weather Review*, **130**, 1617–1632.

Zhang, G., and Z. Wang, 2018: North Atlantic extratropical Rossby wave breaking during the warm season: Wave life cycle and role of diabatic heating. *Monthly Weather Review*, **146**, 695–712.

Zhang, S., G. Fu, C. Lu, and J. Liu, 2017: Characteristics of explosive cyclones over the Northern Pacific. *Journal of Applied Meteorology and Climatology*, **56**, 3187–3210.

Zheng, M., E. K. Chang, and B. A. Colle, 2013: Ensemble sensitivity tools for assessing extratropical cyclone intensity and track predictability. *Weather and forecasting*, **28**, 1133–1156.